

GLOBAL-MODE HELIOSEISMOLOGY:
EXTENSIONS OF A WELL-USED METHOD

A DISSERTATION
SUBMITTED TO THE DEPARTMENT OF PHYSICS
AND THE COMMITTEE ON GRADUATE STUDIES
OF STANFORD UNIVERSITY
IN PARTIAL FULFILLMENT OF THE REQUIREMENTS
FOR THE DEGREE OF
DOCTOR OF PHILOSOPHY

tim larson
December 2016

Copyright © 2017 by tim laron
All Rights Reserved

I certify that I have read this dissertation and that, in my opinion, it is fully adequate in scope and quality as a dissertation for the degree of Doctor of Philosophy.

(Philip Scherrer) Principal Adviser

I certify that I have read this dissertation and that, in my opinion, it is fully adequate in scope and quality as a dissertation for the degree of Doctor of Philosophy.

(Jesper Schou)

I certify that I have read this dissertation and that, in my opinion, it is fully adequate in scope and quality as a dissertation for the degree of Doctor of Philosophy.

(Sarah Church)

for my family

Abstract

Global-mode helioseismology has been used extensively to precisely infer the detailed properties of the solar interior. Multiple algorithms have been applied to several different datasets, which now span over two solar cycles. This dissertation deals primarily with two instruments, namely the *Michelson Doppler Imager* (MDI) onboard the *Solar and Heliospheric Observatory*, and the *Helioseismic and Magnetic Imager* (HMI) onboard the *Solar Dynamics Observatory*. For MDI, we have two velocity datasets spanning the 15 years from 1996 to 2011: high-resolution images which were taken for a few months each year, and low-resolution images which were taken almost all the time. For HMI, we have even higher resolution velocity images taken since 2010. Unlike MDI, HMI also provides intensity data.

The initial motivation for this study was to address known systematic errors in the analysis of MDI data, as well as discrepancies with inferences drawn by other projects, most notably the *Global Oscillation Network Group*. In particular, the MDI results indicated a high-latitude peak in the solar rotation rate, which is now believed to be spurious. Also, certain fits resulted in normalized residuals that indicate the fit is not using the correct model. Lastly, MDI saw an annual periodicity in frequency shifts, which can only be because of errors in geometry.

Now that MDI is no longer operating, it has also become important to achieve continuity between the MDI and HMI datasets. To that end, both have been processed in their entirety using the same set of software. Since the original software was written when computational capabilities were far less than now, this involved the application of several updates. At the same time, we have adopted better models of the physics behind the oscillations and applied various geometric corrections.

In this dissertation we investigate how these changes affected the global-mode parameters from the MDI analysis and the systematic errors therein. We then apply the fully updated analysis to the HMI data, and make a comparison of mode parameters derived from the various datasets from the two instruments.

We find methods that decrease or eliminate the systematic errors mentioned above. Hence, inferences of the Sun's interior rotation have become more robust. Further, the comparison between MDI and HMI encourages the concatenation of their datasets, which may allow for the detection of new oscillation modes.

Acknowledgement

I went through the lowest time of my life here at Stanford. It is only by sheer luck that I enjoy the completely undeserved good fortune to be alive at all. Given the irrefutable meaninglessness of existence, there are few things left the value of which I am able to perceive. Among those things are my relationships with my advisors, Jesper Schou and Phil Scherrer. For the successful completion of my time here, I would like to thank these two, and no one else. Many have given me help over the years, but nothing can compare to the help Jesper and Phil gave me. Without their kindness, compassion, understanding, and friendship, I could never have composed the document you are reading. It reflects dismally on our culture that they are most respected for their scientific accomplishments when their true contribution to our species is far greater. My hope is that I can withdraw my participation from such a culture and follow the example set by my advisors.

Contents

Abstract	v
Acknowledgement	vii
1 Introduction	1
2 Mathematical Background	9
3 Analysis of Data from the MDI Medium-ℓ Program	19
3.1 Introduction	19
3.2 Data	24
3.3 Method	26
3.3.1 Spherical Harmonic Transform	27
3.3.2 Detrending and Gapfilling	29
3.3.3 Peakbagging	33
Leakage Matrix	38
Asymmetry	41
3.4 Results	43
3.4.1 Mode Parameters	43
3.4.2 Systematic Errors	56
3.5 Discussion and Future Prospects	62
4 Analysis of Full-Disk Datasets from MDI and HMI	69
4.1 Introduction	69

4.2	Data	71
4.3	Method	74
4.4	Results	75
4.4.1	MDI Mode Parameters	75
4.4.2	Systematic Errors in MDI data	80
4.4.3	HMI Mode Parameters	83
4.4.4	Systematic Errors in HMI data	89
4.4.5	Comparison of MDI and HMI	91
4.4.6	Annual Periodicity	96
4.5	Discussion and Future Prospects	99
5	Looking Back, Looking Forward	105
5.1	Ideas	105
5.2	Zonal Flows	114
5.3	Conclusion	120

List of Figures

1.1	Sunspot areas	2
1.2	An ℓ - ν diagram	5
1.3	A zonal flow plot for 15 years of MDI	7
3.1	Normalized residuals of a fit for rotation	21
3.2	Rotation as a function of radius at selected latitudes	22
3.3	Change in seismic radius as a function of time	23
3.4	Changes in frequency	45
3.5	Changes in amplitude	46
3.6	Changes in width	47
3.7	Changes in background	48
3.8	Changes in a_1 coefficient	49
3.9	Changes in mode parameters resulting from all updates	51
3.10	Ratio of improved to original error estimates	52
3.11	Error amplification resulting from asymmetric mode profiles	53
3.12	Number of modes fitted as a function of time for five analyses	53
3.13	Difference in mode parameters between 360-day and 72-day fits	54
3.14	Ratio of the errors estimated from 360-day fits to those from 72-day fits	55
3.15	Tradeoff curves for select analyses	58
3.16	Normalized residuals of a_1 for different tradeoff parameters	59
3.17	Internal rotation for different tradeoff parameters	60
3.18	Amplitude of cosine vs. sine component of annual periodicity	61
3.19	Internal rotation at 75° latitude for select analyses	63
3.20	An ℓ - ν diagram with magnified errors	65

4.1	Number of modes fitted in all dynamics runs for four analyses	76
4.2	Effect of apodization on mode parameters	78
4.3	Effect of smoothing and subsampling on mode parameters.	79
4.4	Effect of smoothing and subsampling on amplitudes as a function of time	80
4.5	Tradeoff curves for three analyses averaged over all dynamics runs . .	81
4.6	Residuals of a_1 for three analyses averaged over all dynamics runs . .	82
4.7	Internal rotation at 75° for the 1998 dynamics run	83
4.8	Number of modes fitted as a function of time for HMI	84
4.9	Difference in mode coverage for symmetric and asymmetric profiles .	85
4.10	Effect of asymmetric profiles on mode parameters	86
4.11	Effect of length of timeseries on mode parameters	88
4.12	Tradeoff curves for an average over six years of HMI	89
4.13	Residuals of a_1 for an average over six years of HMI	90
4.14	Internal rotation at 75° latitude for HMI	90
4.15	Difference between MDI and HMI full-disk fits	92
4.16	Difference between low-resolution MDI data and an HMI proxy . . .	93
4.17	Difference between HMI full disk and low-resolution fits	94
4.18	Difference between MDI full-disk and low-resolution fits	95
4.19	f -mode frequency shift for the entire MDI mission.	97
4.20	f -mode frequency shift for MDI with solar-cycle dependence removed	97
4.21	f -mode frequency shift for the first six years of HMI.	98
4.22	f -mode frequency shift for HMI with solar-cycle dependence removed	98
4.23	Number of modes fitted with absolute value of B_0 overplotted	99
4.24	Effect of different apodizations on amplitudes and widths	100
4.25	Internal rotation at 75° latitude resulting from a new leakage matrix .	102
4.26	Tradeoff curves resulting from a new leakage matrix	103
5.1	Internal rotation at 75° latitude for restricted modesets	107
5.2	Internal rotation at 75° latitude for different values of B_0	108
5.3	Tradeoff curves for different values of B_0	109
5.4	Tradeoff curves for three apodizations for small $ B_0 $	111

5.5	Internal rotation at 75° latitude for three apodizations for small $ B_0 $.	111
5.6	Tradeoff curves for three apodizations for large $ B_0 $	112
5.7	Internal rotation at 75° latitude for three apodizations for large $ B_0 $.	112
5.8	Tradeoff curves three apodizations using a new leakage matrix	113
5.9	Internal rotation at 75° latitude for three apodizations using a new leakage matrix	113
5.10	Updated zonal flow plot for 15 years of MDI	115
5.11	Difference in zonal flows resulting from updates	115
5.12	Zonal flows for MDI mission in 360-day intervals	116
5.13	Zonal flows for HMI in 72-day intervals	118
5.14	Difference in zonal flows resulting from the <code>vw_V</code> proxy	118
5.15	Zonal flows for HMI in 360-day intervals	119
5.16	Difference in zonal flows between 360-day and 72-day fits	119
5.17	Difference in zonal flows resulting from asymmetric mode profiles . . .	120
5.18	Zonal flows for combined MDI and HMI 72-day datasets	121

List of Tables

3.1	Timeseries derived from MDI Medium- ℓ Program data	25
3.2	Sequence of changes made to the analysis	56
4.1	Dynamics timeseries, derived from full-disk MDI data	72
4.2	HMI timeseries	73

Chapter 1

Introduction

Throughout the course of the preceding millenia, human beings have had many different ideas about the Sun. For accounts of prehistoric views, the reader is referred to excellent compilations and references therein on both solar folklore (Scherrer, 2015b) and ancient observatories (Scherrer, 2015a). There is also a thorough discussion of Galileo’s research on the Sun (Van Helden, 1995). In this dissertation, we shall begin our narrative with the research of Richard Carrington in the mid-19th century. His work, *Observations of the Spots on the Sun* (1863), is the first scientific paper that is of direct numerical relevance to the work presented here. In it, he gives a measurement of the position of the Sun’s rotation axis based on the motions of sunspots. The Carrington elements, as these measurements came to be called, remained unchallenged for over a century.

Even earlier, however, Carrington had already made several interesting observations about sunspots. Although he was not the first to notice the approximate periodicity of sunspot numbers¹, Carrington has been credited with the first butterfly diagram (Carrington, 1858), which depicts how sunspots emerge at high latitudes early in the solar cycle and gradually migrate to lower latitudes (a modern example is shown in Figure 1.1). Carrington was also the first to quantify the variation of solar rotation with latitude (Carrington, 1863).

¹This was done by S. Heinrich Schwabe in 1843, using observations he carried out himself (Schwabe, reprinted 2004).

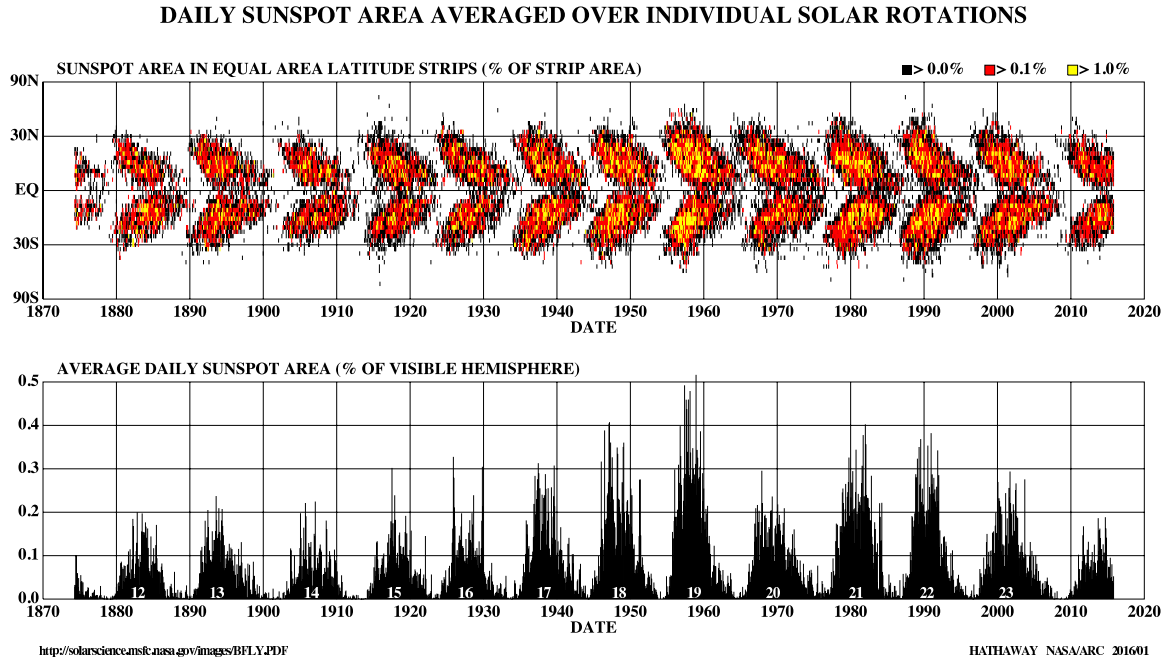


Figure 1.1: Top: a butterfly diagram. Bottom: sunspot areas. Provided courtesy of David Hathaway, NASA

Most spectacularly, Carrington (and independently Richard Hodgson) made the first observation of a solar flare on 1 September 1859. What makes this observation so spectacular is that the associated coronal mass ejection struck the Earth. Auroras could be seen as far south as Panama. Telegraph systems failed across the northern hemisphere. This particular geomagnetic solar storm became known as the Carrington Event and was the first indication that events on the Sun could affect us here on Earth. It has been estimated that if a similar event occurred today, the cost of the damage in the US alone could exceed \$2 trillion (Lloyd's and Atmospheric and Environmental Research, 2013).

Such damage is not unprecedented. In March 1989, a similar but smaller event caused power grids to fail in Quebec. As our society becomes more dependent on electronic technology, we become more susceptible to various disruptions caused by solar events. Objects above the atmosphere, such as communications satellites and astronauts, are in the greatest danger. Closer to Earth radio communication has often

been disrupted. Our vulnerability was highlighted in July 2012 when a Carrington-size event was observed, but by good fortune did not strike the Earth (Phillips, 2014).

A major milestone in our understanding of solar activity came in the early 20th century, when George Hale discovered that sunspots are regions of concentrated magnetic field (Hale, 1908). Later, he and his colleagues also observed them to occur in opposite-polarity pairs, with the leading polarity generally being the same in one hemisphere and opposite in the other hemisphere. The polarity then reverses with each sunspot cycle. Hence, the magnetic cycle is composed of two sunspot cycles. Further, they also observed Joy's law, which states that "the following spot of the pair tends to appear farther from the equator than the preceding spot, and the higher the latitude, the greater is the inclination of the axis to the equator." (Hale *et al.*, 1919). George Hale also founded Mount Wilson Observatory (MWO) in southern California, which would provide important solar data for over a century.

Decades later, Horace Babcock found that the Sun's polar magnetic field reverses with the same period, though out of phase with the sunspot cycle (Babcock, 1959). Eventually it was discovered that many of the Sun's physical parameters, among them its 10.7 cm radio flux and its total irradiance, also vary with the solar cycle. Most importantly, the frequency of occurrence of solar flares and coronal mass ejections is highly correlated with sunspot number (Hathaway, 2010).

Hence, we are presented with two compelling reasons to study the Sun. In the first place, there are the scientific questions posed by the solar cycle itself: why is it (approximately) 11 years long? Why do sunspots emerge and move in the patterns they do? How is the magnetic field of the Sun generated in the first place? Secondly, it becomes increasingly important to our society for us to make predictions of solar behavior. Some have conjectured that a grand maximum of solar activity may occur in the next few centuries, such as some evidence suggest it has in the past (Eddy, 1976), and our susceptibility to it will only become greater.

The magnetic field of the Sun is presumably generated by a system of electric currents below the surface. Therefore our understanding of it can only be enhanced by a measurement of solar plasma flows. As mentioned above, surface measurements were already in progress at the time of Carrington, but since all the light we see from the Sun is emitted from its surface, we have no direct probe of the solar interior.

The big break came in 1960 when Robert Leighton, using only photographic techniques, discovered a five minute oscillation in the solar velocity field (Leighton, Noyes, and Simon, 1962). Using the same data he was also able to detect a non-oscillating component, originally discovered by Avril Hart in 1953 (Hart, 1954), that would soon come to be known as supergranulation. Several theories were put forward to explain the oscillations, such as a ringing solar atmosphere and various types of travelling waves. Even when it was recognized that the oscillations probably represented standing acoustic waves, there was still debate about the location of the resonant cavity. Then in 1970 Roger Ulrich calculated the eigenfrequencies of waves trapped in the convection zone, and found them to be in agreement with the available observations. His cavity was bounded by the photosphere on top, while in the interior the waves were refracted back to the surface. The following year John Leibacher and Bob Stein independently published similar ideas backed up by numerical simulation, but it wasn't until 1975 that Franz Deubner provided the observations that confirmed the predictions (Stein, 2013). He created one of the first ℓ - ν (or equivalently k - ω) diagrams, a modern example of which is shown in Figure 1.2. Clearly visible are the distinct mode ridges corresponding to different numbers of nodes in radius, which revealed the modal nature of the oscillations.

From then on, helioseismology became more and more popular, and observations increased in both quantity and quality. Particularly desirable are long continuous observing runs, which for a single observatory would always be interrupted by the cycle of day and night as well as bad weather. This difficulty can be surmounted by building a network of nearly identical observatories. The first of these was the Birmingham Solar Oscillation Network (BiSON), which began in 1976² with only two observing stations. The current six-site configuration was reached in 1992. In 1979 the Birmingham group published an analysis of 300 hours of velocity data averaged over the solar disk (Claverie *et al.*, 1979). Unlike Deubner's observations, which revealed the short wavelength modes, these Sun-as-a-star observations revealed the low-degree modes. Whereas the modes found by Deubner can easily be labelled by their radial order because of good agreement with models, for the low-degree modes the radial order is much more uncertain.

²The official beginning of BiSON observations was in 1981.

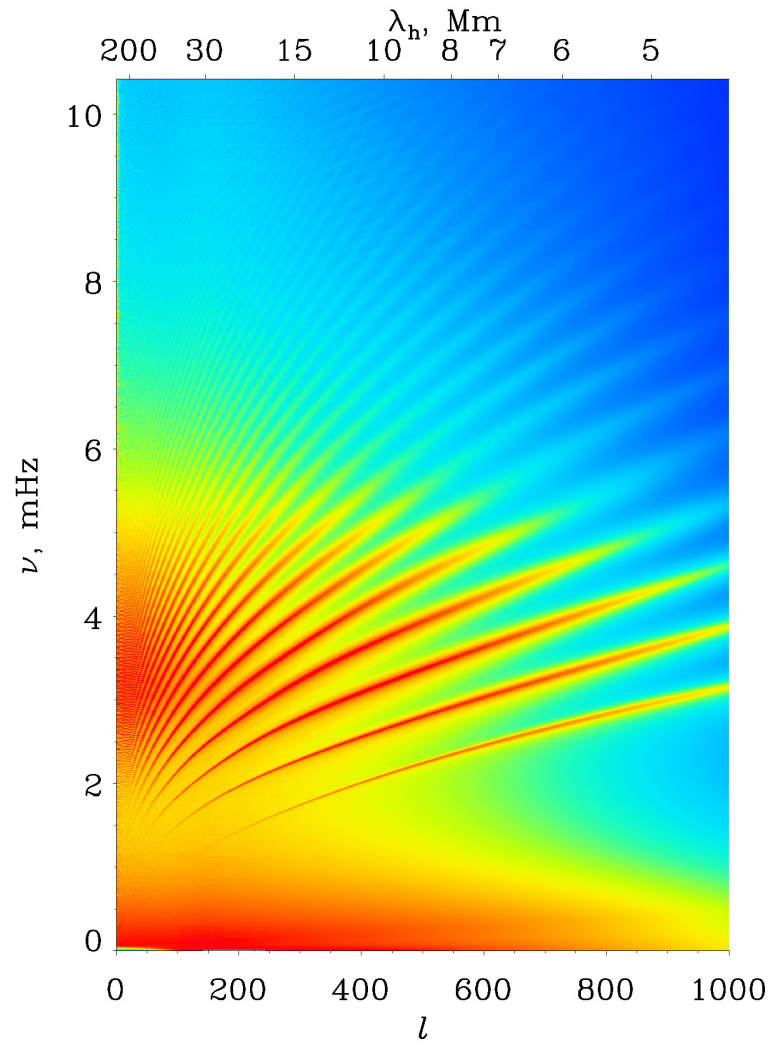


Figure 1.2: An l - ν diagram, which shows power as a function of angular degree and frequency. Provided courtesy of the Solar Oscillation Investigation at Stanford.

Finally, at the end of 1981, Tom Duvall and Jack Harvey used a 244×248 pixel camera at the South Pole to make intensity observations of the solar surface. Their longest continuous dataset was only 50 hours, but they were nonetheless able to detect modes of intermediate degree (Harvey, 2013). Now an ℓ - ν diagram could be constructed that connected the high and low degree modes, enabling unambiguous identification of their radial order. This result will be discussed below in the context of the solar neutrino flux.

Also at the beginning of the 80's was the discovery of zonal flows on the Sun by Bob Howard and Barry LaBonte (Howard and Labonte, 1980). Using velocity data that had been recorded daily at the 150-Foot Tower Telescope at Mount Wilson Observatory since 1966, they fit a smooth curve to the Sun's rotation rate as a function of latitude. When this curve was subtracted, the residuals revealed alternating latitudinal bands of faster-than-average and slower-than-average rotation, which migrated in latitude throughout the solar cycle. Although they termed this phenomenon "torsional oscillation", I feel this term unfortunately implies a restoring force, which is unlikely to exist. Hence, throughout this work I shall refer to it simply as zonal flows. A modern zonal flow plot is shown in Figure 1.3.

Another important milestone during the 80's was the establishment of a dedicated helioseismology telescope at the 60-Foot Solar Tower at Mount Wilson Observatory. The first observations were recorded in 1984 using a Magneto-Optical Filter (MOF: Cacciani and Rhodes, 1984), and in 1987 the system was upgraded with a 1024×1024 CCD. MWO then became home to the first long-term, high-cadence observing program, which lasted for 23 years (Rhodes, 2013). While in operation, the 60-Foot Solar Tower produced an image every minute.

A different type of instrumentation, called the Fourier Tachometer, had initially been developed in 1978 by Tim Brown and Jacques Beckers (Beckers and Brown, 1978). Then, around 1985, an improved version was selected for use in the Global Oscillation Network Group (GONG: Harvey *et al.*, 1996), which came online in 1995 using six observing sites. This network was the first to provide near-continuous coverage of the Sun at a resolution of 256×256 pixels. Due to technical limitations (camera speeds) at the time, a higher resolution was not possible, and the pixels were

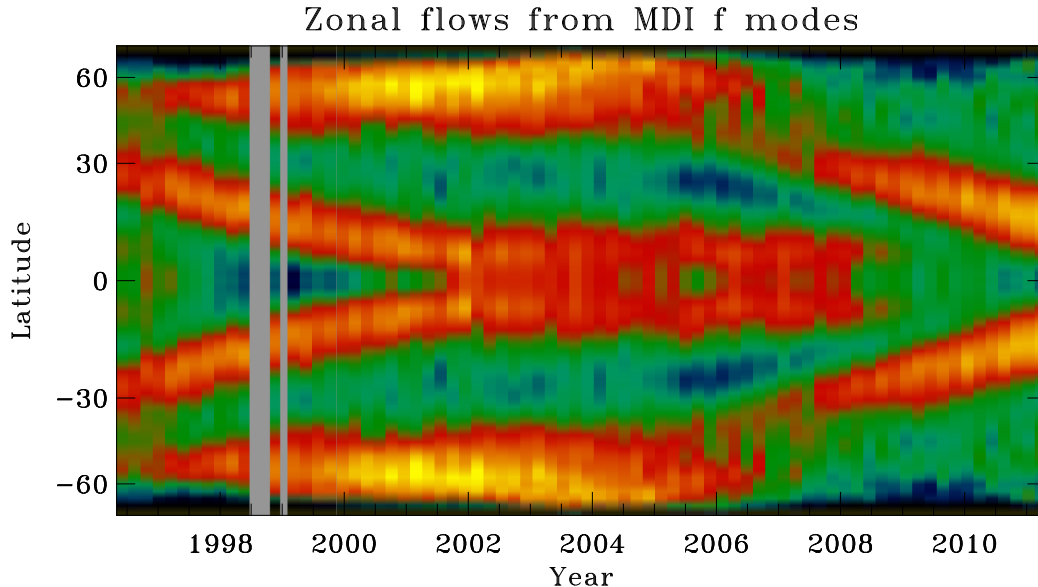


Figure 1.3: A zonal flow plot constructed from the entire medium- ℓ dataset from the Michelson Doppler Imager (MDI). Provided courtesy of Jesper Schou.

non-square rectangles. In 2001 the GONG network was upgraded with 1024×1024 square pixel cameras. Throughout, GONG has used the Ni I 6768 Å spectral line to create both dopplergrams and magnetograms at a cadence of one minute.

Although GONG represented a large advance in the quality of helioseismic data, it was still limited by distortions caused by turbulence in Earth’s atmosphere. To achieve a higher resolution for near-surface measurements and a higher signal-to-noise ratio (and duty cycle), it was recognized that spaceborn instrumentation is needed. In an appropriate orbit, such an instrument could be fully illuminated all the time. The first of these was the Michelson Doppler Imager (MDI: Scherrer *et al.*, 1995), which used the same idea as the Fourier Tachometer, and a 1024×1024 CCD. MDI was launched at the end of 1995, and used the same spectral line and cadence as GONG. Further details are provided in Chapter 3.

The final instrument we shall be interested in is the Helioseismic and Magnetic Imager (HMI: Schou *et al.*, 2012), which was launched in 2010. Although its design is extremely similar to that of MDI, HMI is equipped with a 4096×4096 CCD, uses

the Fe I 6173 Å spectral line, and produces observables at a cadence of 45 seconds. Further details are provided in Chapter 4.

Helioseismology has become increasingly precise over the years, and helioseismic inferences place tight constraints on various physical processes. Most obviously, we can check the accuracy of solar evolution models, which also tells us how well we might be modelling other stars. One surprise that contradicted theoretical predictions was the discovery that the solar core has a solid-body rotation and that it is slower than the surface rotation at the equator. Previously it was thought that a rapidly rotating core might compromise tests of general relativity based on the precession of the perihelion of Mercury; helioseismology has squashed this concern. It has also helped to resolve a puzzle in neutrino physics, which was that the observed solar neutrino flux was only about a third of what was expected based on the Sun's luminosity. Initial attempts to solve the puzzle usually involved modifying solar models in such a way that they would have a lower core temperature, and hence a lower flux of the high energy neutrinos to which early experiments were sensitive. One might, for example, try lowering the heavy element abundance of the core, but this was ruled out when the results of Duvall and Harvey allowed the unambiguous identification of the oscillation modes (Christensen-Dalsgaard, 2002). Eventually, other experiments confirmed the reality of the now well-known neutrino oscillations.

In the following chapter, a sketch is given of some aspects of the theory of stellar oscillations. Chapter 3 gives a full account of the method used to analyze the entire MDI medium- ℓ dataset. I also describe a sequence of upgrades applied to the processing and discuss their effects on mode parameters and systematic errors. Chapter 4 extends these ideas to the analysis of full-disk data from MDI, the analysis of HMI velocity data, and a comparison between the two instruments. Chapter 5 implements some of the ideas suggested by Chapters 3 and 4, and presents how long-term trends in surface rotation are affected. Finally, a summary is given as well as a look forward to how we might do even better.

Chapter 2

Mathematical Background

This chapter draws heavily on the presentation given by Jørgen Christensen-Dalsgaard in his Lecture Notes on Stellar Oscillations, available at <http://astro.phys.au.dk/~jcd/oscilnotes/>. All equations are adapted from the same.

Velocities on the surface of the Sun can be inferred from direct observations. The frequencies and other parameters describing the Sun's oscillation modes can be derived from these data. In order to connect these observations to inferences about the solar interior, a mathematical framework based on the underlying physics is needed. As a beginning, let us consider the conservation of mass, momentum, and energy in the interior of the Sun.

Assuming no mass sources or sinks, conservation of mass is expressed by the equation of continuity:

$$\frac{d\rho}{dt} + \rho \nabla \cdot \mathbf{v} = 0 \quad (2.1)$$

where ρ is the density and \mathbf{v} is the velocity of a fluid element. The time derivative is the material time derivative, which follows the motion of the fluid. For any quantity q , it is related to the derivative at a fixed point (the local time derivative) by

$$\frac{dq}{dt} = \frac{\partial q}{\partial t} + \mathbf{v} \cdot \nabla q. \quad (2.2)$$

Conservation of momentum is expressed by the equation of motion. Assuming the only forces acting on a fluid element arise from pressure and gravity, we have

$$\rho \frac{d\mathbf{v}}{dt} = -\nabla p + \rho \mathbf{g} = -\nabla p - \rho \nabla \Phi \quad (2.3)$$

where p is pressure and \mathbf{g} is the acceleration of gravity. The gravitational potential Φ satisfies Poisson's equation, $\nabla^2 \Phi = 4\pi G\rho$. Note that I have neglected the effects of viscosity and magnetic fields.

An equation for the balance of energy flux inside the Sun would in general be quite complicated. It can be immensely simplified by assuming that the oscillations occur adiabatically, that is, with no heat transfer, so that entropy remains constant. This is justified since in most of the Sun the time scale of the oscillations is much shorter than the time scales of energy transfer. In that case, we have

$$\frac{dp}{dt} = \frac{\Gamma_1 p}{\rho} \frac{d\rho}{dt} \quad (2.4)$$

where Γ_1 is the adiabatic exponent. This approximation will break down near the surface, where also the density scale height becomes comparable to the wavelengths of the modes and the speed of convective motions becomes comparable to the local sound speed.

Let us now consider the oscillation modes to be small perturbations around an equilibrium structure, in which all time derivatives vanish. For example, we shall write the density as $\rho(\mathbf{r}, t) = \rho_0(\mathbf{r}) + \rho'(\mathbf{r}, t)$. The velocity is also considered to be a small perturbation, so that if the displacement caused by the perturbation is $\boldsymbol{\xi}$, the velocity is given by $\mathbf{v} = \partial \boldsymbol{\xi} / \partial t$. In a frame following the motion of the fluid, the perturbation to the density would be $\delta\rho = \rho' + \boldsymbol{\xi} \cdot \nabla \rho_0$. Substituting these expressions into the above equations, cancelling terms in the equilibrium quantities, and retaining only terms linear in the perturbations yields

$$\rho' + \nabla \cdot (\rho_0 \boldsymbol{\xi}) = 0 \quad (2.5a)$$

$$\rho_0 \frac{\partial^2 \boldsymbol{\xi}}{\partial t^2} = -\nabla p' - \rho_0 \nabla \Phi' - \rho' \nabla \Phi_0 \quad (2.5b)$$

$$p' + \boldsymbol{\xi} \cdot \nabla p_0 = \frac{\Gamma_1 p_0}{\rho_0} (\rho' + \boldsymbol{\xi} \cdot \nabla \rho_0) \quad (2.5c)$$

where $\nabla^2\Phi' = 4\pi G\rho'$. Since none of the coefficients in the above equations depend on time, we expect the time dependence of the solution to be separable. For oscillations it is natural to assume a time dependence of the form $\exp(-i\omega t)$. Equation 2.5b then implies $\omega^2\boldsymbol{\xi} = (1/\rho_0)\nabla p' + \nabla\Phi' + (\rho'/\rho_0)\nabla\Phi_0$. Since p' and Φ' can both be expressed in terms of ρ' , and ρ' can be obtained from $\boldsymbol{\xi}$, this equation represents a linear eigenvalue problem. That is, if we rewrite it as $\omega^2\boldsymbol{\xi} = \mathcal{F}(\boldsymbol{\xi})$, then $\boldsymbol{\xi}(\mathbf{r}, t) = \tilde{\boldsymbol{\xi}}(\mathbf{r}) \exp(-i\omega t)$ will be a solution if $\tilde{\boldsymbol{\xi}}$ is a solution to $\omega^2\tilde{\boldsymbol{\xi}} = \mathcal{F}(\tilde{\boldsymbol{\xi}})$. I shall return to this formulation of the problem below.

Since the equilibrium quantities are spherically symmetric, we can expect a similar separability of the dependence on the horizontal variables. We therefore write $\boldsymbol{\xi} = \boldsymbol{\xi}_r + \boldsymbol{\xi}_h$ where $\boldsymbol{\xi}_r = \xi_r\hat{r}$ and $\boldsymbol{\xi}_h = \xi_\theta\hat{\theta} + \xi_\phi\hat{\phi}$. If we similarly separate out the horizontal component of the equation of motion, as well as that of the gradient, divergence, and laplacian operators, it can be shown that all derivatives with respect to the horizontal variables appear as ∇_h^2 . We therefore seek a function $f(\theta, \phi)$ that is a solution to the eigenvalue equation

$$r^2\nabla_h^2 f = \frac{1}{\sin\theta} \frac{\partial}{\partial\theta} (\sin\theta \frac{\partial f}{\partial\theta}) + \frac{1}{\sin^2\theta} \frac{\partial^2 f}{\partial\phi^2} = \lambda f. \quad (2.6)$$

Since the coefficients in this equation don't depend on ϕ , we expect a further separability as $f(\theta, \phi) = f_1(\theta)f_2(\phi)$. We can then easily see that f_2 is proportional to its second derivative, so a solution is the exponential function. Requiring that f_2 is continuous, we have $f_2(\phi) = \exp(im\phi)$ where m must be an integer. Inserting this solution into Equation 2.6 results in the associated Legendre differential equation for f_1 in terms of $x = \cos\theta$, if we require that $\lambda = -\ell(\ell + 1)$. This equation only has regular solutions when ℓ is an integer satisfying $\ell \geq |m| \geq 0$. We can then write $f_1(\theta) = P_\ell^m(\cos\theta)$ where P_ℓ^m is an associated Legendre function. Then $f(\theta, \phi) = P_\ell^m(\cos\theta) \exp(im\phi) = Y_\ell^m(\theta, \phi)$ where Y_ℓ^m is known as a spherical harmonic. By convention ℓ is called the spherical harmonic degree and m its azimuthal order. The spherical harmonics will have a total of ℓ node lines, with m in longitude and $\ell - m$ in latitude. Note that here and elsewhere I have absorbed normalization constants into the P_ℓ^m so that the integral of $|Y_\ell^m|^2$ over a sphere is one.

Now that the solution is fully separated, we may write, for example,

$$\xi_r(\mathbf{r}, t) = \tilde{\xi}_r(r) Y_\ell^m(\theta, \phi) \exp(-i\omega t) \quad (2.7)$$

and so on for p' , ρ' , and Φ' . The horizontal component of the equation of motion then gives

$$\boldsymbol{\xi}_h = \frac{1}{\omega^2 \rho_0} (\nabla_h p' + \rho_0 \nabla_h \Phi') = \tilde{\xi}_h(r) \left(\frac{\partial Y_\ell^m}{\partial \theta} \hat{\theta} + \frac{1}{\sin \theta} \frac{\partial Y_\ell^m}{\partial \phi} \hat{\phi} \right) \exp(-i\omega t) \quad (2.8)$$

where

$$\tilde{\xi}_h(r) = (\tilde{p}'/\rho_0 + \tilde{\Phi}')/(r\omega^2). \quad (2.9)$$

Inserting the separated solutions into Equations 2.5 and the perturbed Poisson's equation, recalling that $\nabla_h^2 Y_\ell^m = -\ell(\ell+1)Y_\ell^m/r^2$, dividing by common factors, and eliminating $\tilde{\rho}'$ yields the following system of ordinary differential equations for the amplitude functions:

$$\frac{d\xi_r}{dr} = - \left(\frac{2}{r} + \frac{1}{\Gamma_1 p_0} \frac{dp_0}{dr} \right) \xi_r + \frac{1}{\rho_0 c^2} \left(\frac{S_\ell^2}{\omega^2} - 1 \right) p' + \frac{\ell(\ell+1)}{\omega^2 r^2} \Phi' \quad (2.10a)$$

$$\frac{dp'}{dr} = \rho_0 (\omega^2 - N^2) \xi_r + \frac{1}{\Gamma_1 p_0} \frac{dp_0}{dr} p' - \rho_0 \frac{d\Phi'}{dr} \quad (2.10b)$$

$$\frac{1}{r^2} \frac{d}{dr} \left(r^2 \frac{d\Phi'}{dr} \right) = 4\pi G \left(\frac{p'}{c^2} + \frac{\rho_0 \xi_r}{g_0} N^2 \right) + \frac{\ell(\ell+1)}{r^2} \Phi' \quad (2.10c)$$

where $c^2 = \Gamma_1 p_0 / \rho_0$ is the squared adiabatic sound speed, $g_0 = -d\Phi_0/dr$, and I have dropped the tildes. The characteristic frequencies S_ℓ and N are given by

$$S_\ell^2 = \frac{\ell(\ell+1)c^2}{r^2} \quad \text{and} \quad N^2 = g_0 \left(\frac{1}{\Gamma_1 p_0} \frac{dp_0}{dr} - \frac{1}{\rho_0} \frac{d\rho_0}{dr} \right). \quad (2.11)$$

To complete the problem, a few boundary conditions must be specified. These include regularity at $r = 0$ and the continuity of Φ' and its derivative at the solar surface. The final condition will depend upon the treatment of the solar atmosphere, but can often be approximated by constant pressure at the perturbed surface.

This system can be solved numerically, and it is the numerical solutions that are

typically used when inferring properties of the solar interior from the oscillation frequencies. However, a good deal of understanding can be extracted if some simplifying assumptions are applied. The first of these is the Cowling approximation, which is to neglect the perturbation to the gravitational potential, setting $\Phi' = 0$. Since Φ' is given by a volume integral over ρ' , this is justified for modes of either high radial order or high spherical harmonic degree, which have rapid spatial variation, so that regions of positive and negative perturbation will approximately cancel in the integral. The problem is then reduced to a second-order system for ξ_r and p' .

If we further make the approximation that the perturbations vary much more rapidly than the background state, then the coefficients containing dp_0/dr in Equations 2.10a and 2.10b can be neglected. This approximation breaks down at the surface, and near the center the $2/r$ term obviously cannot be ignored, but the resulting equations are instructive nonetheless. Eliminating p' gives

$$\frac{d^2\xi_r}{dr^2} = -\frac{\omega^2}{c^2} \left(1 - \frac{N^2}{\omega^2}\right) \left(1 - \frac{S_\ell^2}{\omega^2}\right) \xi_r = -K(r)\xi_r. \quad (2.12)$$

Hence, locally the solution will be an exponential function. If we make the identification $K(r) = k_r^2$, where k_r is the radial component of the wave vector, then it is clear that the local solution will be oscillating for positive values of K and exponentially decreasing or increasing for negative values. Similarly, since we know $\nabla_h^2 \xi_r = -\ell(\ell + 1)\xi_r/r^2$, we can make the identification $k_h^2 = \ell(\ell + 1)/r^2$, where k_h is the horizontal component of the wave vector. The values of r for which $K = 0$ are called the turning points of the mode; in the intervening regions where $K > 0$ the mode is said to be trapped.

Later I will describe how a less crude approximation can be made, but the result will simply be a more accurate expression for $K(r)$. For now, let us note that the solution will be oscillating if either $\omega^2 > N^2$ and $\omega^2 > S_\ell^2$, or $\omega^2 < N^2$ and $\omega^2 < S_\ell^2$. Hence we are presented with two classes of oscillation modes, one at high frequencies and one at low frequencies. In the latter case, assuming $\omega \ll S_\ell$, we can approximate K by $(N^2 - \omega^2)\ell(\ell + 1)/(r^2\omega^2)$, so the waves will be trapped in the region where $\omega^2 < N^2$. According to a standard solar model, this implies an upper turning point

below the base of the convection zone. Gravity (buoyancy) provides the dominant restoring force for these modes, which are therefore called g -modes. However, since these modes are evanescent throughout the convection zone, it is unclear whether or not they have observable amplitudes at the solar surface (Appourchaux *et al.*, 2010), and we shall not discuss them further here.

In the high frequency case, assuming $\omega \gg N$, we may approximate

$$K = k_r^2 = \frac{\omega^2 - S_\ell^2}{c^2}, \quad (2.13)$$

so the lower turning point r_1 will be given by $\omega = S_\ell$, or equivalently

$$\frac{r_1^2}{c^2(r_1)} = \frac{\ell(\ell + 1)}{\omega^2}. \quad (2.14)$$

The dominant restoring force for these modes is pressure, which motivates calling them p -modes. Indeed, had we neglected all derivatives of equilibrium quantities from the outset, we would have found that ρ' obeys the wave equation, so that solutions would be plane sound waves with the dispersion relation $\omega^2 = c^2|\mathbf{k}|^2 = c^2(k_r^2 + k_h^2)$. The lower turning point would be where $k_r = 0$. Inserting the expression for k_h given above, we easily recover Equation 2.14. The fact that k_r decreases with depth while k_h increases with depth has a clear physical interpretation: since the sound speed increases with depth, acoustic wave fronts will be refracted toward the surface, where they are reflected.

To actually derive the upper turning point for p -modes, a more accurate description is needed. If we still make the Cowling approximation and ignore the $2/r$ term, but now retain terms containing derivatives of equilibrium quantities (except g_0), we can write down a much more complicated second-order equation for ξ_r . If we are clever enough to make the substitution $X = c^2\rho_0^{1/2}\nabla \cdot \boldsymbol{\xi}$, originally derived by Douglas Gough (Deubner and Gough, 1984), then this equation can be expressed as $d^2X/dr^2 = -K(r)X$ where now

$$K(r) = \frac{\omega^2}{c^2} \left[1 - \frac{\omega_c^2}{\omega^2} - \frac{S_\ell^2}{\omega^2} \left(1 - \frac{N^2}{\omega^2} \right) \right]. \quad (2.15)$$

The frequency ω_c is called the acoustic cutoff frequency and is given by

$$\omega_c^2 = \frac{c^2}{4H^2} \left(1 - 2 \frac{dH}{dr} \right) \quad (2.16)$$

where $H = -(\text{d log } \rho_0/\text{d}r)^{-1}$ is the density scale height. Close to the surface, we will have $\omega \gg S_\ell$, so the upper turning point r_2 will approximately be at the point where $\omega = \omega_c$. Physically, this means the waves are reflected when their wavelengths become comparable to H . Since ω_c is small throughout the interior, it has little effect on the the lower turning point. An asymptotic analysis shows that the condition for resonance is

$$\int_{r_1}^{r_2} \sqrt{K(r)} dr \approx \left(n - \frac{1}{2} \right) \pi. \quad (2.17)$$

It can then be shown that a generalization of the Duvall law (Duvall, 1982) holds:

$$\frac{\pi(n + \alpha(\omega))}{\omega} \approx \int_{r_1}^{r_2} \frac{1}{c} \left(1 - \frac{S_\ell^2}{\omega^2} \right)^{1/2} dr = F \left(\frac{\omega^2}{\ell(\ell + 1)} \right), \quad (2.18)$$

which provides the dispersion relation for p -modes. In this equation n is an integer greater than zero and α is a function of frequency alone. The physical meaning of the Duvall law is that for resonance to occur, the integral of the radial component of the wave vector from r_1 to r_2 must be an integral multiple of π , except for phase changes at the end points. In the crude approximation given by Equation 2.13, this condition is expressed by Equation 2.18. Hence, we also see that n roughly corresponds to the number of nodes in the radial direction.

One may notice that the analysis in terms of X cannot describe modes which have no divergence. In that case the mode does not compress the fluid, so we may assume that ρ_0 is constant and $\rho' = 0$. Then $\Phi' = 0$ automatically. Assuming continuity and adiabaticity, the condition $\nabla \cdot \boldsymbol{\xi} = 0$ also implies $p' = \rho_0 g_0 \xi_r$. Assuming constant gravity and ignoring the $2/r$ term as above, it can then be shown that $\xi_r \propto \exp(k_h r)$. Since such a mode has no nodes in radius, it is assigned $n = 0$ and is known as an f -mode, for “fundamental”. The vertical component of the equation of motion then gives us $\omega^2 = g_0 k_h$, which is the dispersion relation for waves on the surface of an infinitely deep ocean. Indeed, in this approximation, the two problems are equivalent.

In the next chapter it shall be seen how the ratio of the horizontal to vertical component of the displacement at the solar surface is used in fitting for the frequencies. Here, let us derive an approximation of it. To derive a ratio meaningful for the Sun as a whole, we first integrate the magnitude of each component over a sphere. Because of the normalization of the spherical harmonics, for the vertical component this is simply $|\xi_r|$. For the horizontal component, integration yields an additional factor, so that the ratio becomes $\sqrt{\ell(\ell+1)}|\xi_h|/|\xi_r|$. For the p -modes, assuming constant pressure at the surface, we will have $\delta p = p' + \xi_r dp_0/dr = 0$. Ignoring Φ' in Equation 2.9, at the surface we will have

$$\frac{|\xi_h|}{|\xi_r|} = \frac{1}{\rho_0} \frac{dp_0}{dr} \frac{1}{R\omega^2} = \frac{GM}{R^2} \frac{1}{R\omega^2} \quad (2.19)$$

since the equilibrium quantities satisfy the equation of hydrostatic support. The ratio we seek is then

$$c_t = \frac{g_0(R)k_h}{\omega^2} = \frac{\omega^2(0, \ell)}{\omega^2(n, \ell)} \quad (2.20)$$

where $g_0(R)$ is the surface gravity, $\omega(0, \ell)$ is the frequency of the f -mode at a given ℓ , and $\omega(n, \ell)$ is the corresponding frequency of the p -mode for a given n . This expression has the satisfying property that $c_t = 1$ for the f -mode, which it must since the f -mode is incompressible. Since frequency is an increasing function of n , c_t gets smaller as the order of the p -mode increases.

The foregoing analysis assumes zero velocity in the background model. This is obviously inaccurate for a rotating body such as the Sun. Further, if we wish to use observations to infer the background velocity field, it must be accounted for in the model. However, we will assume that the background velocity \mathbf{v}_0 is small enough that it can be treated as a small perturbation to the original model and that terms higher than linear in \mathbf{v}_0 can be neglected. In particular, the centrifugal force will be ignored. It can then be shown that the perturbed oscillation equations remain unchanged, except that Equation 2.5b must be replaced by

$$\rho_0 \frac{\partial^2 \boldsymbol{\xi}}{\partial t^2} = -\nabla p' - \rho_0 \nabla \Phi' - \rho' \nabla \Phi_0 - 2\rho_0 (\mathbf{v}_0 \cdot \nabla) \boldsymbol{\xi} \quad (2.21)$$

which, assuming the same time dependence, implies

$$\omega^2 \boldsymbol{\xi} = (1/\rho_0) \nabla p' + \nabla \Phi' + (\rho'/\rho_0) \nabla \Phi_0 - 2i\omega(\mathbf{v}_0 \cdot \nabla) \boldsymbol{\xi} = \mathcal{F}(\boldsymbol{\xi}) + \delta\mathcal{F}(\boldsymbol{\xi}). \quad (2.22)$$

A first-order perturbation analysis can now be performed. The result is that the change in frequency due to $\delta\mathcal{F}$ is

$$\delta\omega = \frac{\delta\omega^2}{2\omega} = \frac{1}{2\omega} \frac{\int \rho_0 \boldsymbol{\xi}^* \cdot \delta\mathcal{F}(\boldsymbol{\xi}) dV}{\int \rho_0 |\boldsymbol{\xi}|^2 dV} = -i \frac{\int \rho_0 \boldsymbol{\xi}^* \cdot (\mathbf{v}_0 \cdot \nabla) \boldsymbol{\xi} dV}{\int \rho_0 |\boldsymbol{\xi}|^2 dV}. \quad (2.23)$$

As usual, the perturbation to the frequency is calculated from the unperturbed eigenfunction. If we now take \mathbf{v}_0 to correspond to rotation about the polar axis of our coordinate system, we can write $\mathbf{v}_0 = \Omega(r, \theta) r \sin \theta \hat{\phi}$, where Ω is the angular velocity inside the Sun as a function of latitude and radius. We can then perform the integral, which is too complex to write out in full here. For conciseness, we shall simply write

$$\delta\omega_{n\ell m} = m \int_0^\pi \int_0^R K_{n\ell m}(r, \theta) \Omega(r, \theta) r dr d\theta \quad (2.24)$$

where $\delta\omega_{n\ell m}$ is the frequency shift for a mode characterized by radial order n , degree ℓ , and azimuthal order m , and $K_{n\ell m}$ is the corresponding kernel relating it to internal rotation. It is common practice, however, to represent the frequency shifts as polynomials in m , an idea originated by Brown (1986). In that case, we write

$$\delta\omega_{n\ell m} = \omega_{n\ell m} - \omega_{n\ell 0} = \sum_{i=1}^{i_{\max}} a_i(n, \ell) \mathcal{P}_i^\ell(m) \quad (2.25)$$

for some polynomials \mathcal{P}_i^ℓ and coefficients a_i , where i is the order of the polynomial. The a -coefficients will then be linearly related to the frequency shifts, and we can write

$$a_i(n, \ell) = \sum_m b_i(\ell, m) \delta\omega_{n\ell m} = \sum_m b_i(\ell, m) m \int_0^\pi \int_0^R K_{n\ell m}(r, \theta) \Omega(r, \theta) r dr d\theta \quad (2.26)$$

for some coefficients b_i . However, using the symmetry properties of the associated

Legendre functions, it can be shown that the frequency shift $\delta\omega_{n\ell m}$ arising from rotation is an odd function of m , and hence only the odd a -coefficients will be nonzero. Therefore we can write

$$a_{2s+1}(n, \ell) = \int_0^\pi \int_0^R K_{n\ell s}(r, \theta) \Omega(r, \theta) r dr d\theta \quad (2.27)$$

where the $K_{n\ell s}$ are calculated from the $K_{n\ell m}$ using the odd b_i . Note that actual measurements do result in even a -coefficients as well. These arise from asphericities in solar structure and possibly from magnetic fields.

Since the P_ℓ^m and their derivatives are always either even or odd functions of $x = \cos \theta$, it can be shown that the kernels are always symmetric around the equator, $\theta = \pi/2$. Hence, the odd a -coefficients are only sensitive to the symmetric part of $\Omega(r, \theta)$. This has the consequence that a global-mode inversion for rotation cannot detect any difference between the hemispheres. In the next chapter we shall see how such an inversion might be performed.

Not only does rotation shift the mode frequencies, but it also perturbs the horizontal eigenfunctions themselves. For an analysis performed using the spherical harmonics (the unperturbed eigenfunctions), this will cause coupling between the modes. The next chapter shall also discuss how this fact is used when fitting the mode frequencies.

Chapter 3

Analysis of Data from the MDI Medium- ℓ Program

In the preceding chapter I gave an outline of the mathematics connecting observed mode parameters to physical inferences of the solar interior. This chapter deals with how these parameters might be accurately determined. It first appeared as Improved Helioseismic Analysis of Medium- ℓ Data from the Michelson Doppler Imager in Volume 290, Issue 11, of *Solar Physics*, coauthored with Jesper Schou. The final publication is available at Springer via <http://dx.doi.org/10.1007/s11207-015-0792-y>. Here I have removed the abstract and appendix, as well as corrected one typo in the second sentence of section 2, where “2001” was replaced by “2011”. I wrote all the text and performed all the analysis presented here, with the exception of the original analysis performed by Jesper Schou, who also wrote several of the core routines.

3.1 Introduction

The *Michelson Doppler Imager* (MDI: Scherrer *et al.*, 1995) onboard the *Solar and Heliospheric Observatory* (SOHO) took data from December 1995 to April 2011. Equipped with a 1024×1024 CCD, it was capable (in full-disk mode) of sending down dopplergrams with a spatial resolution of 2.0 arcsec per pixel at a cadence of 60 seconds using the NiI 6768 Å spectral line. However, due to telemetry constraints,

MDI was operated in full-disk mode for only a few months total each year. For the rest of the time, we have only data that were convolved in each direction onboard the spacecraft with a gaussian vector of 21 integers, subsampled by a factor of five, and cropped to 90% of the average image radius in order to fit into the available telemetry bandwidth. It was these dopplergrams that comprised the Medium- ℓ Program and acquired the label of \mathbf{vw}_V for “vector-weighted velocity”. The \mathbf{vw}_V data were the input to all of the analysis described here. For overviews of global mode helioseismology, the reader is referred to Christensen-Dalsgaard (2004) and Gough (2013).

Dopplergrams are decomposed into spherical harmonic components described by their degree [ℓ] and azimuthal order [m], which are formed into timeseries and Fourier transformed. We work in the medium- ℓ regime, which is defined as the range where peaks in the power spectrum, corresponding to the oscillation modes, are well-separated from those of different degrees. Sets of modes with the same radial order [n] form ridges; modes with $n = 0$ are labelled f -modes, and those with $n > 0$ are labelled p -modes. The medium- ℓ regime is conventionally taken to be $\ell \leq 300$ for the f -modes and $\ell \leq 200$ for the p -modes. The Fourier transforms are fit to yield the mode frequencies (among other parameters) for multiplets described by ℓ and n . In a spherically symmetric Sun, the frequency would be the same for all m . Asphericities such as rotation lift this degeneracy, and the variation of frequency with m can be fit by a polynomial, resulting in the so-called a -coefficients (see Section 3.3.3). The frequencies and a -coefficients can be inverted to infer the sound speed or angular velocity in the solar interior as a function of latitude and radius. In this work we have used the odd a -coefficients to perform regularized least squares (RLS) inversions for angular velocity. The RLS method attempts to balance fitting the data with the smoothness of the solution, since the inverse problem is ill-posed (Schou, Christensen-Dalsgaard, and Thompson, 1994).

With an internal-rotation profile in hand, one can compute the corresponding a -coefficients. These inferred a -coefficients represent a fit to the measured a -coefficients. We can use the residuals of this fit to investigate potential systematic errors in the a -coefficients. One problem with the original analysis can be seen in Figure 3.1, which

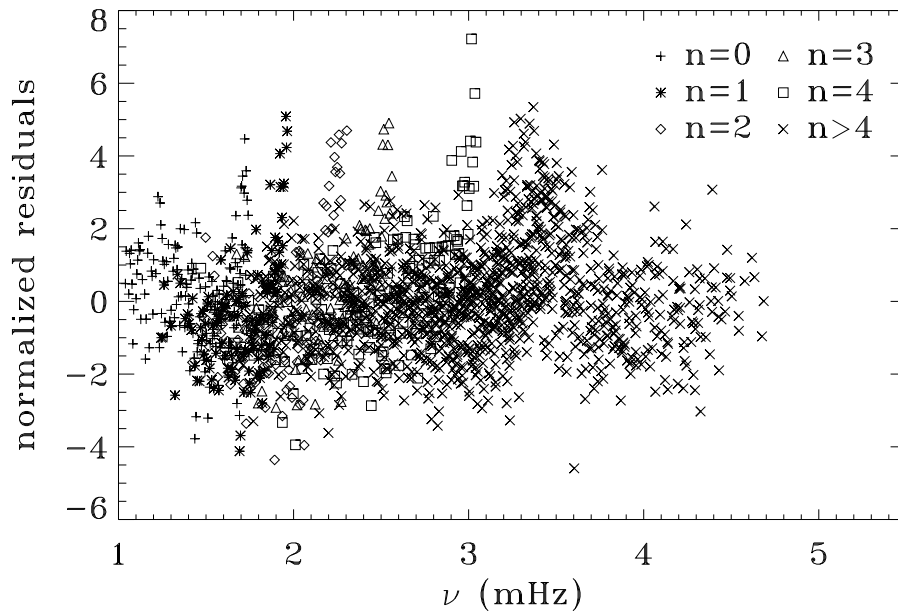


Figure 3.1: Residuals of a_3 coefficients normalized by their errors as a function of frequency for the 72-day interval beginning on 8 January 2004.

presents the normalized residuals of a_3 . If the model were a good fit to the data, one would expect these to be normally distributed around zero with unit variance. A significant deviation from this expectation is the “bump” at around 3.4 mHz, which can be seen in all of the odd a -coefficients and their residuals, and alternates in sign between them. Furthermore, the shape of the bump depends on the width of the frequency interval used in the mode fitting, which by itself indicates a problem with the fits (Schou *et al.*, 2002). Also visible in this plot are deviations from a continuous function at the ends of ridges. This feature, known as “horns”, is visible in several of the mode parameters and is not reproducible by any reasonable internal-rotation profile (see Section 3.4.2). In the new analysis, the residuals have been substantially reduced, but the fact that they are still quite large indicates that the errors are still dominated by systematics (see Section 3.4.2).

In parallel to the MDI analysis, the *Global Oscillation Network Group* (GONG: Harvey *et al.*, 1996) has done an independent medium- ℓ analysis of dopplergrams

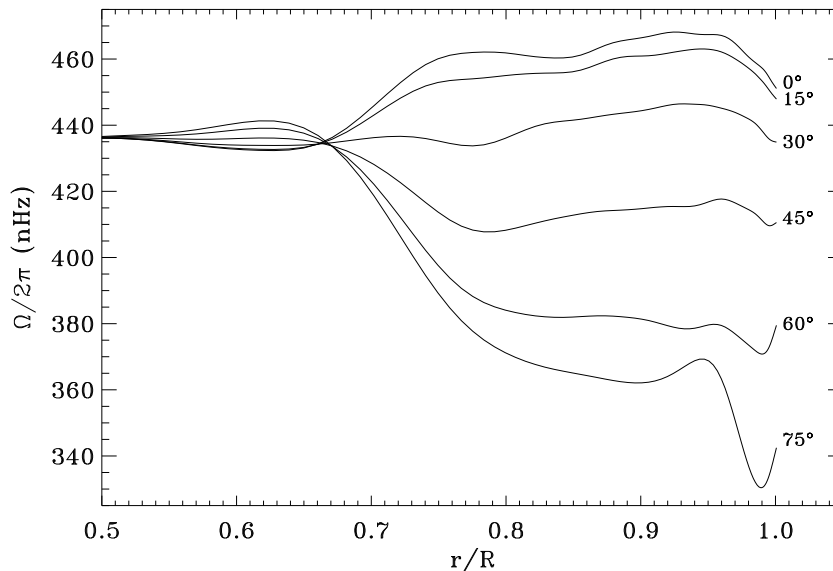


Figure 3.2: Rotation profile for the same time interval shown in Figure 3.1. The curves correspond to the latitudes indicated.

taken from six ground-based observatories (the GONG network), using the same spectral line and cadence as MDI. Although the two analyses are generally in good agreement, in certain areas the inferences drawn by the two projects differ by more than their errors. In particular, the above-mentioned bump is absent in the GONG analysis. Likewise, the MDI analysis indicates a polar jet at a latitude of about 75° , shown in Figure 3.2, which is not seen in the GONG analysis. Excluding the modes that contribute to the bump does not remove this high-latitude jet. Although the jet may be a real feature, the fact that it is not seen in the full-disk analysis of MDI data makes this questionable (Larson and Schou, 2009). Until such discrepancies can be resolved, the analysis results must remain in doubt, and the issue has been studied at length by several investigators with little success (Schou *et al.*, 2002).

Another apparent systematic error seen in the original MDI analysis is a one-year periodicity in the fractional change in the seismic radius of the Sun (see Figure 3.3), which is proportional to the fractional change in f -mode frequencies (Antia *et al.*, 2001). This cannot be studied with the GONG results because they do not fit enough

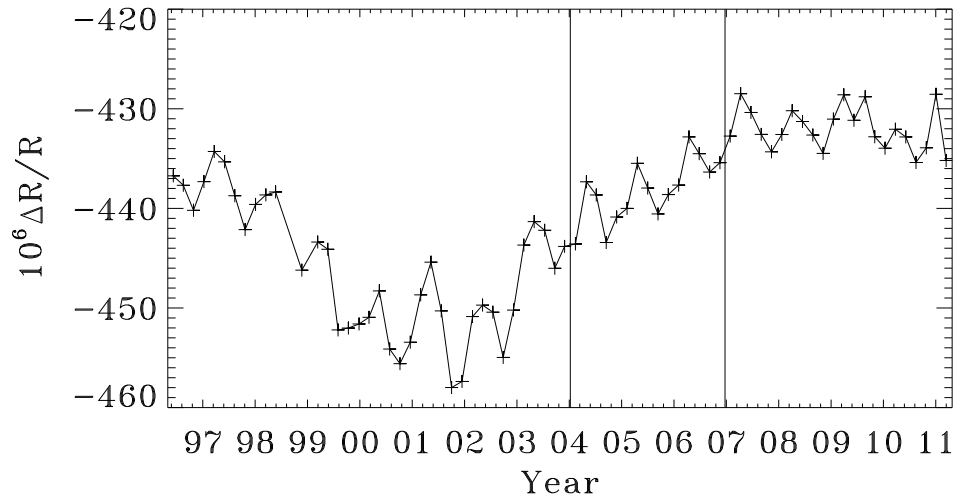


Figure 3.3: Fractional difference in seismic radius between observations and a model as a function of time, averaged over all degrees ℓ . Vertical lines indicate the three years that we reanalyzed for each change in the processing (see Section 3.2).

f -modes, while the MDI full-disk data do not help either since they are only taken for approximately one time interval (long enough for global analysis) per year. Although it was presumed that this effect had to do with an annual variation in leakage (see Section 3.3) between the modes, early investigations revealed that using a corrected B_0 , P_{eff}^1 , and solar radius did not make a substantial difference (Schou and Bogart, 2002).

It was to address all of these issues that a reanalysis of the medium- ℓ data was undertaken. The original analysis was in general very successful, but it is based on certain approximations. Physical effects such as mode profile asymmetry (Duvall *et al.*, 1993), horizontal displacement of the near surface matter, distortion of eigenfunctions by the differential rotation (Woodard, 1989), and a potential error in the orientation of the Sun’s rotation axis as given by the Carrington elements (Beck and Giles, 2005), were not taken into account. Likewise, instrumental effects such as cubic distortion from the optics (see Section 3.3.1), misalignment of the CCD with the solar

¹The angle P_{eff} is the effective P -angle, which is the angle between the solar-rotation axis and the column direction on the CCD; the angle B_0 is the heliographic latitude of the sub-observer point.

rotation axis, an alleged CCD tilt with respect to the focal plane, and image-scale errors were ignored (Korzennik, Rabello-Soares, and Schou, 2004). Furthermore, new algorithms for generating the window functions, detrending the timeseries, and filling the gaps had become available. We updated the data analysis to include each of these considerations in turn to see what effect, if any, they had on the mode parameters and systematic errors.

In the next section we describe the datasets that we analyzed and how. In Section 3.3 we give a detailed description of all of the steps in the data analysis. Section 3.4 describes the effects of the various changes in the analysis. Section 3.5 discusses these results and gives prospects for the future. This work elaborates on and updates our earlier work on the subject (Larson and Schou, 2008).

3.2 Data

The line-of-sight velocity data were initially (Schou, 1999) analyzed in 74 timeseries of length 72 days, beginning 1 May 1996 00:00:00_TAI. The last data point used was at 12 April 2011 23:20:00_TAI. In late June 1998, however, contact with SOHO was lost, resulting in a gap of more than 108 days. This was followed by a period of about two months of usable data at the end of 1998, and then another gap of more than 36 days. Therefore the 12th timeseries is offset from the others by 36 days and begins $12 \times 72 + 36 = 900$ days after the first, while the 13th timeseries begins $14 \times 72 = 1008$ days after the first, as shown in Table 3.1 (note the low duty cycles around MDI mission day number 2116). We have reanalyzed these same 74 time intervals, as well as used them to make 360-day long timeseries. Therefore only three of the 72-day long timeseries were used to make the third 360-day long timeseries, and the last 72-day long timeseries was unused in the 360-day analysis. Timeseries (and other final data products) are available for download from Stanford's Joint Science Operation Center (JSOC). See the Appendix for details.

To see the effect of the various changes in the processing, we apply them one by one to the analysis of 15 timeseries covering a period of three years beginning on 8 January 2004 00:00:00_TAI. This is long enough to see an annual component in

Table 3.1: Timeseries used. Day numbers are given relative to the MDI epoch of 1 January 1993 00:00:00_TAI. Both these and the dates refer to the first day of the timeseries, and all timeseries begin on the first minute of the day. Duty cycles are given for the original timeseries (DC0), the final timeseries (DC1), and the final timeseries after gapfilling (DC2). The difference DC0–DC1 tends to be positive at the beginning of the mission (at most 0.031) and negative at the end (not less than -0.02).

Day	Date	DC0	DC1	DC2	Day	Date	DC0	DC1	DC2
1216	01 May 1996	0.895	0.888	0.907	4024	08 Jan 2004	0.986	0.991	1.000
1288	12 Jul 1996	0.964	0.949	0.966	4096	20 Mar 2004	0.782	0.770	0.858
1360	22 Sep 1996	0.964	0.954	0.969	4168	31 May 2004	0.897	0.898	0.989
1432	03 Dec 1996	0.976	0.962	0.982	4240	11 Aug 2004	0.853	0.852	0.941
1504	13 Feb 1997	0.952	0.950	0.964	4312	22 Oct 2004	0.969	0.968	0.981
1576	26 Apr 1997	0.981	0.981	1.000	4384	02 Jan 2005	0.991	0.991	1.000
1648	07 Jul 1997	0.970	0.976	0.986	4456	15 Mar 2005	0.991	0.992	0.996
1720	17 Sep 1997	0.973	0.965	0.976	4528	26 May 2005	0.983	0.989	1.000
1792	28 Nov 1997	0.979	0.982	1.000	4600	06 Aug 2005	0.989	0.988	0.996
1864	08 Feb 1998	0.969	0.968	0.976	4672	17 Oct 2005	0.985	0.985	0.996
1936	08 Apr 1998	0.884	0.883	0.896	4744	28 Dec 2005	0.988	0.992	1.000
2116	18 Oct 1998	0.731	0.726	0.737	4816	10 Mar 2006	0.990	0.992	1.000
2224	03 Feb 1999	0.894	0.885	0.894	4888	21 May 2006	0.962	0.971	0.978
2296	16 Apr 1999	0.982	0.974	0.986	4960	01 Aug 2006	0.988	0.992	1.000
2368	27 Jun 1999	0.986	0.987	1.000	5032	12 Oct 2006	0.990	0.991	1.000
2440	07 Sep 1999	0.930	0.917	0.941	5104	23 Dec 2006	0.895	0.900	0.907
2512	18 Nov 1999	0.870	0.839	0.852	5176	05 Mar 2007	0.976	0.977	0.986
2584	29 Jan 2000	0.986	0.983	0.989	5248	16 May 2007	0.985	0.984	0.994
2656	10 Apr 2000	0.994	0.994	1.000	5320	27 Jul 2007	0.988	0.991	1.000
2728	21 Jun 2000	0.988	0.988	0.996	5392	07 Oct 2007	0.965	0.968	0.980
2800	01 Sep 2000	0.986	0.984	0.995	5464	18 Dec 2007	0.985	0.987	1.000
2872	12 Nov 2000	0.947	0.937	0.945	5536	28 Feb 2008	0.996	0.996	1.000
2944	23 Jan 2001	0.985	0.986	1.000	5608	10 May 2008	0.989	0.993	1.000
3016	05 Apr 2001	0.990	0.990	1.000	5680	21 Jul 2008	0.988	0.991	1.000
3088	16 Jun 2001	0.964	0.961	0.975	5752	01 Oct 2008	0.983	0.986	0.994
3160	27 Aug 2001	0.991	0.991	1.000	5824	12 Dec 2008	0.983	0.989	1.000
3232	07 Nov 2001	0.971	0.970	0.979	5896	22 Feb 2009	0.996	0.996	1.000
3304	18 Jan 2002	0.859	0.862	0.870	5968	05 May 2009	0.951	0.954	0.960
3376	31 Mar 2002	0.987	0.985	1.000	6040	16 Jul 2009	0.709	0.729	0.736
3448	11 Jun 2002	0.978	0.984	0.996	6112	26 Sep 2009	0.985	0.989	0.996
3520	22 Aug 2002	0.991	0.990	1.000	6184	07 Dec 2009	0.989	0.993	1.000
3592	02 Nov 2002	0.994	0.994	1.000	6256	17 Feb 2010	0.992	0.993	1.000
3664	13 Jan 2003	0.992	0.989	1.000	6328	30 Apr 2010	0.988	0.995	1.000
3736	26 Mar 2003	0.982	0.982	0.996	6400	11 Jul 2010	0.952	0.961	0.971
3808	06 Jun 2003	0.822	0.826	0.852	6472	21 Sep 2010	0.879	0.881	0.929
3880	17 Aug 2003	0.981	0.981	0.996	6544	02 Dec 2010	0.732	0.744	0.753
3952	28 Oct 2003	0.878	0.878	0.952	6616	02 Feb 2011	0.812	0.812	0.822

the f -mode frequencies, but short enough to approximate the solar-cycle variation as linear during its declining phase. Beginning with the image-scale correction, we then apply, in order, corrections for the cubic distortion from the instrument optics, the misalignment of the CCD, the inclination error, and the suspected CCD tilt. These are all the corrections that we made during the spherical harmonic decomposition, and we regenerate timeseries for the entire mission with all of them applied. The next two improvements applied are to the detrending and then the gapfilling. Again, detrended and gapfilled timeseries have been regenerated for the entire mission. For the 360-day analysis, the timeseries were created by concatenating the detrended and gapfilled 72-day long timeseries. The remaining changes to the processing all take place in the fitting. We first take into account the horizontal component of the displacement, and then distortion of eigenfunctions by the differential rotation (known as the “Woodard effect”, see Section 3.3.3). Mode parameters for the entire mission have been recomputed with these applied, using first a symmetric mode profile and again using an asymmetric one. This sequence of corrections is summarized in Table 3.2.

3.3 Method

Analysis proceeds as follows. An observed oscillation mode is taken as proportional to the real part of a spherical harmonic given by $Y_\ell^m(\phi, \theta) = P_\ell^m(\cos \theta)e^{im\phi}$, where the P_ℓ^m are associated Legendre functions normalized such that

$$\int_{-1}^1 [P_\ell^m(x)]^2 dx = 1 \quad (3.1)$$

and with the property that $P_\ell^{-m} = P_\ell^m = P_\ell^{|m|}$. As used here, ℓ and m are integers with $\ell \geq 0$ and $-\ell \leq m \leq \ell$. However, since spherical harmonics with negative m are the complex conjugates of those with positive m , we only compute coefficients for $m \geq 0$. For medium- ℓ analysis, we use degrees up to $\ell = 300$. Beyond this, peaks along the f -mode ridge begin to blend into each other. For the p -modes, this is already happening around $\ell = 200$ or below.

To efficiently compute the spherical harmonic coefficients, each image is remapped to a uniform grid in longitude and $\sin(\text{latitude})$ using a cubic convolution interpolation, and apodized with a cosine in fractional image radius from 0.83 to 0.87. The grid rotates at a constant rate of 1/year so that the apparent rotation rate of the Sun remains constant. The resulting map is Fourier transformed in longitude and for each m a scalar product is taken with a set of associated Legendre functions of $\sin(\text{latitude})$, which yields the complex amplitudes of the spherical harmonics as a function of ℓ and m in the ranges given above. These amplitudes are arranged into timeseries 72 days long, and the timeseries for each ℓ and m is detrended, gapfilled, and Fourier transformed, at which point the positive frequency part of the transform is identified with negative m and the conjugate of the negative frequency part is identified with positive m . The Fourier transforms are fit (a process that has become known as peakbagging), resulting in a mode frequency, amplitude, linewidth, and background for each ℓ and n . The m -dependence of the frequencies is parameterized by the a -coefficients, which are fit for directly in the peakbagging, with the other mode parameters assumed to be the same for all m .

Because of leakage between the modes, predominantly caused both by projection onto the line of sight and by our inability to see most of the Sun, the Fourier transform of the target ℓ and m contain peaks from neighboring modes as well, which have to be accounted for in the peakbagging. This is done through the so-called leakage matrix, which quantifies the amplitude of each mode as it appears in the observed spectra. The leakage matrix is calculated by generating artificial images containing spherical harmonics and their relevant horizontal derivatives, projected onto the line of sight, and decomposing them in the same way as the the actual data. The same leakage matrix has been used for all times (see Section 3.3.3).

3.3.1 Spherical Harmonic Transform

Since spherical harmonic decomposition begins with a remapping, it gives us an opportunity to apply certain corrections to the data. The most significant of these is to correct for the image scale, which is the number of arcseconds corresponding to each

pixel of the detector. Although assumed to be a constant in the original analysis, changes in the instrument with temperature and over time actually caused it to vary. The radius of the solar image on the MDI detector, measured in pixels, is assumed to be given by $\arcsin(D/R_{\text{ref}})$ divided by the image scale, where D is the observer distance and R_{ref} is defined as 696 Mm. Hence the original value used for the solar radius in pixels was in error. In the current analysis the image scale is given by a multiplicative factor times the original constant image scale of 1.97784 arcsec per pixel. The inverse of this factor (hence the radius correction) is given as a function of time t by

$$f(t) = b_0 + D[b_1 + b_2(t - t_0) + b_3(t - t_0)^2]. \quad (3.2)$$

The parameters b_0 , b_1 , b_2 , b_3 , and t_0 result from a fit to $(A_{\text{major}} + A_{\text{minor}})/(2R_0)$, where A_{major} and A_{minor} are the lengths of the major and minor axes of the solar image returned by the routine used to fit the solar limb and R_0 is the original value used for the solar radius in pixels (Keh-Cheng Chu, private communication, 2001). The parameters of the fit change throughout the mission, typically at a focus change. Hence the radius correction is a piecewise-continuous function.

To account for distortion from the instrument optics, we apply a correction given by an axisymmetric cubic distortion model (Korzennik, Rabello-Soares, and Schou, 2004). Such a model gives the distorted coordinate as a cubic function of the undistorted one. In our implementation, the fractional change in coordinates is given by $C_{\text{dist}}(r^2 - R^2)$, where r is the distance from the center of the CCD, R is the (updated) radius of the solar image, and all quantities are given in terms of full-disk pixels. For C_{dist} we have used 7.06×10^{-9} , which was derived from a ray-trace of the MDI instrument. This differs from the value used by Korzennik, Rabello-Soares, and Schou (2004), which resulted from a different model. It is unclear how to resolve the discrepancy, but ongoing investigation of the MDI distortion is likely to help.

For P_{eff} and B_0 we apply a simple sinusoidal correction with respect to time. Since the error of the ascending node position is not significant (Beck and Giles, 2005), if δI is the error of the inclination and δP is the error on P_{eff} resulting from misalignment

of the CCD, then the new values are given by

$$B'_0 = B_0 + \delta I \sin[2\pi(t_{\text{obs}} - t_{\text{ref}})] \quad (3.3)$$

and

$$P'_{\text{eff}} = P_{\text{eff}} + \delta P + \delta I \cos[2\pi(t_{\text{obs}} - t_{\text{ref}})] \quad (3.4)$$

where t_{obs} is the observation time and t_{ref} is a time when B_0 is zero, both measured in years. For t_{ref} we have used 6 June 2001 06:57:22_TAI. For the value of δP we have used -0.2° , which agrees with values obtained both by cross-correlations with GONG images and from the Mercury transit in November 1999 (Cliff Toner, private communication, 2004). For the value of δI we have used -0.1° , a value derived by Beck and Giles (2005).

The ellipticity of the observed solar image is much greater than the actual ellipticity of the Sun. A possible explanation is that the CCD is not perpendicular to the optical axis of the instrument. To correct for this image distortion, we follow the prescription given in the appendix of Korzennik, Rabello-Soares, and Schou (2004). The required parameters are the amount $[\beta]$ to rotate the x -axis to give the direction around which the CCD is tilted, the amount of the tilt $[\alpha]$, and the effective focal length $[f_{\text{eff}}]$. We have adopted the values $\beta = 56.0^\circ$, $\alpha = 2.59^\circ$, $f_{\text{eff}} = 12972.629$ pixels, which are consistent with the values found by the above-mentioned authors. Although there is some doubt as to whether the CCD is actually tilted, the model still reproduces the observed ellipticity reasonably well (see Korzennik, Rabello-Soares, and Schou (2004)).

3.3.2 Detrending and Gapfilling

Once the 72-day long timeseries have been assembled, the next step in the processing is the evaluation of the window function. As used here, the window function is a timeseries of zeros and ones that identifies both missing data and data that should be rejected on the basis of quality; only time points corresponding to ones in the window function will be used in the subsequent processing. In the original analysis, the $\ell = 0$

timeseries was examined to ensure that gaps resulting from known spacecraft and instrument events were accurately reflected in the timeseries generated. These events included such things as station keeping, momentum management, problems with the ground antennas, emergency Sun reacquisitions (ESRs), and tuning changes due to instrumental drifts. Additionally, any day whose duty cycle was less than 95% was investigated to ensure that all potentially available data were processed in the spherical harmonic decomposition step. Unfortunately, the original analysis employed a simple algorithm that performed detrending of the timeseries on full mission days only, thus requiring any day that contained a discontinuity in the data, such as those caused by instrument tuning changes, to have its window function zeroed to the nearest day boundary. Also, the instrument occasionally stopped taking images, which caused thermal transients after it restarted until equilibrium was reestablished. These turn-on transients, and other data deemed unusable, were also manually identified in the timeseries and set to zero in the window function. Then, ten timeseries were examined and thresholds on acceptable values in them were set by hand in order to reject outliers. These ten timeseries are the real parts of $\ell = 0, m = 0$; $\ell = 1, m = 0$; $\ell = 1, m = 1$; the imaginary part of $\ell = 1, m = 1$; and the sum over m of the real part squared plus the imaginary part squared for $\ell = 1, 2, 5, 10, 20$, and 50.

In the new analysis, we use the old $\ell = 0$ timeseries, since they had already been examined, to confirm the legitimacy of any data missing in the new $\ell = 0$ timeseries. We then automatically set to zero in the window function any point where the Image Stabilization System (ISS) was off, as derived from housekeeping data. Next we form ten timeseries in the same fashion as the original analysis, but we replace squaring the real and imaginary parts in the sum over m with taking the absolute value of the real and imaginary parts, and then subtract a 41 point running median. This enables us to remove outliers by taking the rms excluding the top and bottom 1% of the data, and rejecting any points that differ from zero by more than 6.0 times this rms.

In the new analysis, the discontinuities, which were typically caused by tuning changes, spacecraft rolls, and any event that powered down the instrument, all had

to be identified by hand. This information has to be available for the median filtering, and subsequent detrending can now be done on entire continuous sections of data irrespective of day boundaries. Further, the beginning of every section is automatically checked for the existence of thermal transients in the $\ell = 0$ timeseries by fitting a sum of two decaying exponentials and a constant. We do not fit the decay constants as part of this check. Rather, we fit for them only once and hold them fixed at values of 15 and 60 minutes. The use of two exponentials comes from a model of the instrument. The window function is zeroed wherever the first two terms of the fit differ from zero by more than the rms of the median-subtracted $\ell = 0$ timeseries. Also, by defining sections, we were able to manually reject any data lying in between the sections, if such were deemed necessary. In the new analysis, defining the sections of continuous data was the only operation that required human attention, and had to be done only once.

Detrending in the original analysis was performed on whole mission days (1440 time points) by fitting a Legendre polynomial of degree given by $2 + N_{\text{span}}/300$ where N_{span} is the number of minutes spanned by the available data and the division truncates to the next lowest integer. This polynomial was subtracted prior to gapfilling, which was also independently performed on each mission day. The algorithm used would compute an autoregressive model from the data and use it to fill gaps up to a maximum size of five points. It required six points either before or after each gap to do so, regardless of the size of the gap.

Detrending in the new analysis is done by fitting a Legendre polynomial of degree seven to an interval of data spanning 1600 minutes, which is advanced by 1440 minutes for each fit. In other words, the detrending intervals overlap by 160 points. The polynomials are stitched together in the overlap region by apodizing each of them with a \cos^2 curve. In the case that the data points in a detrending interval spanned less than 800 minutes, the Legendre polynomial was recomputed for the shorter span, and the fit was not apodized. The resulting function is subtracted from the data to yield a timeseries with a mean of zero.

In the new analysis, gaps are filled using an autoregressive algorithm based on the work of Fahlman and Ulrych (1982). This method predicts values for the missing

data based on the spectral content of the data present. Each point in the known data is expressed as a linear combination of the N preceding and following points, where N is the order of the autoregressive model, the coefficients of which are found by minimizing the prediction error in the least-squares sense. Hence, the order of the model can be no greater than the number of points in the shortest section of data. If a model of a certain order is desired, it imposes a lower limit on the length of data sections that can be used to generate it. In our implementation, we always use the highest order such that at least 90% of the data will be used to generate the model, up to a maximum order of 360. It was found that increasing the model order beyond this value did not result in significantly better predictions². Once the model is known, the gaps are filled by minimizing the prediction error in the least-squares sense, this time with respect to the unknown data values. The innovation over the method of Fahlman and Ulrych is that all gaps shorter than the model order within each filling interval are filled simultaneously. Gaps longer than the model order are not filled. Gaps at the beginning or end of the timeseries are not filled regardless of their length, because the choice was made not to extrapolate the timeseries. The model order may possibly then be increased by using the filled values as known data, and the process is repeated, but using the original gap structure. That is, the gaps that were filled on the first iteration will be filled again using the new model. If the model order did not change, or if all the gaps were already filled in the first iteration, the process stops after two iterations. Otherwise a final iteration is run wherein a new model is computed using the newly filled values, and the gaps are filled one last time (Rasmus Larsen, private communication, 2013). Lastly, a new window function is generated to reflect the filled gaps.

²Since the coefficients of a model of order N are determined from a model of order $N - 1$, our algorithm may truncate the model if the ratio of the prediction error to the variance of the timeseries drops below $\sim 1.2 \times 10^{-6}$ as the model order is increased. However, this never occurred while gapfilling the MDI dataset.

3.3.3 Peakbagging

Fourier transforms of the gapfilled timeseries are fit using a maximum-likelihood technique, taking into account leakage between the modes. In this section we expand upon the presentation given by Schou (1992) and describe the fitting process as it is currently implemented. When modelling an oscillation mode as a stochastically excited damped oscillator, both the real and imaginary parts of the Fourier transform will be normally distributed with a mean of zero. The variance due to the mode will be given by

$$v(\nu_0, w, A, \nu) = \frac{2wA^2}{w^2 + 4(\nu - \nu_0)^2} \quad (3.5)$$

where ν_0 is the frequency of the mode, w is the full width at half maximum, and A is the amplitude (A^2 is a measure of the total power in the mode). To fit an actual observed spectrum, one must also add a background term; our treatment of the background is described below. Furthermore, to account for the redistribution of power caused by gaps in the timeseries, this model will be convolved with the power spectrum of the window function (Anderson, Duvall, and Jefferies, 1990). If x is the real part of the observed value of the Fourier transform, then the probability density for the i th frequency bin in the real part will be given by

$$P_{\text{real}}(\nu_0, w, A, \nu_i) = \frac{1}{\sqrt{2\pi v(\nu_i)}} \exp\left(-\frac{x(\nu_i)^2}{2v(\nu_i)}\right) \quad (3.6)$$

and likewise for P_{imag} with x replaced by y , the imaginary part. The total probability density for the i th bin is then $P = P_{\text{real}}P_{\text{imag}}$. In these equations the mode parameters, and hence v , are functions of n , ℓ , and m ; we have suppressed their dependence on these for conciseness.

The idea behind the maximum-likelihood approach is to maximize the joint probability density of a given mode, which is given by a product of individual probability densities over a suitable number of frequency bins (assuming that each frequency bin is independent, which is not strictly true in the presence of gaps). This is equivalent to minimizing the negative logarithm of this product, which, except for constants, is

given by

$$S(\nu_0, w, A) = \sum_i \ln(v(\nu_i)) + \frac{x(\nu_i)^2 + y(\nu_i)^2}{v(\nu_i)}. \quad (3.7)$$

where ν_i is the frequency of the i th frequency bin. For a given value of ℓ , there will be $2\ell + 1$ values of m . Rather than fitting each m separately, we will maximize the joint probability density of all of them together. To do so, we assume that the width and amplitude are independent of m and estimate the variation of the background with m from the spectrum far from the peaks. We redefine ν_0 as the mean multiplet frequency for each n and ℓ , and expand the frequency dependence on m as

$$\nu_{n\ell m} = \nu_0(n, \ell) + \sum_{i=1}^{N_a} a_i(n, \ell) \mathcal{P}_i^\ell(m) \quad (3.8)$$

where the polynomials $[\mathcal{P}]$ are those used by Schou, Christensen-Dalsgaard, and Thompson (1994), and the coefficients $[a_i]$ are fit for directly. The a_1 coefficient will have 31.7 nHz added to correct for the average orbital frequency of the Earth about the Sun. In what follows, we will label the set of parameters upon which S depends using the vector \mathbf{p} . This will include ν_0 , w , A , N_a a -coefficients, a background parameter (described below), and optionally a parameter to describe the asymmetry (also described below), for each n and ℓ .

Due to leakage between the modes, the observed timeseries and Fourier transforms are a superposition of the true underlying oscillations. The observed timeseries for a given ℓ and m will be given by

$$o_{\ell m}(t) = \sum_{n'\ell'm'} c_{\ell m, \ell' m'}^{RR} \text{Re}[a_{n'\ell'm'}(t)] + i c_{\ell m, \ell' m'}^{II} \text{Im}[a_{n'\ell'm'}(t)] \quad (3.9)$$

where $a(t)$ is the complex amplitude of the underlying timeseries, and $\text{Re}[\]$ and $\text{Im}[\]$ denote the real and imaginary parts, respectively. The sensitivity coefficients c^{RR} and c^{II} give the real-to-real leaks and imaginary-to-imaginary leaks respectively. Approximate expressions for the radial contribution to these coefficients are given by Schou and Brown (1994). Under the same approximations, it can be shown that the real-to-imaginary and imaginary-to-real leaks are identically zero for geometries that

are symmetric around the central meridian. Although these are still assumed to be zero for the current work, c^{RR} and c^{II} are computed as described below. It can also be shown under these assumptions that

$$\begin{aligned}
c_{\ell m, \ell' m'}^{RR} &= c_{\ell' m', \ell m}^{RR} \\
c_{\ell m, \ell' m'}^{II} &= c_{\ell' m', \ell m}^{II} \\
c_{\ell(-m), \ell' m'}^{RR} &= c_{\ell m, \ell' m'}^{RR} \\
c_{\ell(-m), \ell' m'}^{II} &= -c_{\ell m, \ell' m'}^{II}
\end{aligned} \tag{3.10}$$

and that $c^{RR} = c^{II} = 0$ when $\ell + m + \ell' + m'$ is odd. Note that since the spherical harmonic decomposition is not able to separate the different values of n , we have suppressed the n -dependence of the leaks in these equations. Later we will consider effects that cause the leaks to vary with n . In frequency space, the observed Fourier transform can then be expressed as

$$\tilde{o}_{\ell m}(\nu) = x_{\ell m}(\nu) + iy_{\ell m}(\nu) = \sum_{n' \ell' m'} C_{\ell m, \ell' m'} \tilde{a}_{n' \ell' m'}(\nu) \tag{3.11}$$

where $C = (c^{RR} + c^{II})/2$ (Schou and Brown, 1994). Although in principle the sum above should be over all modes, for a given ℓ and m , only modes in a certain range in ℓ' and m' will have significant leakage. Therefore the sum in Equation 3.11 need only be over modes that may have appreciable amplitudes within the fitting window. For this work we have used $\Delta\ell = \ell - \ell'$ in the range ± 6 and $\Delta m = m - m'$ in the range ± 15 . Furthermore, we neglect leaks for $\Delta\ell + \Delta m$ odd or which are estimated to be far away in frequency. Since the modes on the Sun are uncorrelated with each other, the elements of the covariance matrix between the different transforms at each frequency point will be given by

$$\begin{aligned}
E_{\ell m, \ell' m'}^{\text{modes}}(\nu_i) &= \text{Cov}[x_{\ell m}(\nu_i), x_{\ell' m'}(\nu_i)] = \text{Cov}[y_{\ell m}(\nu_i), y_{\ell' m'}(\nu_i)] \\
&= \sum_{n'' \ell'' m''} C_{\ell m, \ell'' m''} C_{\ell' m', \ell'' m''} v_{n'' \ell'' m''}(\mathbf{p}, \nu_i).
\end{aligned} \tag{3.12}$$

The total covariance will be the sum of the covariance between the modes and the

covariance of the noise. Since we fit each ℓ separately and all m for that ℓ simultaneously, the elements of the covariance matrix $[\mathbf{E}]$ used in the fitting are given by

$$E_{m,m'}(\nu_i) = E_{m,m'}^{\text{modes}}(\nu_i) + \tilde{E}_{m,m'} \frac{\nu_B}{\nu_i} e^b \quad (3.13)$$

where $\tilde{E}_{m,m'}$ is the measured covariance between m and m' in the frequency range 7638.9 to 8217.6 μHz , ν_B is a constant, and b is a free parameter determined in the fit. Due to our choice of normalization, e^b is proportional to the length of the timeseries. The probability density for a frequency bin then becomes

$$P(\mathbf{p}, \nu_i) = \frac{1}{|2\pi\mathbf{E}(\mathbf{p}, \nu_i)|} \exp \left[-\frac{1}{2} (\mathbf{x}(\nu_i)^T \mathbf{E}(\mathbf{p}, \nu_i) \mathbf{x}(\nu_i) + \mathbf{y}(\nu_i)^T \mathbf{E}(\mathbf{p}, \nu_i) \mathbf{y}(\nu_i)) \right] \quad (3.14)$$

and the function to minimize becomes

$$S(\mathbf{p}) = \sum_i \ln |\mathbf{E}(\mathbf{p}, \nu_i)| + \mathbf{x}(\nu_i)^T \mathbf{E}(\mathbf{p}, \nu_i) \mathbf{x}(\nu_i) + \mathbf{y}(\nu_i)^T \mathbf{E}(\mathbf{p}, \nu_i) \mathbf{y}(\nu_i) \quad (3.15)$$

where $|\cdot|$ denotes the determinant, \mathbf{x} is a vector of the $2\ell + 1$ real parts of the transforms, and \mathbf{y} is a vector of the $2\ell + 1$ imaginary parts. Note that \mathbf{p} , \mathbf{x} , and \mathbf{y} are implicit functions of n and ℓ (the dependence of \mathbf{x} and \mathbf{y} on n come from the frequency range chosen for the fitting window). For the width of the fitting window we have chosen 5.0 times the estimated width of the peak, with a minimum of 2.9 μHz and a maximum of 81.0 μHz . The minimum ensures that we always have enough points in frequency for the fit to be stable, and the maximum serves to limit the computational burden. The peakbagging will yield the mode parameters specified by \mathbf{p} for each multiplet that it is able to fit, as well as error estimates on these, generically referred to as σ . The errors are estimated from the inverse of the Hessian matrix at the minimum of S . For readability, the error estimates for the a -coefficients will be labelled by σ_i , while the rest will be designated in the usual way.

The minimization scheme used is a variation of the Levenberg–Marquardt method. For further details, such as approximations made in the calculation of derivatives, the reader is referred to Schou (1992).

Since we fit for one n and ℓ at a time while holding the leaks fixed, the peakbagging must be iterated to account for the variation of the mode parameters of the leaks as the fits proceed. For all iterations except the last, we fit six a -coefficients. In the original analysis, the initial guess for the first iteration was taken from the final fits of the previous timeseries. In the new analysis, the same initial guess was used for all time periods, which allows for fitting all of them independently of one another. We found this made no significant difference. Any modes that cannot be fit in the first attempt have the initial guess of their background parameter $[b]$ perturbed by -1 and the fit is reattempted. At this point in the original analysis the resulting set of fitted modes would be weeded by hand to reject outliers. In the new analysis this step is simply skipped; again we found it made no significant difference. In both cases the remaining modes are used to make new initial guesses for the modes that had not converged (or were rejected). The second iteration is then done in the same way as the first. At no point do we ever attempt to fit modes for which there are estimated to be other modes within ± 2 in ℓ and within twice the line width in frequency. These typically occur at the ends of ridges and do not converge in any case.

For subsequent iterations, the modes that have not converged to within $0.1 \sigma_{\nu_0}$ or for which there exist unconverged modes with the same n and $\Delta\ell = \pm 1$ are fitted (occasionally more modes would be fit in the original analysis). In the original analysis the convergence of the modes would be examined to determine the total number of iterations, which would usually be from 9 to 11. All modes would be fit in the last iteration and in at least one of the preceding two iterations. In the new analysis, for the sake of automation, the peakbagging would always be performed for ten iterations with all modes being fit during the last three. In both cases, the final fits are repeated with both 18 and 36 a -coefficients, which is to say that these fits are not iterated.

After the final iteration, the resulting set of modes is automatically weeded one last time. For the fits with six a -coefficients, modes differing by more than $0.25 \sigma_{\nu_0}$ from their input guesses are rejected. Additionally, any mode with a large error on its frequency given its width is suspect: if there were no background noise, we would expect a frequency error given by

$$(2\ell + 1)\sigma_{\nu_0}^2 = \frac{w}{4\pi T} \quad (3.16)$$

where T is the length of the timeseries (Libbrecht, 1992). Any mode with a frequency error greater than 6.0 times this prediction is rejected. The same theoretical error estimate is the motivation for identifying modes for which the line width is smaller than the width of a frequency bin. These modes have the error estimates on their frequencies and a -coefficients increased by a factor of $\sqrt{1/(wT)}$. This prevents underestimates of the error caused by low estimates of the widths in the region where they cannot be reliably estimated.

The resulting set of mode parameters is then compared to those of a model obtained from a rotational inversion of fits to a 360-day long timeseries at the beginning of the mission. The median difference between the fit and the model of the odd a -coefficients is taken for the f -modes to account for their change throughout the solar cycle. The differences for all of the modes are compared to this median; any that differ by more than 10σ are rejected.

To weed the fits with 18 and 36 a -coefficients, their error estimates are adjusted as above. Frequencies and a -coefficients are then compared to the fits using six a -coefficients. Any mode for which the error estimates on any of these parameters increased by more than a factor of 2.0, or for which any of these parameters changed by more than 2σ (estimated from the fits with 18 and 36 a -coefficients, respectively), is rejected. Any mode that was rejected in the fits with six a -coefficients is also removed from the fits with 18 a -coefficients, and any mode that was rejected in the fits with 18 a -coefficients is also removed from the fits with 36 a -coefficients.

Leakage Matrix

For this work, the leakage matrix elements, which quantify how modes nearby in spherical harmonic space appear in the spectrum of the target mode, are computed by generating artificial images containing components of the solution to the oscillation equations projected onto the line of sight for a subset of the modes that we wish to fit. A mode on the Sun has a velocity at the surface with components proportional

to the real parts of ³

$$\begin{aligned}
u_r &= Y_\ell^m(\phi, \theta) = P_\ell^m(x)e^{im\phi} \\
u_\theta &= \frac{1}{L} \frac{\partial Y_\ell^m}{\partial \theta} = -\frac{1}{L} \frac{dP_\ell^m}{dx} e^{im\phi} \sin \theta \\
u_\phi &= \frac{1}{L} \frac{1}{\sin \theta} \frac{\partial Y_\ell^m}{\partial \phi} = \frac{1}{L} \frac{im}{\sin \theta} P_\ell^m(x) e^{im\phi}
\end{aligned} \tag{3.17}$$

where $x = \cos \theta$ and $L = \sqrt{\ell(\ell + 1)}$. A mode with oscillation amplitude $V_{\ell m}$ will then have a total velocity of

$$\mathbf{V} = \mathbf{V}_{\ell m}^r + c_t \mathbf{V}_{\ell m}^h \tag{3.18}$$

where $\mathbf{V}_{\ell m}^r = V_{\ell m} u_r \hat{r}$, $\mathbf{V}_{\ell m}^h = V_{\ell m} (u_\theta \hat{\theta} + u_\phi \hat{\phi})$, and

$$c_t = \frac{\nu_0^2(0, \ell)}{\nu_0^2(n, \ell)} \tag{3.19}$$

is the ratio of the mean multiplet frequency of the f -mode squared to the mean multiplet frequency of the given mode squared at that ℓ (Rhodes *et al.*, 2001). Therefore $c_t = 1$ for the f -mode and $c_t < 1$ for the p -modes. Equation 3.19 is derived under the assumption of zero lagrangian pressure perturbation at the solar surface.

Since the spherical harmonic decomposition does not separate the different radial orders, we create a separate matrix for the vertical and horizontal components; the effective leakage matrix will be computed during the fitting by combining them according to Equation 3.18. We project each component onto the line of sight separately using projection factors calculated for a finite observer distance. In the approximation of an infinite observer distance this would become

$$\begin{aligned}
u_{\text{vertical}} &= V_{\ell m} P_\ell^m(x) e^{im\phi} \sin \theta \cos \phi \\
u_{\text{horizontal}} &= -\frac{V_{\ell m}}{L} \left(\frac{dP_\ell^m}{dx} \sin \theta \cos \theta \cos \phi + \frac{im}{\sin \theta} P_\ell^m(x) \sin \phi \right) e^{im\phi}
\end{aligned} \tag{3.20}$$

where we choose $V_{\ell m} = 1000 \text{ ms}^{-1}$ to give us roughly the same order of magnitude as the observations. As with the real data, these images are only calculated for $m \geq 0$. The resulting leakage matrix will be divided by 1000.

³The sign of u_r relative to u_θ and u_ϕ depends on the convention for the sign of m .

These images are first generated as they would appear to MDI, assuming an observer distance of 1 AU, a P_{eff} and B_0 both equal to zero, and that the image is centered on the CCD. They are then convolved with a gaussian in each dimension with the same width of $\sigma = 4/\sqrt{2}$ as used onboard the spacecraft, but they are not sub-sampled at this point. Rather they are also convolved with a function that takes into account the interpolation errors made during the subsequent remapping. This function is generated by applying the cubic convolution algorithm to a δ -function. During the spherical harmonic decomposition, these images will be remapped to the same resolution in longitude and $\sin(\text{latitude})$ as the real data. The higher resolution images are used to simulate an average over different pixel offsets; we have verified the accuracy of this technique by generating lower resolution images and actually performing the average. After the remap, the artificial data are processed exactly as the real data. For each image, we take its scalar product with a set of target spherical harmonics in the range $\Delta\ell = \pm 6$ given above. The results are the coefficients c^{RR} and c^{II} given in Equation 3.9. The values for the modes that we did not compute directly are found by interpolation. The values for negative m are given by Equations 3.10.

In the original analysis, only the vertical component of the leakage matrix was used, meaning that the horizontal component was assumed to be zero. Although this is not a bad approximation for high-order p -modes, it becomes worse as one approaches the f -mode ridge, where the horizontal and vertical components have equal magnitude. In the new analysis, our first improvement to the peakbagging is to include both components.

For a spherically symmetric Sun, the horizontal eigenfunctions would be spherical harmonics. Although the presence of differential rotation breaks this symmetry, the true eigenfunctions can still be expressed as a sum over spherical harmonics. In the new analysis, this is accounted for in the peakbagging by appropriately summing the leakage matrix. We use the prescription given by Woodard (1989) with the differential rotation expanded as

$$\Omega(x) = B_0 + B_1x^2 + B_2x^4 \quad (3.21)$$

where, again, $x = \cos\theta = \sin(\text{latitude})$. We first used constants derived from surface

measurements, with values of $B_1 = -75$ nHz and $B_2 = -50$ nHz as given by Woodard (the value of B_0 is not used). However, this has the drawback of distorting every mode in the same way, even though they sample different depths where the differential rotation has a different dependence on latitude. Following Vorontsov (2007), we use the estimated splitting coefficients to calculate B_1 and B_2 for each mode separately. In particular, we use the approximation that

$$\begin{aligned} B_1 &= -5a_3 - 14a_5 \\ B_2 &= 21a_5 \end{aligned} \tag{3.22}$$

so that B_1 and B_2 change as the iteration proceeds. Fortunately this did not disrupt the convergence of the a -coefficients. This change made only a modest difference in the mode parameters, as discussed below.

Asymmetry

In addition to the symmetric line profiles described by Equation 3.5, we have also used asymmetric profiles to fit the data. Although it is common to use the profile derived by Nigam and Kosovichev (1998), their equation has the undesirable properties that it is based on an approximation that does not hold far from the mode frequencies and that its integral over all frequencies is infinite. To derive a more well behaved profile, we begin with Equation 3 of Nigam and Kosovichev (1998), which was derived for a one-dimensional rectangular potential well model, and generalize it by replacing their βX with an arbitrary function of frequency $h(\nu)$. Since β is generally very small, we drop the second term in the numerator to arrive at a variance given by

$$v(\nu) = \frac{P_D(\nu) \cos^2[h(\nu) + \gamma(\nu)]}{g(\nu) + \sin^2[h(\nu)]} \tag{3.23}$$

where P_D is the power spectrum of the excitation, γ is a measure of the asymmetry, and g is related to the damping. The function h is constrained to be $n\pi$ at the mode frequencies, and in the numerator we have changed sin to cos so that $\gamma = 0$ corresponds to a symmetric profile. Considering a single ℓ and m , we can expand

Equation 3.23 in terms of profiles given by Equation 3.5 to get

$$v_{\ell m}(\nu) = \cos^2[h_{\ell m}(\nu) + \gamma_{\ell m}(\nu)] \sum_n \frac{1}{\cos^2[\gamma_{\ell m}(\nu_{n\ell m})]} \frac{2wA^2}{w^2 + 4(\nu - \nu_{n\ell m})^2} \quad (3.24)$$

where the factor $1/\cos^2(\gamma_{\ell m}(\nu_{n\ell m}))$ has been included so that to lowest order, A retains its original meaning. To find a function to use for h , we note that from the Duvall law (Duvall, 1982) we can define $h_0(\nu) = \nu F(\nu/(\ell+1/2)) - \pi\alpha(\nu) \approx n\pi$, where F and α are known functions. These we have tabulated from a fit to a 360-day long timeseries at the beginning of the mission, and interpolate them as needed during the peakbagging. We then choose $h = h_0 + h_1$ where h_1 is a piecewise linear function chosen to make h exactly $n\pi$ at the mode frequencies as required. The function γ can likewise be interpolated using a piecewise linear function derived from its value at the mode frequencies. Above the frequency of the maximum n and below the frequency of the minimum n , we assign constant values to h_1 and γ .

Equation 3.24 is valid for all frequencies. Restricting ourselves to a single mode, we can now replace the variance in Equation 3.12 with

$$v_{n\ell m}(\mathbf{p}, \nu) = \frac{\cos^2[h_{\ell}(\nu') + \gamma_{\ell}(\nu')]}{\cos^2(\gamma_{n\ell})} \frac{2w_{n\ell}A_{n\ell}^2}{w_{n\ell}^2 + 4(\nu - \nu_{n\ell m})^2} \quad (3.25)$$

where $\nu' = \nu - \nu_{n\ell m} + \nu_0(n, \ell)$, $\nu_{n\ell m}$ is given by Equation 3.8, and we have implicitly assumed that the asymmetry is the same for all m . The function γ_{ℓ} is constructed from the values $\gamma_{n\ell}$, the fit parameters, such that $\gamma_{\ell}(\nu_0(n, \ell)) = \gamma_{n\ell}$. Since h is an increasing function of frequency, a positive value of $\gamma_{n\ell}$ means that the high-frequency wing of the line will be lower than the low-frequency wing. Finally, the value actually reported is $\tan(\gamma_{n\ell})$.

To form the initial guess for the asymmetric fits, we examined the frequencies and asymmetry parameters resulting from a preliminary fit using the same initial guess as for the symmetric fits. We then fit the frequency shift relative to the symmetric case by fitting a sixth-order polynomial in frequency, which we now add to the initial guess for the frequency. For the asymmetry parameter, we use a third-degree polynomial in frequency directly for the initial guess.

When we tried the iteration scheme described above for the 15 intervals that we

analyzed in detail, we found that for some of them very few f -modes were fitted. We therefore added an automatic rejection of fits with negative asymmetry parameters in the range $\nu < 2000 \mu\text{Hz}$ between iterations of the peakbagging, since the asymmetry in that range is observed to be positive. This solved the problem for these 15 intervals, but when we reanalyzed the entire mission, a small number of intervals still had few f -modes fit. We were able to improve the coverage of those intervals by adding a further criterion to reject modes that had an extremely high value of $\tan(\gamma)$, but this caused other intervals to lose modes. We therefore reverted to the initial rejection criteria. Clearly, the asymmetric fits are much less stable than those using symmetric profiles.

3.4 Results

3.4.1 Mode Parameters

We applied 11 different analyses to 15 intervals of 72 days each, beginning in January 2004 (see Table 3.2). Comparing the analyses is complicated by the fact that, in general, they do not result in identical modesets. For each analysis, we therefore only consider modes common with the preceding analysis for each interval. We then took an average in time over whatever intervals had each mode successfully fit. In so doing, we are assuming that the difference in mode parameters resulting from the difference in the analysis is much more significant than their relative change over time. In the following figures, we plot the difference in several mode parameters normalized by their error estimates. For these plots, we calculated the average error estimates, rather than the error on the average, and for any given comparison between two analyses, we use the larger error estimate of the two. Thus the significance that we have plotted is the least that one might expect from a single 72-day fit. The range of some plots excludes a few outliers; this is always less than 1.4% of the data. The sense of subtraction is the later analysis minus the earlier one. Here we have plotted all of the parameter differences as a function of frequency. Full listings of all mode parameters for all time intervals and all analyses that we performed are provided as

ASCII tables in the electronic supplementary material.

As can be seen in Figure 3.4, the change in frequency was most significant for the image-scale correction and asymmetric fits. Including the horizontal displacement and correcting for distortion of eigenfunctions made the next most significant changes, followed by correcting for cubic distortion, in agreement with our previous work (Larson and Schou, 2008). Differences in detail between these and our previous results can mostly be attributed to the different method that we have used for computing mode averages; by first taking the common modeset for each 72 day interval, the calculation of the averages becomes much more straightforward. For the image-scale correction, some of the difference in magnitude of the change in mode frequency can be attributed to the different epoch we reanalyzed. Previously we studied the two years beginning in January 2003, whereas in this work we study the three years beginning in January 2004, and the image-scale error is the only problem with the original analysis that is known to become worse over time. For the asymmetric fits, we used an improved iteration scheme for the asymmetry parameter, which seems to have resulted in a smaller change in frequency. The correction for CCD misalignment made a significant difference for the f -mode, but otherwise this correction, the correction for the inclination error, the correction for CCD tilt, improved detrending, and improved gapfilling typically resulted in less than 0.5σ change in the mode frequencies. We have also used a different method for calculating the Woodard effect, as described above, but we found this made less than a 0.5σ difference in all of the parameters for the vast majority of modes. Therefore in all plots we show only the results of using the second method.

We find similar results for the amplitude and width (Figures 3.5 and 3.6), although for both of these parameters the detrending and gapfilling made much more significant differences. This is likely because these two changes in the processing made the dominant changes to the background parameter (Figure 3.7), as one might expect. We also point out that the large scatter of all three of these parameters just above 3.5 mHz indicates an instability of the fits in this frequency range, which may perhaps relate to the bump as well.

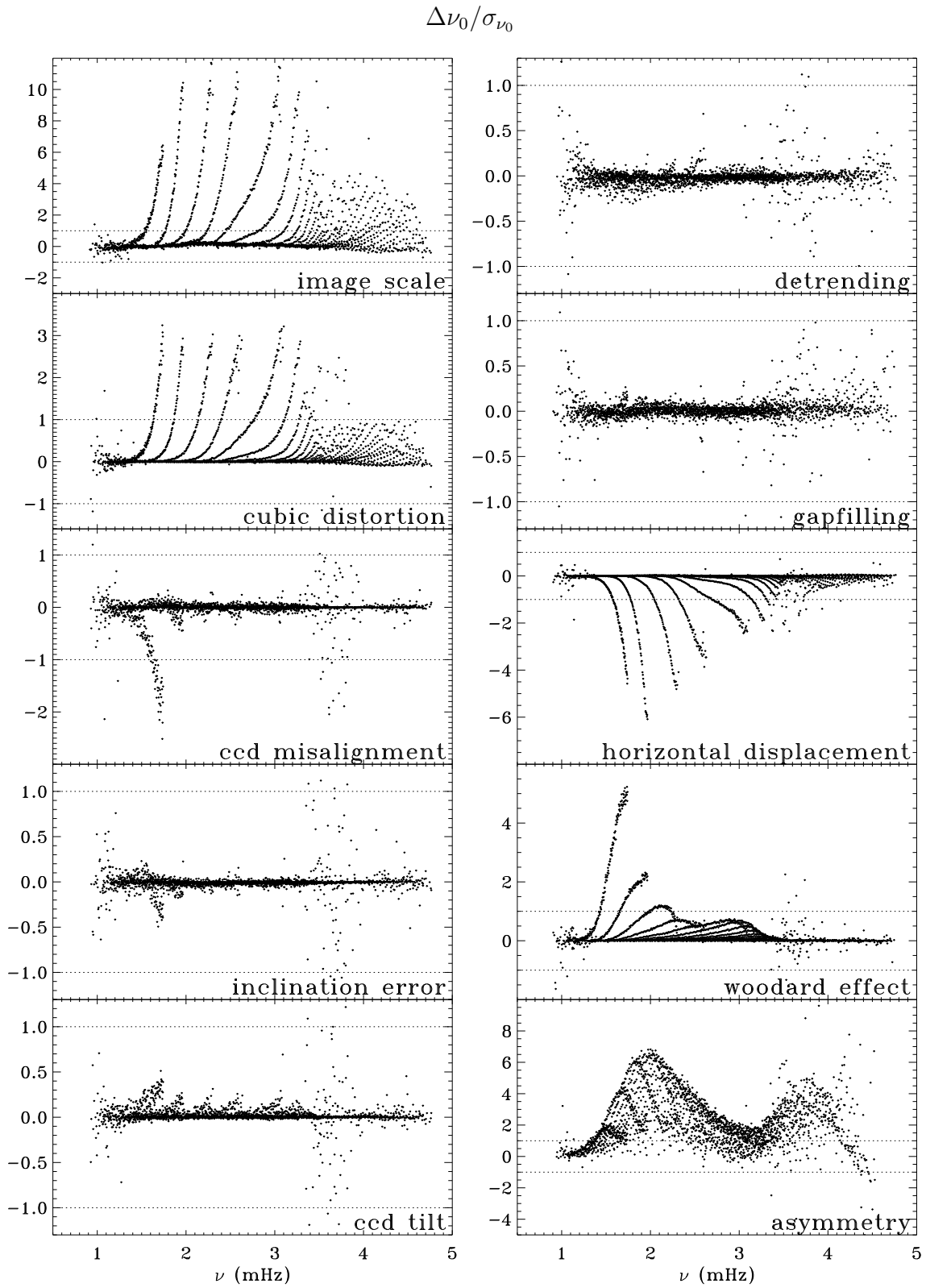


Figure 3.4: Change in mean multiplet frequency resulting from each change as a function of frequency, in units of standard deviation. Each panel is scaled differently; dotted lines show the $\pm 1\sigma$ levels.

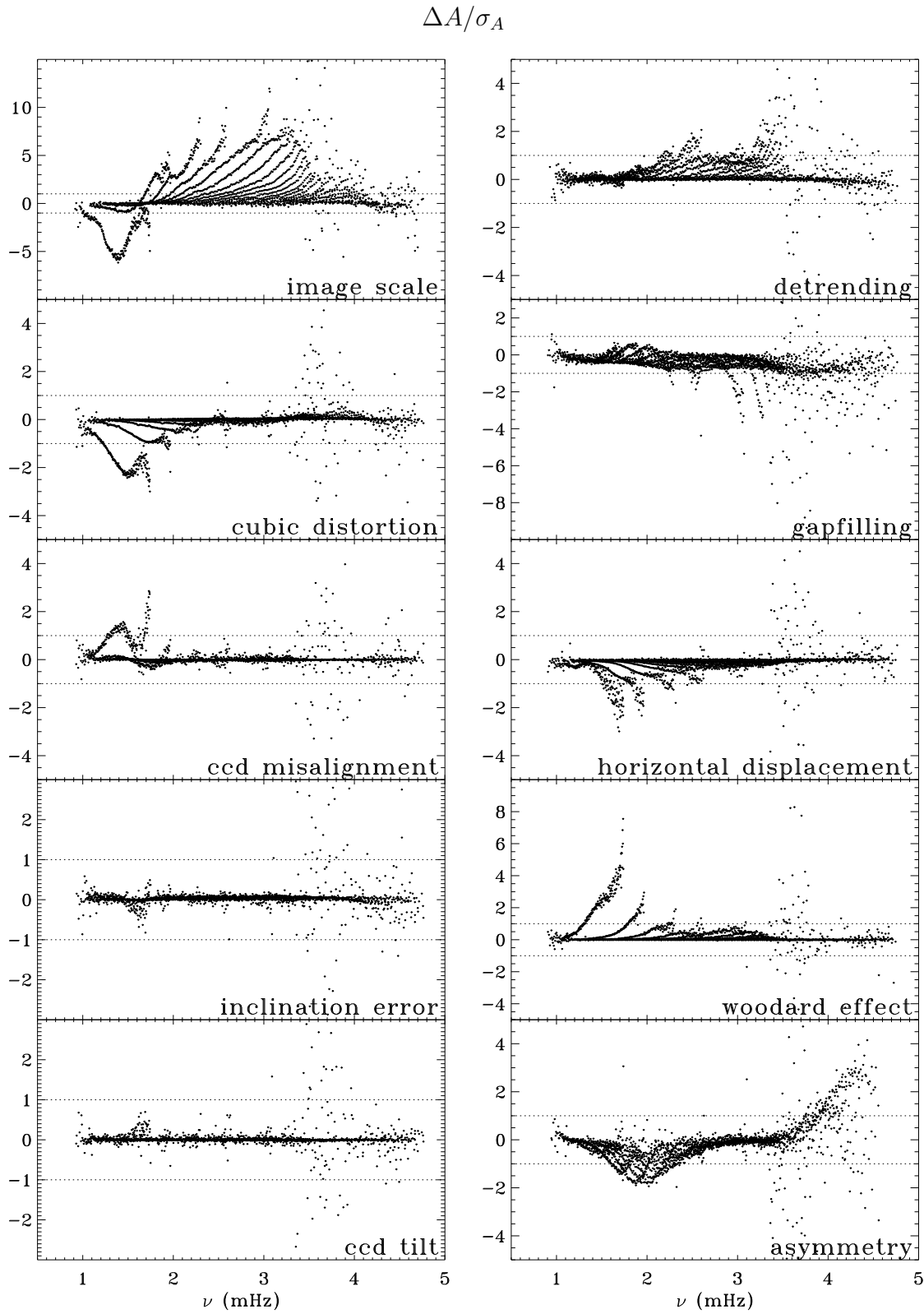


Figure 3.5: Change in amplitude resulting from each change as a function of frequency, in units of standard deviation. Each panel is scaled differently; dotted lines show the $\pm 1\sigma$ levels.

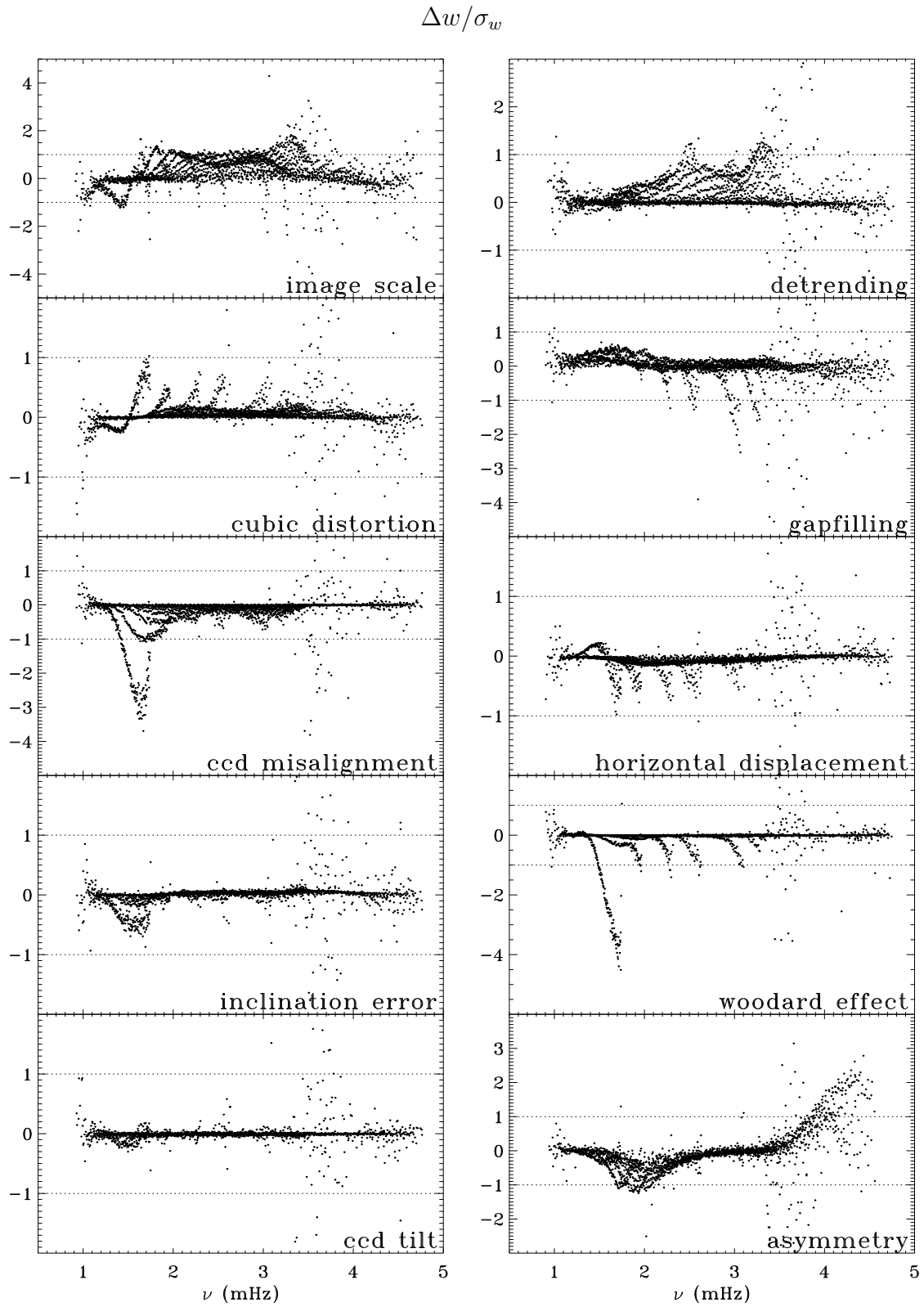


Figure 3.6: Change in width resulting from each change as a function of frequency, in units of standard deviation. Each panel is scaled differently; dotted lines show the $\pm 1\sigma$ levels.

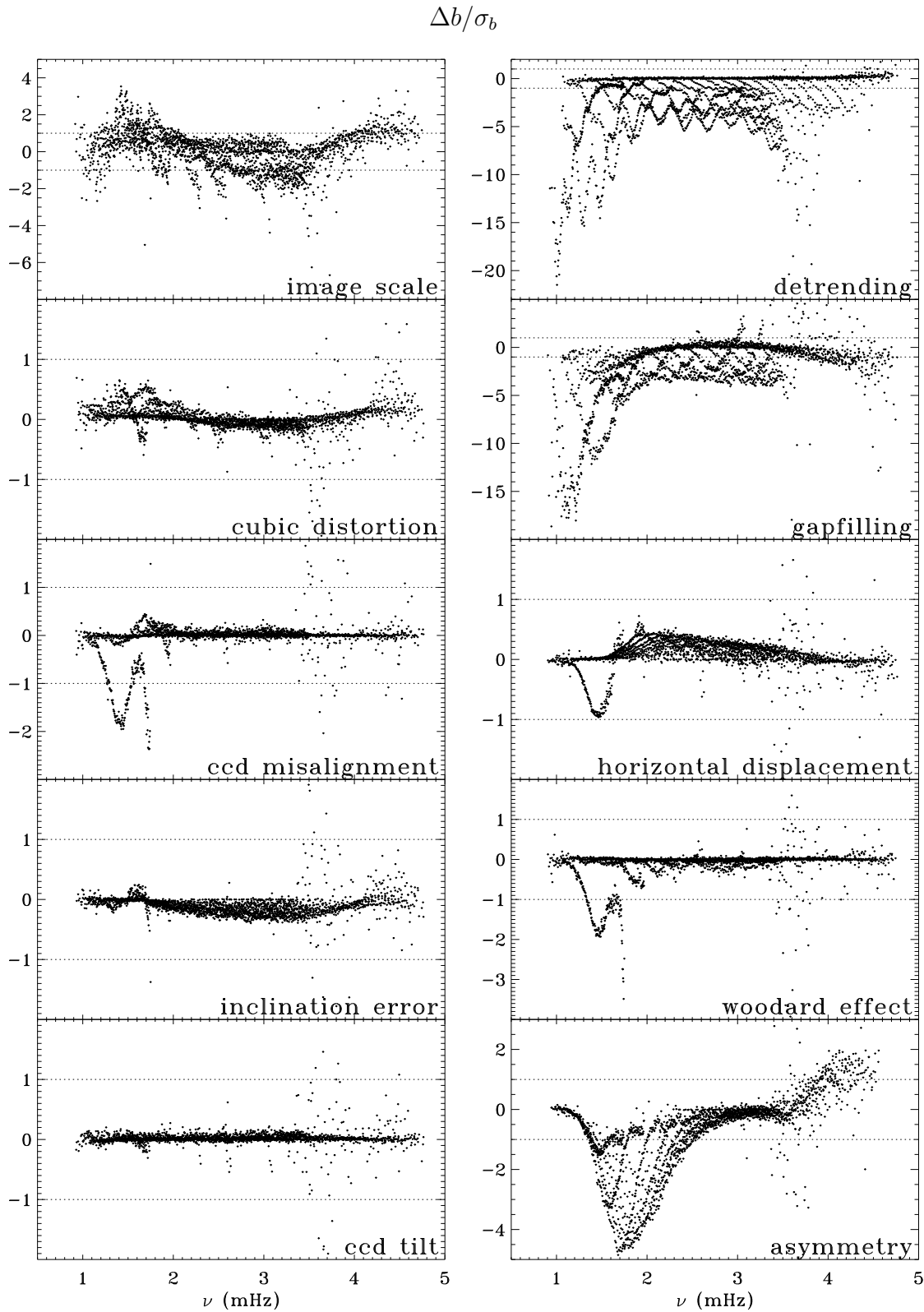


Figure 3.7: Change in background parameter resulting from each change as a function of frequency, in units of standard deviation. Each panel is scaled differently; dotted lines show the $\pm 1\sigma$ levels.

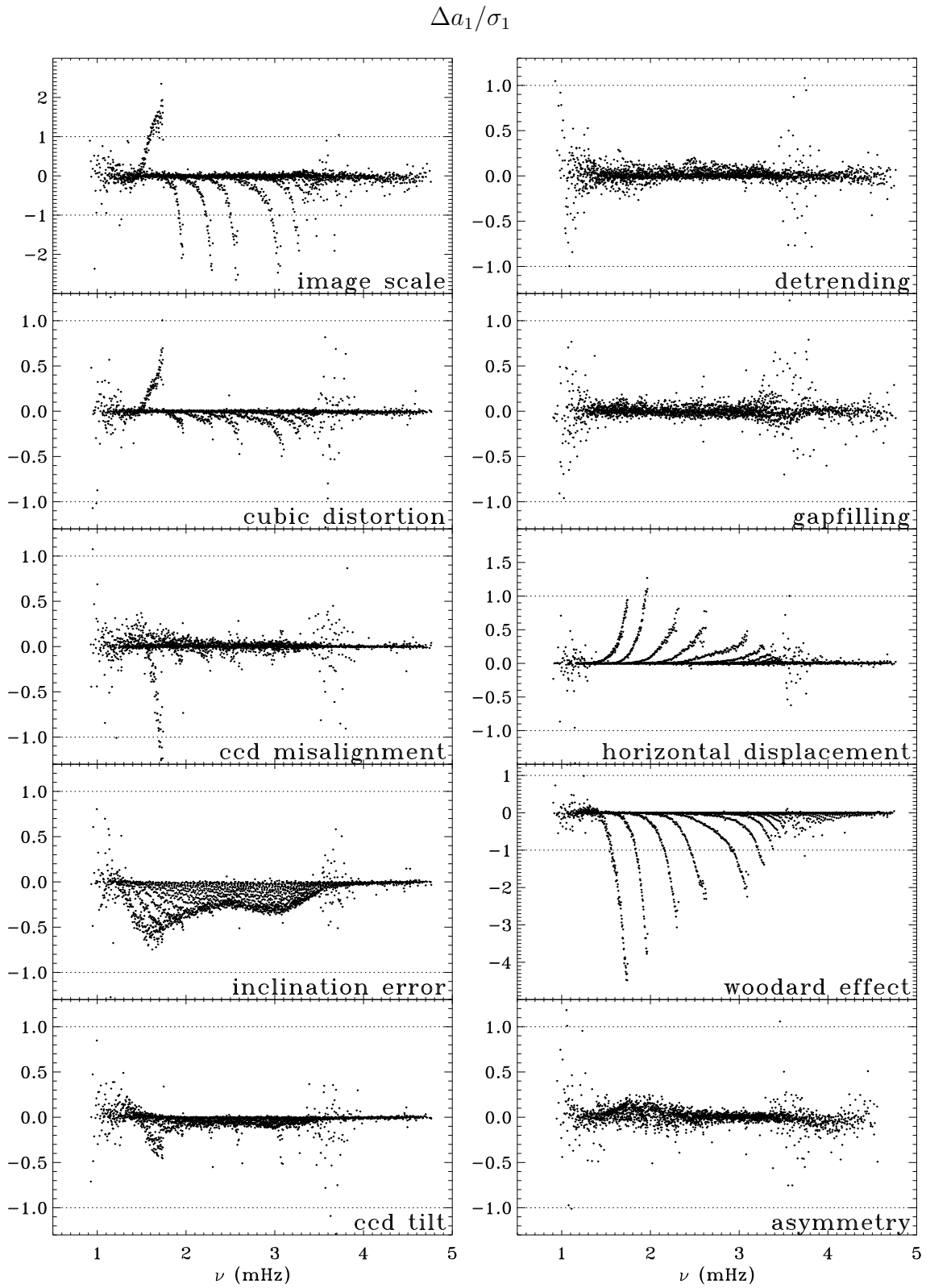


Figure 3.8: Change in a_1 resulting from each change as a function of frequency, in units of standard deviation. Each panel is scaled differently; dotted lines show the $\pm 1\sigma$ levels.

The changes in a_1 (Figure 3.8) have relative magnitudes that are roughly similar to the changes in frequency, the most notable exception being that correcting for the Woodard effect caused the dominant changes to this parameter. For the f -mode, correcting for the image scale, cubic distortion, and misalignment of the CCD resulted in changes with the same sign as the frequency changes, but for the p -modes, and all modes when correcting for horizontal displacement and the Woodard effect, the changes had opposite sign. The changes in a_1 resulting from the inclination correction were more significant than the frequency changes, and show an interesting frequency dependence not seen in other parameters for this correction. The effects of the various changes on inversions of a_1 are discussed in the next section.

To see the effect of all of the changes in the processing taken together, we examine the mission averages, formed as described above. Figure 3.9 shows the result for various mode parameters. For the p -modes, the error estimates were mostly unaffected. However, the set of all improvements up to and including the correction for the Woodard effect resulted in substantially lower error estimates for the f -modes, as shown in Figure 3.10. Unfortunately, using asymmetric line profiles resulted in substantially higher error estimates for the mode frequencies and background parameters, as shown in Figure 3.11.

One easy check of the robustness of our results is to compare the 72-day and 360-day analyses. Even without examining any mode parameters, one can see that the 360-day analysis was more successful in the sense that it was able to fit more modes, as shown in Figure 3.12. To compare the mode parameters, for each 360-day interval we averaged the results of the five corresponding 72-day analyses (three for the third 360-day interval) for the modes that were present in all of them. The errors used are the errors on the average. Then we formed modesets common between the 360-day and 72-day analyses as above, representing the mission averages, this time taking the average error. The differences in mode parameters using asymmetric line profiles are shown in Figure 3.13 and the corresponding error ratios are shown in Figure 3.14. The results were mostly similar using symmetric line profiles. To compare the background parameters, we subtracted $\log(5)$ from the 360-day fits.

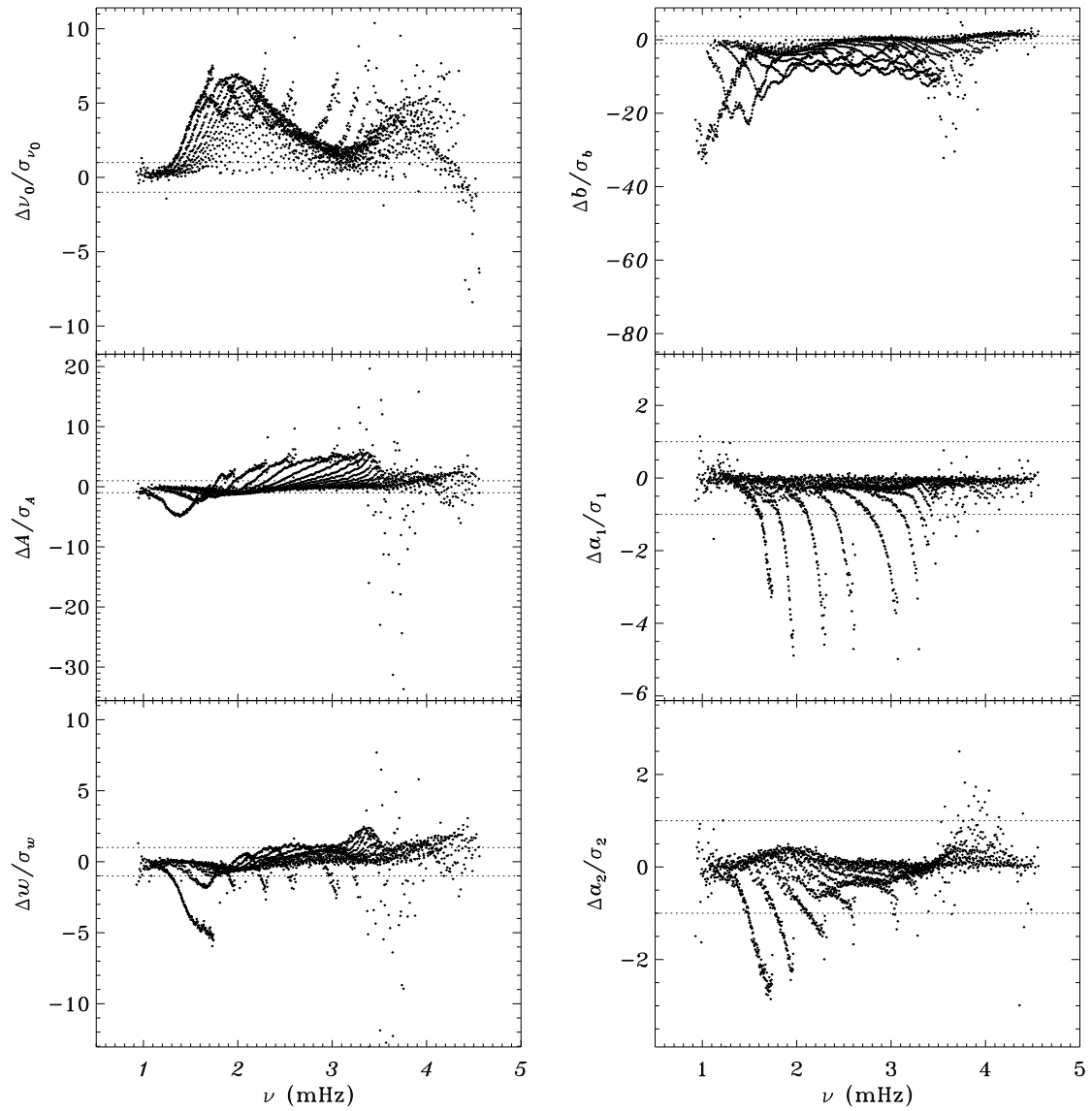


Figure 3.9: Change in frequency, amplitude, width, background parameter, a_1 , and a_2 resulting from all changes as a function of frequency, in units of standard deviation, averaged over the entire mission. Dotted lines show the $\pm 1\sigma$ levels. The range of these plots includes all points.

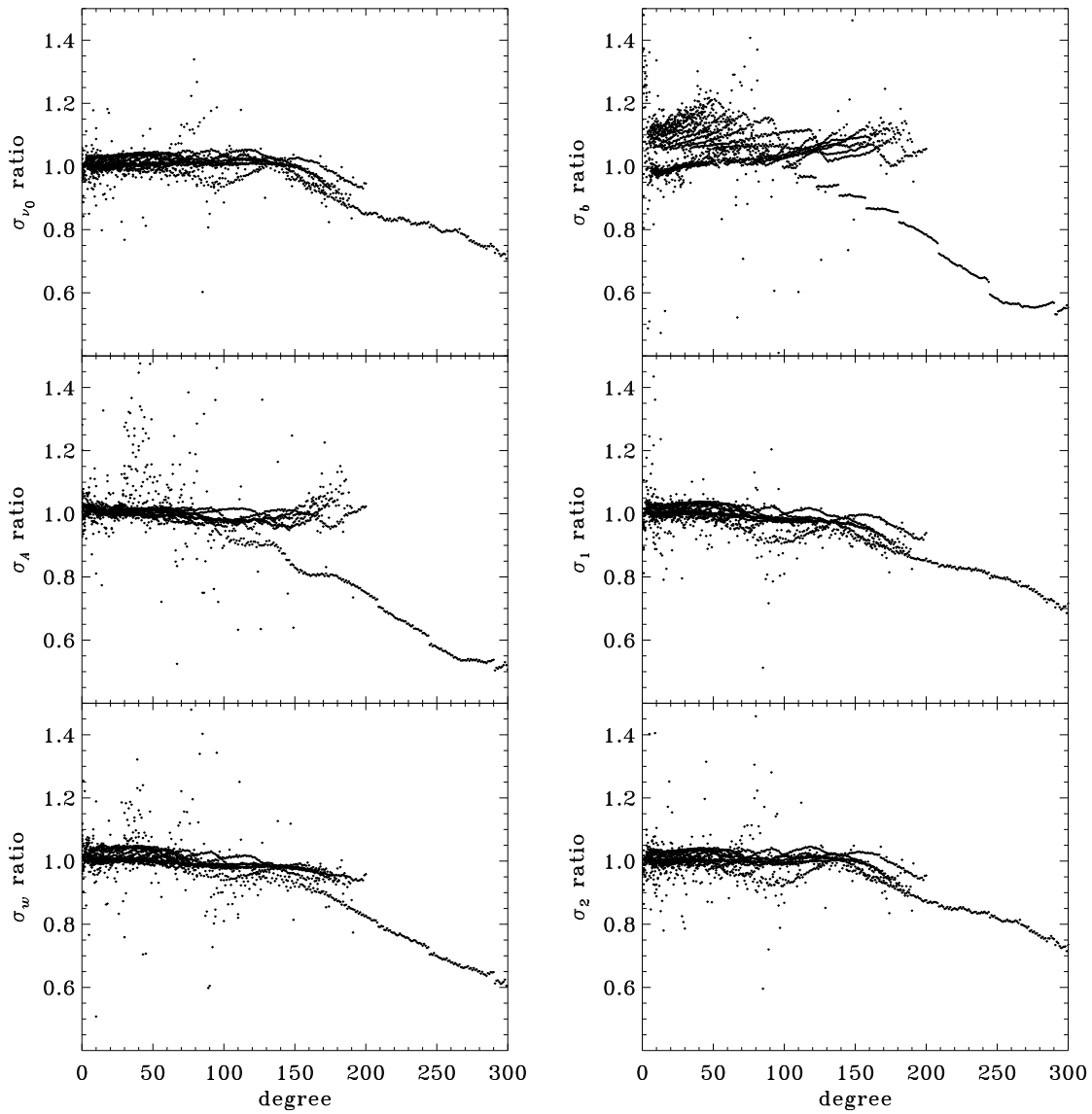


Figure 3.10: Ratio of the improved error estimates to the original error estimates as a function of spherical harmonic degree for the parameters shown in Figure 3.9. The improved estimates do not include fitting asymmetric profiles. For the background, 2.1% of points do not fall within the range shown on the plots. For the other parameters, at most 0.6% of points are not shown.

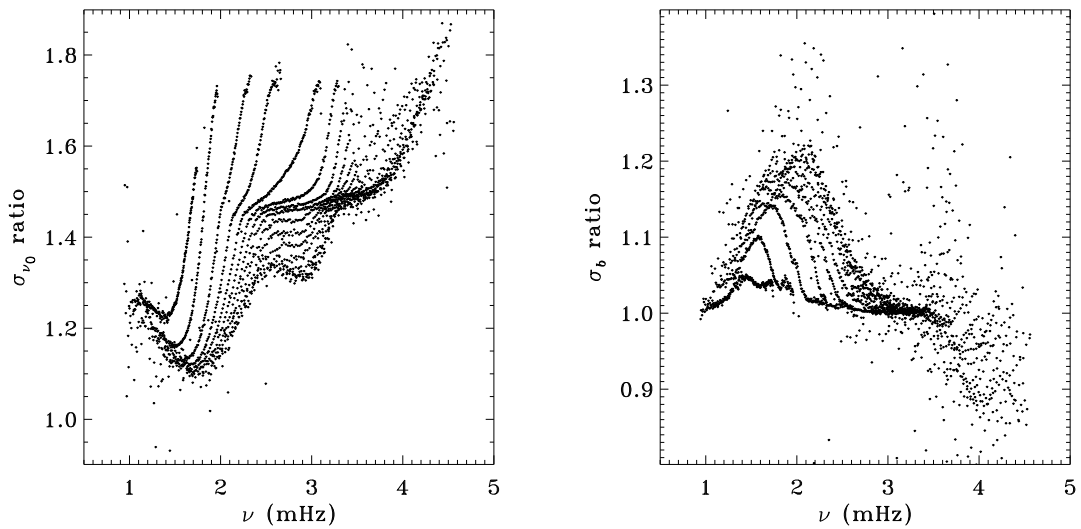


Figure 3.11: Amplification of errors for frequency and background resulting from the use of asymmetric profiles. For the background, 2.9% of points are excluded; for the frequency, 0.3% are excluded.

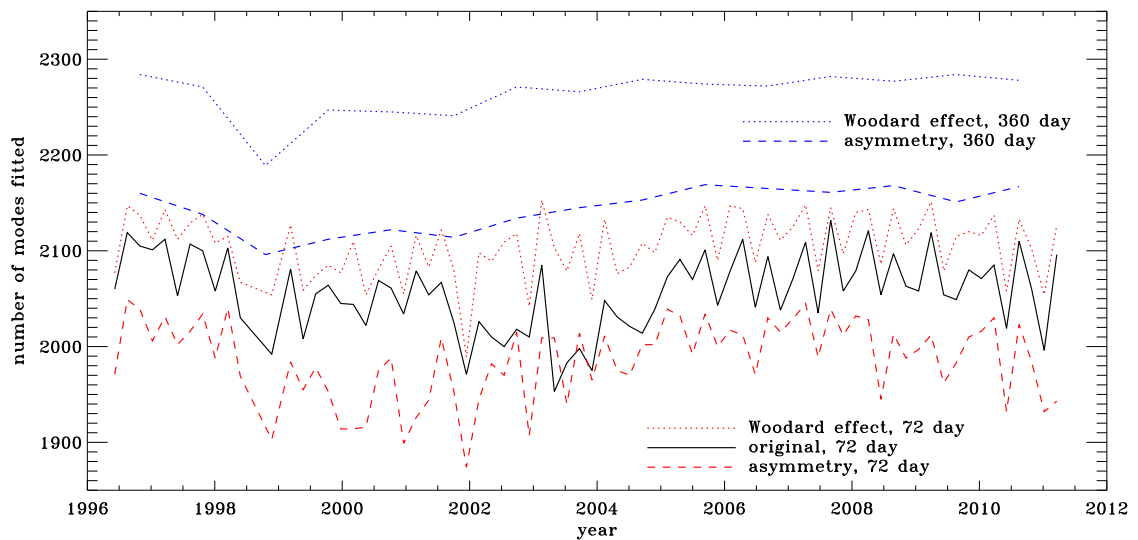


Figure 3.12: Number of modes fitted as a function of time for the five different ways we analyzed the entire mission. Dotted lines show the set of all changes in the processing up to correcting for the Woodard effect; dashed lines show the result of also using asymmetric line profiles. In both cases the higher line is for the 360-day fits, the lower line is for the 72-day fits. The solid line shows the original analysis.

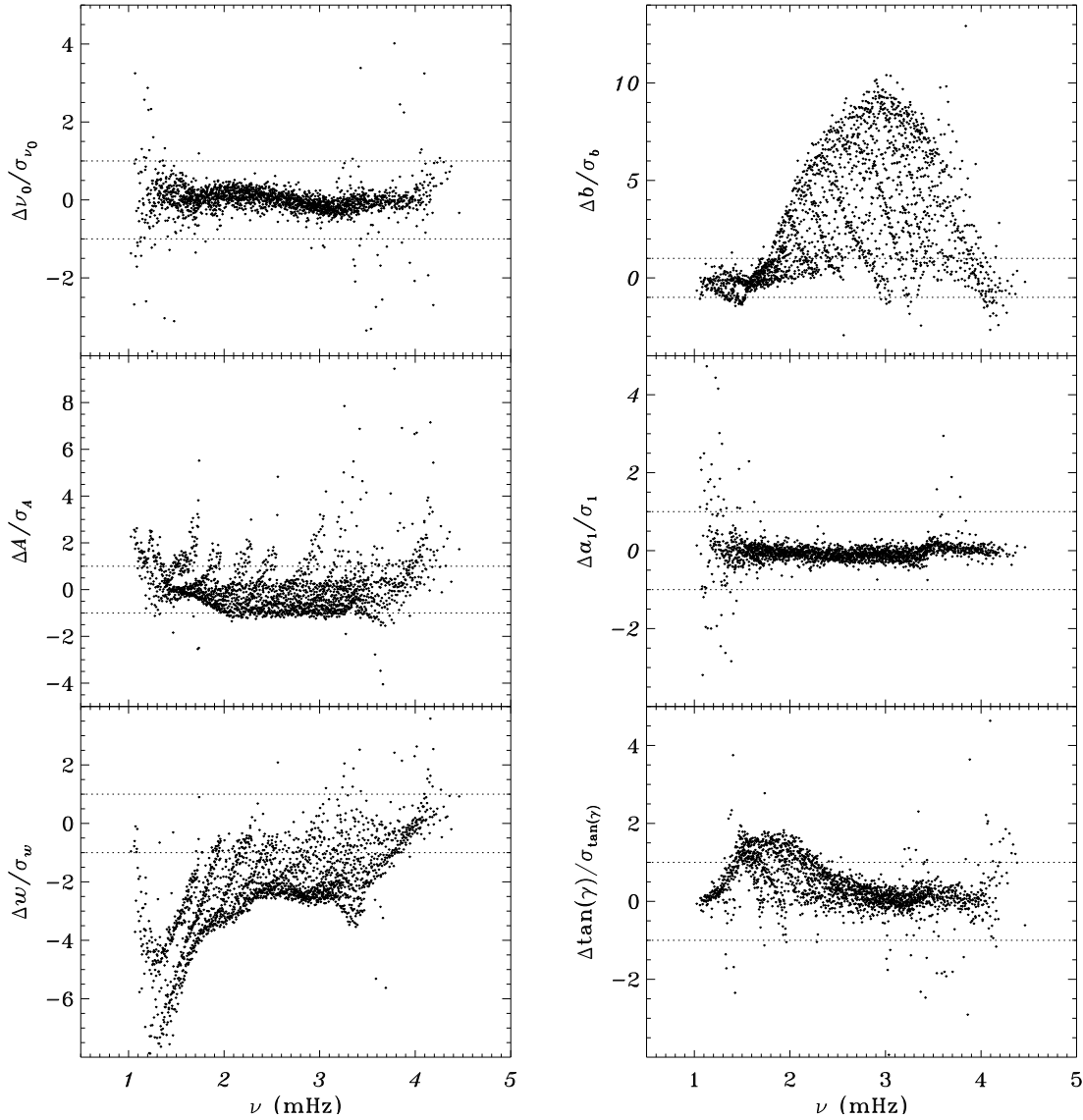


Figure 3.13: Difference in frequency, amplitude, width, background parameter, a_1 , and asymmetry parameter between 360-day fits and an average of 72-day fits as a function of frequency, in units of standard deviation from the 360-day fits. Dotted lines show the $\pm 1\sigma$ levels. The sense of subtraction is 360 day minus 72 day. At most 0.9% of points have been excluded.

Although the change in frequency seems to show a weak systematic dependence on frequency, the changes are mostly not significant. The change in frequency was slightly more significant using symmetric line profiles, especially at low frequencies.

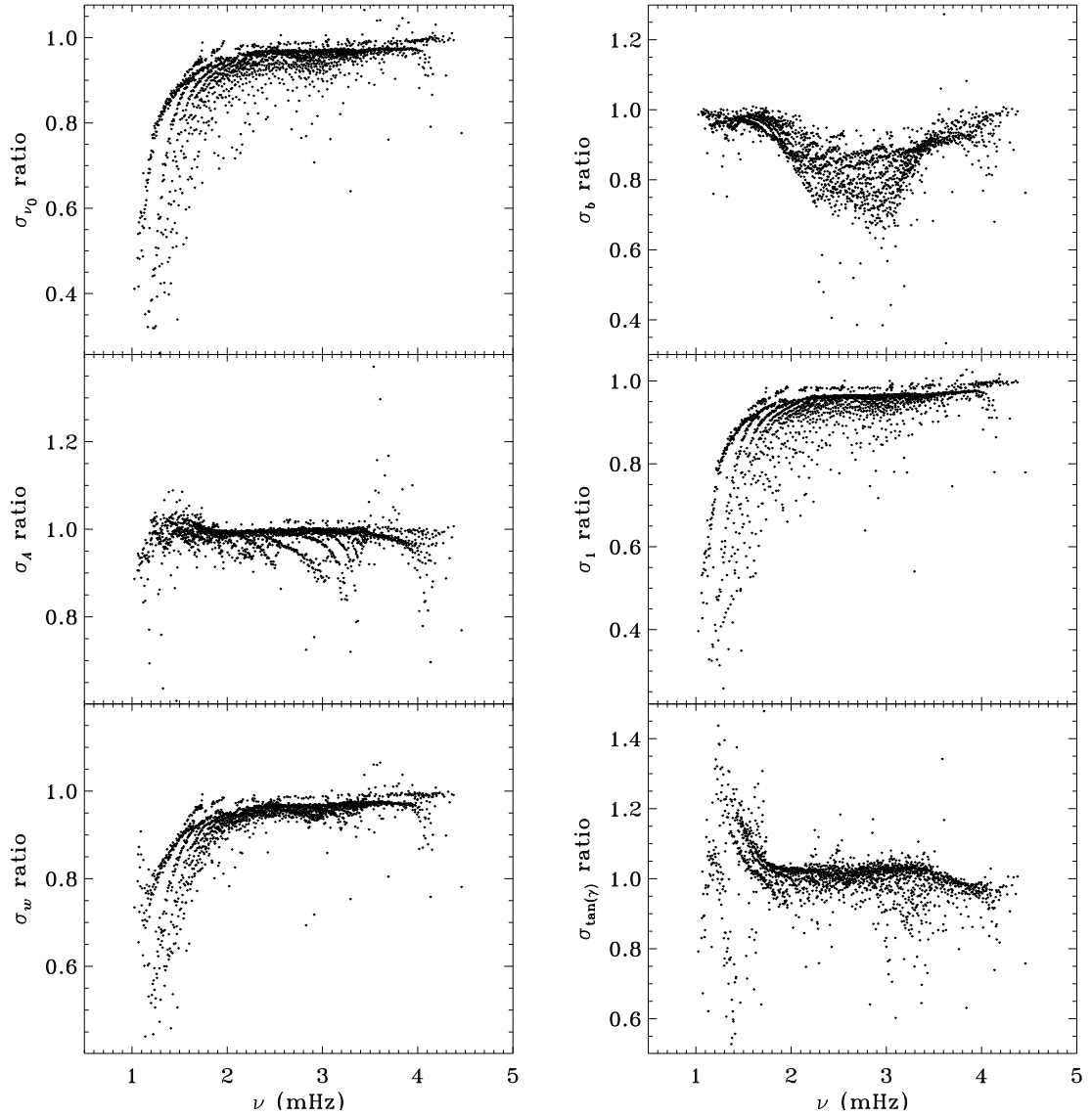


Figure 3.14: Ratio of the errors estimated from 360-day fits to the errors estimated from an average of 72-day fits as a function of frequency for the parameters shown in Figure 3.13. At most 1.9% of points have been excluded.

The changes in amplitude show ridge structure; although the majority of modes show reduced amplitude, the mean change is actually positive. The changes in width show ridges as well, but here the width is almost always less for the 360-day fits, and more

so at lower frequencies. This is as one might expect, since the lorentzian is not well-resolved when the width is on the order of the width of a frequency bin. The increased frequency resolution of the 360-day fits better characterizes these low widths. The background parameter shows the most significant changes (an increase except for the f -mode), but centered on the p -mode band, where the noise is drowned by the signal. The changes in a_1 are the flattest, although a feature is discernible around 3.5 mHz. The asymmetry parameter was in general greater for the 360-day fits, with a peak around 1.8 mHz. For the frequency, width, and a_1 , the estimated errors were much lower for the 360-day fits at low frequencies, again as one might expect. Harder to understand is why the error on the asymmetry parameter increased in the same frequency range. The background parameter also had lower errors, but again in the center of the frequency range.

3.4.2 Systematic Errors

In this section we will refer to the changes in processing by the order in which they were applied. This is summarized in Table 3.2.

Table 3.2: Sequence of changes made to the analysis; each analysis includes the changes made in all previous ones.

0	original analysis
1	image scale
2	cubic distortion
3	CCD misalignment
4	inclination error
5	CCD tilt
6	window functions and detrending
7	gapfilling
8	horizontal displacement
9	distortion of eigenfunctions (“Woodard effect”)
10	asymmetric line profiles

To see the effect of the various changes on our systematic errors, we begin by performing simple one-dimensional regularized least-squares rotational inversions of the a_1 -coefficient only. An RLS inversion seeks to minimize the sum of normalized

residuals squared plus a penalty term that serves to constrain rapid variations in the solution. In particular, we have chosen to minimize

$$\sum_{n\ell} \left[\frac{1}{\sigma_1(n, \ell)} \left(\int_0^1 K_{n\ell}(r) \bar{\Omega}(r) dr - a_1(n, \ell) \right) \right]^2 + \mu \int_0^1 \left(\frac{d^2 \bar{\Omega}}{dr^2} \right)^2 dr \quad (3.26)$$

where $\bar{\Omega}$ is the inferred rotation rate, the $K_{n\ell}$ are known kernels calculated from the mode eigenfunctions that relate the rotation rate to a_1 , σ_1 is the standard error on a_1 , r is fractional radius, and μ is the tradeoff parameter that controls the relative importance of the two terms. A low value of μ will fit the data better, but the solution may oscillate wildly as a function of radius. A higher value of μ will attenuate this feature (the solution will be more regularized) at the cost of increased residuals (Schou, Christensen-Dalsgaard, and Thompson, 1994). To choose a value of μ , we have examined tradeoff curves, which are constructed by varying μ and plotting the rms of the residuals against the magnitude of the integral in the penalty term. The changes in a_1 that underlie the difference in the tradeoff curves for the different analyses were shown in Figure 3.8. The tradeoff curves themselves (shown in Figure 3.15) were computed using a modeset constructed by finding the modes common to all eleven analyses for each time interval and taking the average in time over whatever modes were present; in this case the errors used are the errors on the average.

As one can see, the image-scale correction made a substantial difference to the tradeoff curve. The curve for the cubic distortion correction is nearly indistinguishable. The correction for CCD misalignment made another significant reduction in the residuals, but the curves for the next four changes to the analysis all lie between the previous two. Accounting for the horizontal displacement caused a substantial increase in the residuals, but accounting for the Woodard effect resulted in the lowest curve shown. The use of asymmetric profiles made no change to the tradeoff curve. This is basically in line with what one might expect based on the differences in a_1 resulting from each change in the analysis shown in Figure 3.8.

To choose a value of μ , one typically looks for the “elbow” in the tradeoff curve: the place where the residuals stop decreasing sharply, so that further decreases of μ will be of little benefit. Unfortunately, there seem to be two elbows in the curves

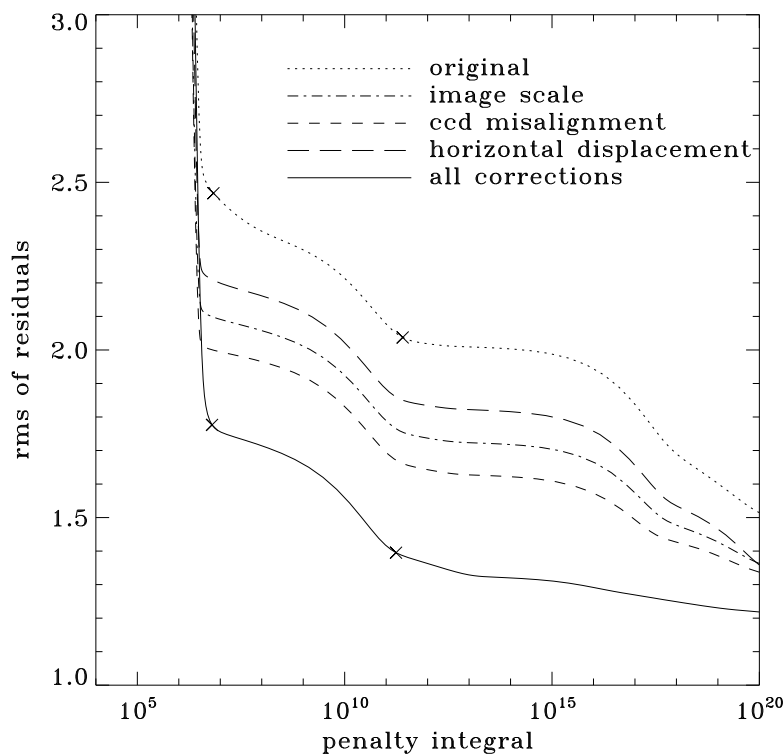


Figure 3.15. Tradeoff curves for several analyses. Dotted curve is for original analysis. Dash-dot curve shows first correction. Short-dashed curve shows first three corrections. Long-dashed curve shows first eight corrections (note this curve is above the one for only the first correction). Solid line is for all corrections. Symbols, from left to right, indicate tradeoff parameters of $\mu = 10^{-4}$ and $\mu = 10^{-9}$.

shown in Figure 3.15. For the initial and final analyses, we have marked the point corresponding to the highest reasonable value of μ (10^{-4}) and the lowest value one might reasonably use (10^{-9}). Furthermore, if the model were a good fit to the data, for the lowest values of μ the tradeoff curve should approach a value of 1.0, which it does not.

In Figure 3.16 we show the normalized residuals of the inversions for the original and final analyses and for the smallest and largest values of μ given above. As one can see, the bump was mostly unaffected by all the changes in the analysis. A smaller value of μ decreases the size of the bump, but as Figure 3.17 shows, the resulting rotation profile is unrealistic. The fact that the bump is only marginally present in the residuals for $\mu = 10^{-9}$ suggests that this systematic error is responsible for the “knee” in the tradeoff curves. Notably, even this small value of μ was not able to fit the horns in the original analysis, which are greatly reduced in the final analysis. This is likely the cause of the overall reduction in χ^2 .

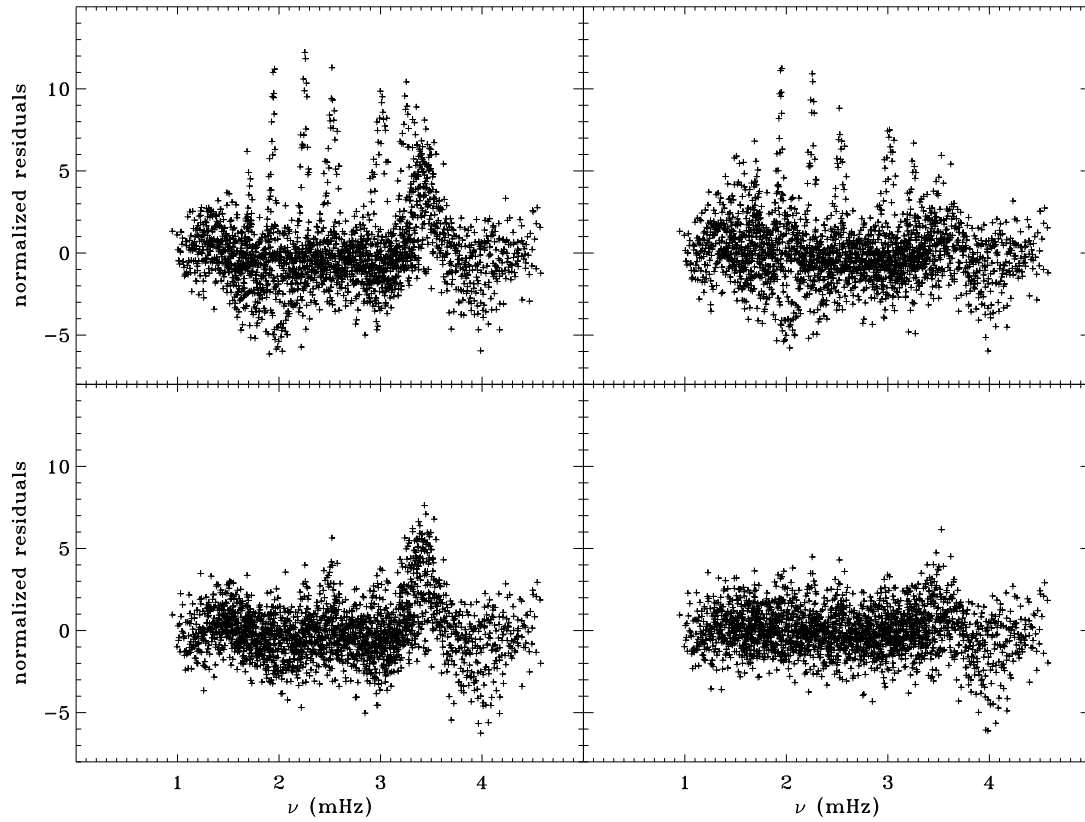


Figure 3.16: Normalized residuals as a function of frequency. Top panels show original analysis, bottom panels show analysis with all changes applied. Left panels show $\mu = 10^{-4}$, right panels show $\mu = 10^{-9}$. The sense of subtraction is the opposite of Figure 3.1 for ease of visual comparison.

To investigate the annual periodicity in the f -mode frequency variations, we used the common modesets described above to fit a function of the form

$$f(t) = A \sin(\omega_{\text{yr}} t) + B \cos(\omega_{\text{yr}} t) + Ct + D \quad (3.27)$$

to the average fractional f -mode frequency shift relative to its average over time, where $\omega_{\text{yr}} = 2\pi/365.25$ and t is measured in days. We did separate averaging and fits for four different ranges in degree $[\ell]$: 101 to 150, 151 to 200, 201 to 250, and 251 to 300. In each case, for each ℓ we took the average over whatever intervals it was fit in.

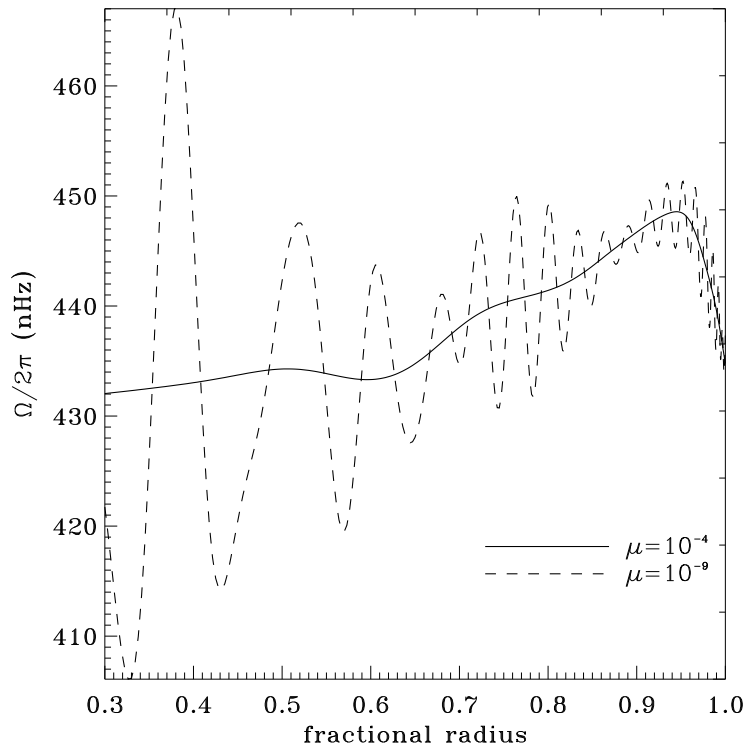


Figure 3.17. Internal rotation as a function of radius for the final analysis; curves for original analysis are similar. The solid line is the inversion result using $\mu = 10^{-4}$; the dashed line uses $\mu = 10^{-9}$.

Then, for each interval, we took the difference between each ℓ and the time average, divided by the time average, and then averaged over the range in ℓ . We performed a weighted least-squares fit to this data, which yielded values for the parameters A , B , C , D , and their corresponding errors.

The images produced by MDI, however, are taken at equal intervals of time on the spacecraft, whereas it would be optimal if they were taken at equal intervals of time on the Sun. To correct for this effect, we applied the relativistic Doppler shift due to the motion of the spacecraft. That is, we multiplied each frequency and its error by $\sqrt{(c+v)/(c-v)}$ where c is the speed of light and v is the average velocity of the spacecraft away from the Sun, as derived from the `OBS_VR` keyword of the input dopplergrams for each 72-day interval. The resulting fits are shown in Figure 3.18, as well as the shift caused by the Doppler correction.

The amplitude of the annual component has a large variation between the different analyses, but in general it is always greater for the higher ranges in ℓ . The point in

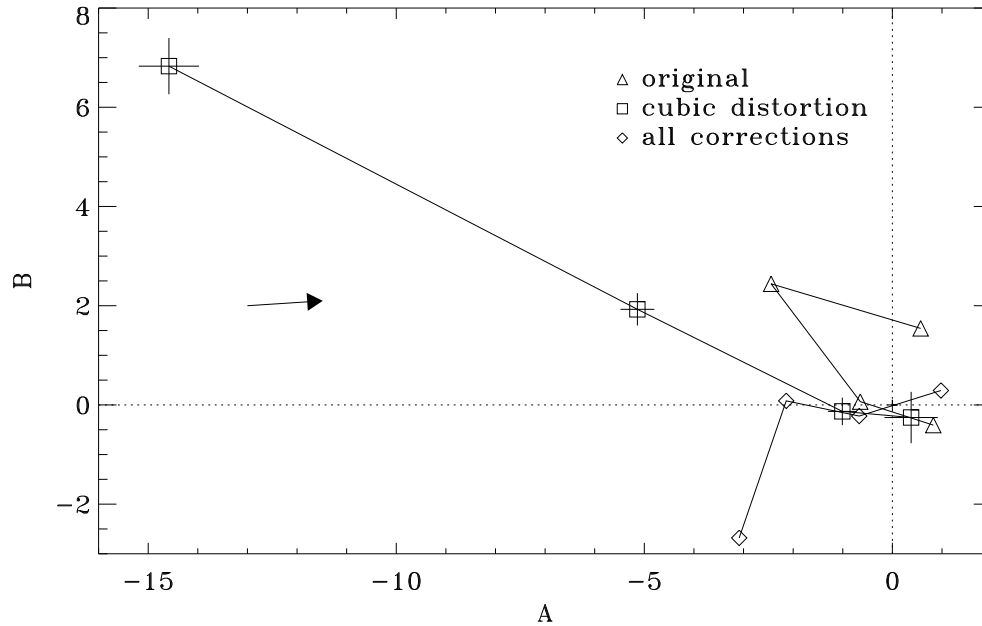


Figure 3.18: Amplitude of cosine vs. sine component of annual periodicity for three analyses after Doppler correction: triangles show original analysis, diamonds show final analysis, and squares show the correction for cubic distortion, which yielded the largest amplitude of the annual component. Solid lines connect points for different ranges in ℓ , beginning with the lowest range on the lower right. The arrow shows the size and direction of the shift resulting from the Doppler correction. The errors on A and B were similar for all analyses; the error bars show an average value. All values have been multiplied by 10^6 to match the units in Figure 3.3.

the plot for $\ell=251-300$ of the original analysis contradicts that trend, but it must be noted that the fit represented by that point was an extremely poor one, which is likely related to the horns in the original analysis. For the lower two ranges in ℓ , the amplitude was only marginally significant. Although not shown here, we note that the slope C was zero for the lowest range in ℓ , and becomes steadily more negative as ℓ increased, in agreement with previous findings (Antia *et al.*, 2001).

Finally, to explore the anomalous peak in the near-surface rotation rate near the poles (the high-latitude jet), we used the fits with 36 a -coefficients to perform two-dimensional RLS inversions for internal rotation. In this case we minimize

$$\sum_{n\ell s} \left[\frac{1}{\sigma_{2s+1}(n, \ell)} \left(\int_0^1 \int_0^\pi K_{n\ell s}(r, \theta) \bar{\Omega}(r, \theta) dr d\theta - a_{2s+1}(n, \ell) \right) \right]^2 + \mu_r \int_0^1 \left(\frac{d^2 \bar{\Omega}}{dr^2} \right)^2 dr + \mu_\theta \int_0^\pi \left(\frac{d^2 \bar{\Omega}}{d\theta^2} \right)^2 d\theta \quad (3.28)$$

in perfect analogy with Equation 3.26 (Schou, Christensen-Dalsgaard, and Thompson, 1994). We formed common modesets and averaged them using the same method described above for one-dimensional inversions, and used tradeoff parameters of $\mu_r = 10^{-6}$ and $\mu_\theta = 10^{-2}$ for the radial and latitudinal regularization terms respectively. Using this relatively high value for μ_θ should dampen variations in latitude (Howe *et al.*, 2000). The results are shown in Figure 3.19; the jet is more pronounced in this plot than in Figure 3.2, which can be attributed both to the different modeset and to the smaller errors resulting from averaging. Although in every updated analysis the polar jet actually had a greater magnitude than in the original analysis, the gapfilling resulted in a reduced rotation rate in the lower convection zone, which brings our result closer to agreement with inferences drawn by the GONG analysis (Schou *et al.*, 2002).

3.5 Discussion and Future Prospects

We have found that the various changes that we made to the processing of medium- ℓ data from MDI resulted in significant changes in mode parameters. In summary, changes in width were overall the least significant, followed by the changes in a_1 , which mostly resulted from correcting for the distortion of eigenfunctions by the differential rotation (the Woodard effect). The background was largely unaffected by most changes except the improved detrending and gapfilling. The image-scale correction made the dominant changes to the amplitudes and frequencies. For the latter, large changes also resulted from accounting for asymmetry, horizontal displacement,

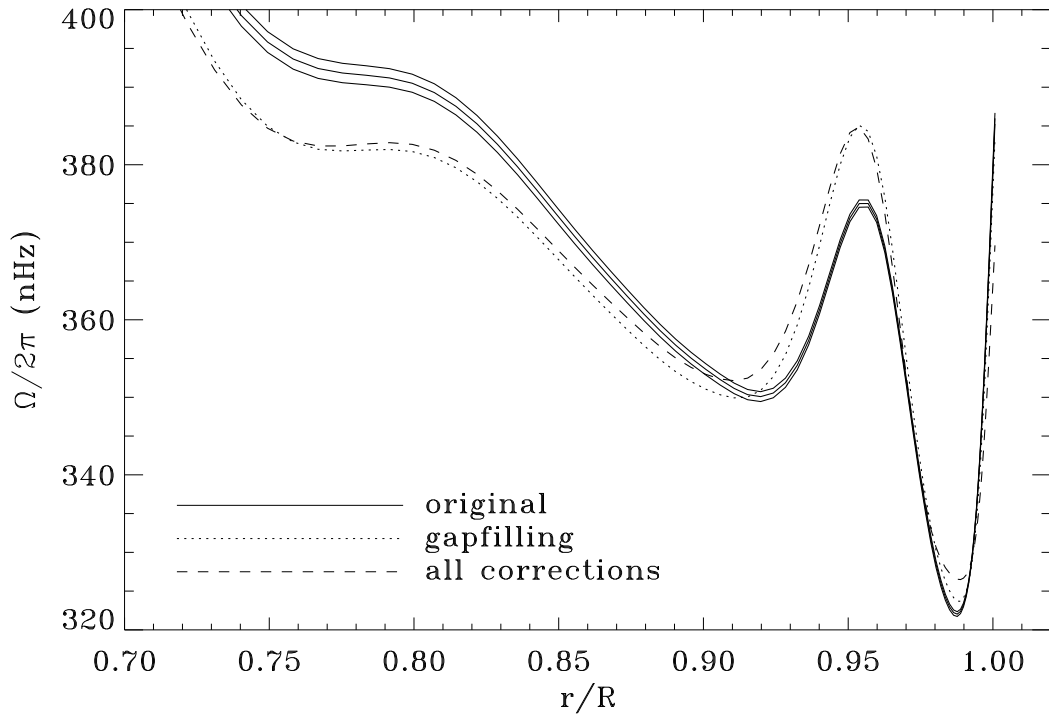


Figure 3.19: Internal rotation as a function of radius at 75° latitude for three analyses. Solid lines show the original analysis and its error bars; errors on the other analyses are similar. The dotted curve is the analysis that includes the improved gapfilling, and the dashed curve is the final analysis.

the Woodard effect, and cubic distortion, in decreasing order of significance.

Not only is one led to believe these changes represent an improvement as a matter of principle, but some of the systematic errors in the analysis have been reduced as well. In particular, the horns have been greatly reduced, resulting in overall lower residuals from rotational inversions. A more stubborn systematic error is the bump in the odd a -coefficients, which seems to be reflected in the anomalous shape of the tradeoff curve. This remained almost completely unchanged in all analyses. Nor did any change to the analysis make a reduction in the high-latitude jet just below the solar surface, although there is an improved agreement with GONG in the lower convection zone.

Regarding the annual periodicity in the f -mode frequencies, we found that the first change that we applied, the image-scale correction, resulted in a drastically increased magnitude of the annual component for the higher two ranges in ℓ . The correction for cubic distortion resulted in an even higher amplitude. After correcting for the misalignment of the CCD, however, the amplitude was reduced and did not vary much for later changes. We conjecture that the original fits were so poor at high ℓ (thus the horns) that the one-year period was swamped by noise there. The image-scale correction, which was the most significant one for the frequencies, itself has a one-year period due to its dependence on observer distance. Hence this correction revealed the remaining annual periodicity in the f -mode frequencies, which appears to result mostly from errors in P_{eff} . Due to symmetry, one would expect the frequency error to depend on the absolute value of the error in P_{eff} . The inclination error by itself would therefore be expected to result in a six-month period, but the combination with the misalignment of the CCD causes a one-year period. Hence, although the correction for CCD misalignment is constant in time, it still greatly reduces the annual component.

Of concern to us is the discrepancy between the 360-day analysis, which in principle should be more accurate, and the 72-day analysis. Most notably, it indicates a problem with our model of the background. Interestingly, the asymmetry was the only parameter for which the error was greater for the 360-day fits (at low frequency), and adding the asymmetry also made significant changes to the background and its error.

In spite of these shortcomings, the analysis of the MDI data in its entirety allows us to determine mode parameters with extraordinary precision. This is illustrated in Figure 3.20, where we show mode coverage in the ℓ - ν plane along with the estimated uncertainty on the frequencies.

Although our analysis has in general been very successful, the core peakbagging routines were written at a time when computational capabilities were far less than now. A number of approximations which were necessary 20 years ago could now be lifted. The current work is an attempt to remove some of these limitations. Over the years, other workers in the field have also made contributions to the problem of

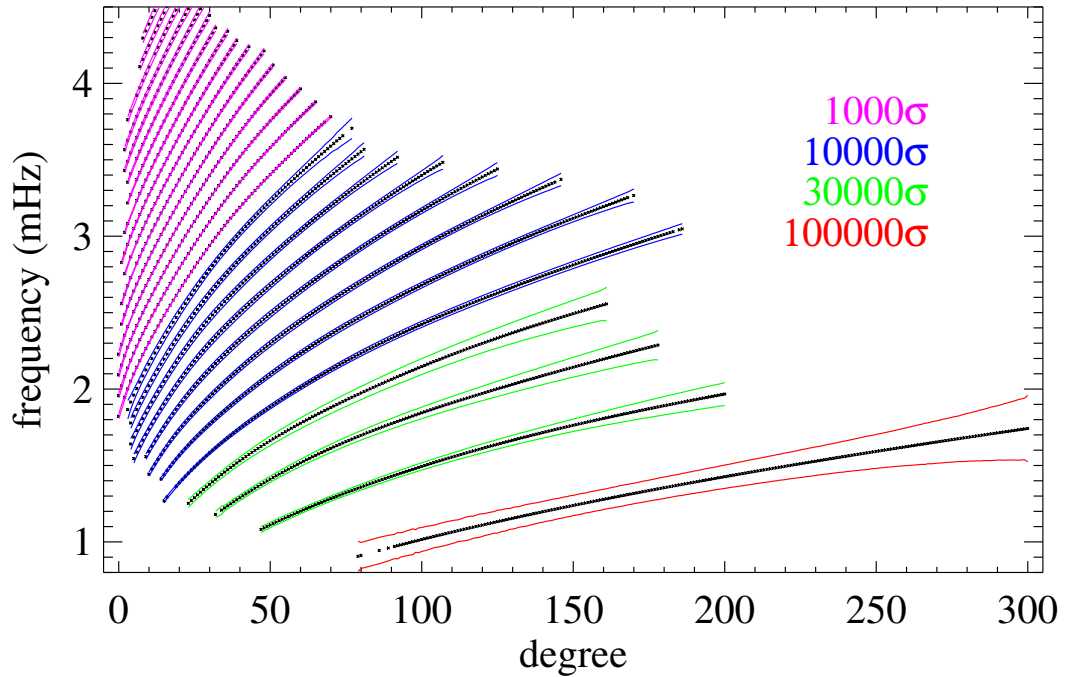


Figure 3.20: An ℓ - ν diagram with magnified errors. Dots represent a mode that was fitted in at least 12 of the 15 years we analyzed using symmetric profiles. Solid lines show the errors: for the f -mode, these have been multiplied by 100 000. For $n = 1, 2, 3$ the errors have been multiplied by 30 000. The next eight ridges ($n = 4 - 11$) have errors multiplied by 10 000. The remaining ridges have errors multiplied by 1000.

inferring physical properties of the Sun from medium- ℓ MDI data. Vorontsov and Jefferies (2013) have proposed fitting power spectra for rotation directly, circumventing the need to measure frequencies. As an intermediate step they have still done so, using more physically motivated spectral models and an analytically calculated leakage matrix. Korzennik (2005) has used sine multi-tapers as power-spectrum estimators and fit widths and asymmetries as functions of m . Reiter *et al.* (2015) have fit m -averaged spectra using a methodology that extends to high ℓ .

A potential difficulty facing these efforts is the computation of the leakage matrix. In general, the use of a leakage matrix should increase the stability of fits, but the results will then depend upon the assumptions that went into its calculation. In

particular, one might consider using leakage matrices calculated for different observer distances and values of B_0 . This has been done explicitly by Korzennik and Eff-Darwich (2013) and analytically by Vorontsov and Jefferies (2013). Others have attempted to fit the coupling of modes by subsurface flows, among them Schad, Timmer, and Roth (2013) and Woodard *et al.* (2013).

Although a comparison between the results of these other investigators and our improved analysis is still pending, all agree that some systematic errors remain in every analysis. These have been variously attributed to anisotropy in the point-spread function of MDI, failure to account for the height of formation in the solar atmosphere of the observed spectral line or the difference in light travel time between disk center and limb, and the effect of convective flows on the phase of the oscillations.

For us, there are a number of ways to move forward. The most obvious is the extension of this work to other datasets. First and foremost of these must be the MDI full-disk data, which will allow us to determine how systematic errors and mode parameters might depend on the smoothing of the medium- ℓ data and its apodization. Because of its duty cycle the full-disk data cannot be used to study the annual periodicity in our results, but now the *Helioseismic and Magnetic Imager* (HMI: Schou *et al.*, 2012) onboard the *Solar Dynamics Observatory* (SDO) has taken a long enough span of data for it to be suitable for this purpose. Phil Scherrer (private communication, 2014) has suggested that the one year period may be related to the variable (in solar coordinates) width of the gaussian used for smoothing the medium- ℓ data; an analysis of the MDI medium- ℓ proxy from HMI should elucidate the issue. Finally, a repetition of the comparison with GONG results is long overdue. The original comparisons all used GONG classic data; now that GONG+ (Hill *et al.*, 2003) has been in place for over 13 years and software pipelines in both projects have been updated, the time has come to renew an investigation of the systematic differences between the two.

There still remain possibilities for progress with the MDI medium- ℓ dataset itself. One that is suggested by the results of this article is to correct the timeseries for the relative motions of SOHO and the Sun. Although we can correct the frequencies after the fitting by Doppler shifting them, there is no obvious way to correct

the other mode parameters. Another change in the analysis that suggests itself is to the width of the fitting window, since this is one of the things most notably different in the GONG analysis and is also known to affect the shape of the bump in the a -coefficients. During the remapping performed prior to spherical harmonic decomposition, we could implement an interpolation algorithm that takes into account the correlation between points introduced by the gaussian smoothing. We have also considered the common practice of zero-padding our timeseries before performing Fourier transforms. Lastly, the parameter space of the detrending and gapfilling remains almost entirely unexplored.

Acknowledgements

This work was supported by NASA Contract NAS5-02139. SOHO is a mission of international cooperation between NASA and ESA. The authors thank the Solar Oscillations Investigation team at Stanford University and its successor, the Joint Science Operations Center. We thank Rasmus Larsen in particular for providing the gapfilling code. Much of the work presented here was done while J. Schou was at Stanford University. T.P. Larson thanks the Max-Planck-Institut für Sonnensystemforschung for generously hosting him during the composition of this article.

Chapter 4

Analysis of Full-Disk Datasets from MDI and HMI

The material in this chapter is being prepared as Global-Mode Analysis of Full-Disk Data from the Michelson Doppler Imager and Helioseismic and Magnetic Imager for submission to *Solar Physics*, coauthored with Jesper Schou. Therefore, throughout this chapter, Chapter 3 is referred to as LS. I wrote all the text and performed all the analysis presented here. As before, Jesper Schou wrote several of the core routines.

4.1 Introduction

Designed to be the successor to the *Michelson Doppler Imager* (MDI: Scherrer *et al.*, 1995), the *Helioseismic and Magnetic Imager* (HMI: Schou *et al.*, 2012) was launched onboard the *Solar Dynamics Observatory* (SDO) in February 2010. The designs of the two instruments are quite similar; here we shall note the differences between the two projects most pertinent to global-mode analysis. HMI is equipped with a 4096×4096 CCD and takes images with a spatial resolution of about 0.5 arcsec per pixel, or about four times that of MDI. HMI is in geosynchronous orbit, whereas MDI orbits the Sun-Earth L1 Lagrange point; partially for this reason, HMI is able to send down much more telemetry. Among other observables, HMI produces full-resolution dopplergrams at a cadence of 45 seconds. Lastly, HMI observes the FeI 6173 Å

spectral line, so it sees a slightly lower height in the solar atmosphere than MDI, which observed the Ni I 6768 Å line (Fleck, Couvidat, and Straus, 2011).

Global-mode analysis of data from MDI’s Medium- ℓ Program and systematic errors therein was described by Larson and Schou (2015), hereafter referred to as LS. Before an attempt can be made to extend this analysis to HMI data, it is fitting to compare it to the analysis of the MDI full-disk data. Although one might expect the two MDI analyses to be in near-perfect agreement, our investigation reveals surprising differences. In particular, systematic errors such as the “bump” seen in the normalized residuals of the odd a -coefficients and the anomalous peak in the near-surface rotation rate at high latitudes have different characteristics in the analysis of full-disk data.

MDI full-disk data are available throughout the mission, but usually with a low duty cycle. Nominally, for two months per year telemetry was allocated to send down the full-disk images continuously. These time intervals constitute the dynamics runs. As discussed in the next section, the actual lengths of the dynamics runs varied widely across the mission, as well as their timing within the year.

One might say that the primary difference between the MDI full-disk data and the low-resolution data (labelled `vw_V`, see LS) is that the latter are smoothed and subsampled (see Section 4.3), leaving them with a resolution one fifth that of the full-disk data. However, another important difference is that the full-disk data go closer to the limb; in particular an inner apodization radius of $0.9R$ is used, R being the image radius. The `vw_V` data, however, are cropped to about that same radius onboard the spacecraft, so an inner apodization radius of $0.83R$ is used. Further details are provided in Section 4.3.

In order to provide continuity with the MDI Medium- ℓ Program, we use the HMI data to create a `vw_V` proxy. This also allows us to investigate the annual periodicity seen in the f -mode frequencies from the analysis of MDI `vw_V` data.

In the next section we describe the datasets used in our analysis. In Section 4.3 we discuss how these data were analyzed, with emphasis on how each analysis differs from the analysis in LS. Section 4.4 gives the results, first for MDI and then for HMI, followed by a comparison of the two instruments. Finally, in Section 4.5 we discuss these results and propose how we might move forward.

4.2 Data

Beginning in 1996, MDI was continuously operated in full-disk mode for a few months each year through 2010. We therefore have 15 time intervals to analyze, known as the dynamics runs. To choose the exact intervals to use for global-mode analysis, one must balance the lengths of the timeseries and their duty cycles. For the most part, we have followed previous investigators, notably Rabello-Soares, Korzennik, and Schou (2008) and Rhodes *et al.* (2011). In our case, the simplest criterion is maximizing mode coverage. Another factor we consider is choosing intervals similar to each other in order to facilitate comparing them.

For the year 2000 only 45 days of continuous data were available and for 2003 only 38 days were available. There were, however, small additional sections of continuous data for those years, separated from the previously used time intervals by sections with a low duty cycle. We therefore extended both timeseries. In 2002 the situation was reversed; more data were available on the other side of a large gap, but including it did not result in substantially increased mode coverage. Therefore we chose a length that was closer to the other dynamics runs.

The first part of Table 4.1 shows the timeseries we used for the analysis presented here. The second part of the table shows timeseries used by various other researchers. In both cases, the timeseries and resulting mode parameters can be downloaded from Stanford’s Joint Science Operation Center (see the Appendix for details). The exception is the 12-day long timeseries in 2003, which was too short for the mode fitting to succeed.

In order to make comparisons with the `vw_V` data, we use the same 15 time intervals for two other analyses. Firstly, we use the regular `vw_V` data. Secondly, we use the full-disk images but apodize them like the `vw_V` data. We also attempted to use the full-disk apodization on `vw_V` images that we reconstructed from the full-disk images, but this was only possible for the years 1996 and 1998, because for the other years the gaussian convolution kernel used for the smoothing reached outside the full-disk crop radius, resulting in the loss of large amounts of data. These last two variations in the analysis required the computation of new leakage matrices. Details of the apodization are provided in the next section.

Table 4.1: Dynamics timeseries. Day numbers refer to the first day of the timeseries and are given relative to the MDI epoch of 1 January 1993 00:00:00_TAI. All timeseries begin on the first minute of the start date and end on the last minute of the end date. Duty cycles are given for the raw timeseries (DC1) and the timeseries after gapfilling (DC2). The number of modes fitted with six a -coefficients (NM6) and with 36 a -coefficients (NM36) is also given.

Day	Length	Start Date	End Date	DC1	DC2	NM6	NM36
1238	63	23 May 1996	24 Jul 1996	0.93	0.98	2039	1729
1563	93	13 Apr 1997	14 Jul 1997	0.91	0.98	2106	1840
1834	92	09 Jan 1998	10 Apr 1998	0.90	0.97	2132	1862
2262	77	13 Mar 1999	28 May 1999	0.92	0.97	2101	1809
2703	98	27 May 2000	01 Sep 2000	0.74	0.89	2056	1770
2980	90	28 Feb 2001	28 May 2001	0.91	0.97	2088	1837
3331	109	14 Feb 2002	02 Jun 2002	0.85	0.96	2092	1839
3904	76	10 Sep 2003	24 Nov 2003	0.58	0.75	1988	1603
4202	65	04 Jul 2004	06 Sep 2004	0.87	0.96	2062	1741
4558	67	25 Jun 2005	30 Aug 2005	0.92	0.98	2082	1755
4830	62	24 Mar 2006	24 May 2006	0.89	0.98	2073	1723
5454	58	08 Dec 2007	03 Feb 2008	0.87	0.98	2032	1687
5540	64	03 Mar 2008	05 May 2008	0.85	0.96	2088	1740
5981	65	18 May 2009	21 Jul 2009	0.75	0.84	2017	1631
6335	67	07 May 2010	12 Jul 2010	0.85	0.93	2031	1704
2703	45	27 May 2000	10 Jul 2000	0.93	1.00	1919	1556
3296	27	10 Jan 2002	05 Feb 2002	0.86	0.93	1864	1127
3331	98	14 Feb 2002	22 May 2002	0.86	0.97	2081	1821
3368	72	23 Mar 2002	02 Jun 2002	0.90	0.97	2056	1717
3904	12	10 Sep 2003	21 Sep 2003	0.81	0.98	0	0
3942	38	18 Oct 2003	24 Nov 2003	0.81	0.94	1921	1367

Table 4.2: HMI timeseries. Day numbers refer to the first day of the timeseries and are given relative to the MDI epoch. Duty cycles are given for the raw timeseries (DC1) and the timeseries after gapfilling (DC2).

Day	Start Date	DC1	DC2	Day	Start Date	DC1	DC2
6328	30 Apr 2010	0.996	1.000	7408	14 Apr 2013	0.986	0.991
6400	11 Jul 2010	0.982	0.995	7480	25 Jun 2013	0.990	0.997
6472	21 Sep 2010	0.968	0.995	7552	05 Sep 2013	0.967	0.997
6544	02 Dec 2010	0.989	0.995	7624	16 Nov 2013	0.993	0.997
6616	12 Feb 2011	0.963	0.991	7696	27 Jan 2014	0.969	0.997
6688	25 Apr 2011	0.997	1.000	7768	09 Apr 2014	0.989	0.995
6760	06 Jul 2011	0.987	0.997	7840	20 Jun 2014	0.991	0.997
6832	16 Sep 2011	0.966	0.991	7912	31 Aug 2014	0.972	1.000
6904	27 Nov 2011	0.990	0.997	7984	11 Nov 2014	0.992	0.997
6976	07 Feb 2012	0.966	0.997	8056	22 Jan 2015	0.963	0.991
7048	19 Apr 2012	0.998	1.000	8128	04 Apr 2015	0.989	0.993
7120	30 Jun 2012	0.990	0.997	8200	15 Jun 2015	0.989	0.997
7192	10 Sep 2012	0.971	0.997	8272	26 Aug 2015	0.970	0.997
7264	21 Nov 2012	0.993	0.997	8344	06 Nov 2015	0.978	0.990
7336	01 Feb 2013	0.972	0.997	8416	01 Jan 2016	0.972	0.997

In all cases, we use a window function common¹ to all analyses for each time interval as input to the gapfilling. The result was mainly to discard a large amount of the regular `vw_V` data. We did not repeat the analysis of the regular full-disk data using the common window function, but the native window function included at most 0.23% more data.

HMI began producing regular science data on 30 April 2010. Since that time, we have been performing medium- ℓ analysis of it using 72-day long timeseries in phase with the original MDI medium- ℓ timeseries. The time intervals for which results are presented here are shown in Table 4.2. We have also created 360-day long timeseries by concatenating the gapfilled 72-day long timeseries.

¹The window function is a timeseries of ones and zeros designating good and bad data points respectively. The common window function is the product of two or more others.

4.3 Method

The MDI full-disk data are processed in almost exactly the same way as the \mathbf{vw}_V data, that is, using the updated methodology described by LS. The most notable exception is that for the full-disk data it is possible to use a larger fraction of the input images; whereas the the \mathbf{vw}_V data are apodized with a cosine in fractional image radius from 0.83 to 0.87, the full-disk data are apodized in the same way from 0.90 to 0.95. It should also be noted that each analysis uses a leakage matrix appropriate to the data used. For the full-disk data, the leakage matrix is calculated as described by LS, except that the input images are not convolved with anything. In particular, we have not accounted for any point spread function, but this is expected to have little effect in the medium- ℓ regime

In summary, all analyses of MDI data presented here are corrected for various geometric effects during spherical harmonic decomposition: image-scale errors, cubic distortion from the instrument optics, misalignment of the CCD, an error in the inclination of the Sun’s rotation axis, and a potential tilt of the CCD. The spherical harmonic timeseries are then detrended and gapfilled as described by LS, and Fourier transforms of these are fit to extract the mode parameters. The fitting, or peakbagging as it is called, takes into account horizontal displacement at the solar surface and the distortion of eigenfunctions by the differential rotation (known as the “Woodard effect”). For the native full-disk analysis, the peakbagging is also repeated using asymmetric mode profiles in addition.

For the analysis of HMI data, the input images are already corrected for optical distortion. Hence, the only geometrical correction applied here is for the inclination error. After the spherical harmonic decomposition, the HMI data are processed almost exactly like the MDI full-disk data. In particular, the images are apodized in the same way, and therefore an identical leakage matrix is used. The peakbagging is performed using both symmetric and asymmetric mode profiles for both the 72-day long timeseries and the 360-day long timeseries.

In addition, we have created a proxy for the MDI \mathbf{vw}_V data from the HMI data. This is done by binning the HMI data by a factor of four to simulate the MDI full-disk

data, convolving them with a gaussian, and retaining only every fifth point in each direction as described by LS. The resulting images are then apodized like the MDI `vw_V` data and the peakbagging likewise uses the same leakage matrix. We have fit these data only as 72-day long timeseries and only using symmetric profiles.

Whether we use the HMI images in their native resolution or by way of the proxy, the most significant difference with the MDI processing is in the detrending. Whereas the MDI data needed to have discontinuities in the timeseries manually identified, for HMI this information can be derived from keywords in the input data. Furthermore, the quality of the HMI data are more carefully tracked, so the keywords also provide a reliable measure of what data are expected to be present.

Due to its orbit and potential problems with calibration, the HMI data contain a strong daily oscillation. We therefore detrend it using different parameters than the MDI data. Although in both cases the timeseries are detrended by subtracting Legendre polynomials of degree seven, for HMI these polynomials are fit to an interval of 1100 points (825 minutes) which is advanced by 960 points (720 minutes). In other words, the detrending intervals overlap by 140 points (105 minutes). For additional details, the reader is referred to LS

4.4 Results

4.4.1 MDI Mode Parameters

In total, we applied four different analyses to all 15 dynamics runs. For conciseness, we shall make use of the following additional labels: `fd_ap90` for the full-disk analysis using its regular apodization, `fd_ap90_as` for the same thing fit with asymmetric profiles, and `fd_ap83` for the full-disk data apodized like the `vw_V` data. We shall use the label `vw_ap83` when we use the `vw_V` with its regular apodization, but note that we processed it using a window function common to all analyses. We shall also use the label `vw_ap90` for the `vw_V` data apodized like the full-disk data, but note that this analysis is only available for the 1996 and 1998 dynamics runs. Figure 4.1 shows the number of modes fitted using six a -coefficients (which parameterize the dependence

of the frequencies on m , see LS) for all these analyses. As expected from our previous work, the mode coverage for the `fd_ap90_as` analysis as a function of time is basically the same as that for the `fd_ap90` analysis shifted downward. Interestingly, the other two analyses are closer in coverage to the `fd_ap90` analysis, with the exception of the 2003 dynamics run, which by far had the lowest duty cycle. Apparently the regular full-disk analysis was less susceptible to this than all the other ones. The effect of using asymmetric profiles on the mode parameters themselves will be discussed in the context of the HMI analysis.

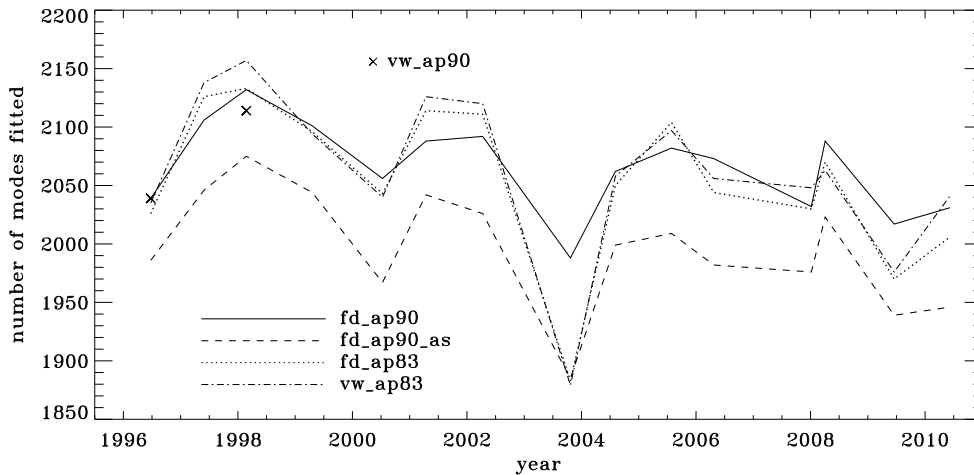


Figure 4.1: Mode coverage for all dynamics runs. Symbols show the number of modes fitted in 1996 and 1998 by the `vw_ap90` analysis.

In order to compare two different analyses, we must create common modesets. For example, in order to quantify the effect of the apodization, for each dynamics run we find the modes common to the `fd_ap90` and `fd_ap83` analyses. We then take a weighted average in time over whatever dynamics runs had each mode successfully fit. For the weights, we have used the length of each timeseries times its duty cycle. For this comparison, we have used the average error, rather than the error on the average, so that the significance shown is what one might expect from an average dynamics run. Lastly, the noise parameter b requires special treatment. Since e^b is proportional to the length of the timeseries, each background parameter has $\log(T/72.0)$ subtracted from it before averaging, where T is the length of the timeseries in days.

In Figure 4.2 we show the result for six mode parameters. For a full explanation of these, the reader is referred to LS. Clearly, the most significant change is to the amplitudes. One might think this is to be expected since the `fd_ap83` data are apodized to a smaller radius, but in fact this ought to be corrected for in the leakage matrix. In other words, the parameter A should represent the intrinsic amplitude of the mode *on the Sun*. Next most significant is the change to the background, which was lower for the `fd_ap83` analysis at lower frequencies, and higher at higher frequencies. The widths were lower for the `fd_ap83` analysis across all frequencies, especially between 2.0 and 3.0 mHz. Lastly, although not very significant, the bump seen in the difference in a_1 is encouraging, since it is in the same location as the bump we hope to eliminate.

Here we note that in the absence of systematic errors, these differences should all be small ($\ll 1\sigma$) near the peak power of the p -mode band (around 3.0 mHz), since the signal-to-noise ratio is high there (Libbrecht, 1992). In any case, the differences should have no trends in frequency or any other parameter. One source of random error, the stochastic excitation of the modes, is the same for all observers and apodizations, since over the majority of the medium- ℓ range the modes have long enough lifetimes to be considered truly global. Another source of random error, convective motions on the surface, could be different when using different parts of the solar disk, but this still should not cause any offsets in the frequencies, widths, or a -coefficients. Although the amplitudes and background parameters could be affected, such an effect would still be flat in frequency. Even when the signal-to-noise ratio is low, the changes should still be random. Hence, we can already see that there is a problem with the analysis.

To quantify the effect of smoothing and subsampling, we compare the `fd_ap83` and `vw_ap83` analyses in exactly the same fashion. Figure 4.3 shows the results. Here the convective noise is the same, as well as any instrumental effect, since the two datasets observe almost the same part of the solar disk. Indeed, with the exception of the background parameter, the smoothing and subsampling results in smaller changes than the apodization. The average of the other parameters shows almost no significance at all. In particular, the differences in the a -coefficients are hardly different from zero, which would suggest that the smoothing and subsampling has little effect on any inversion results.

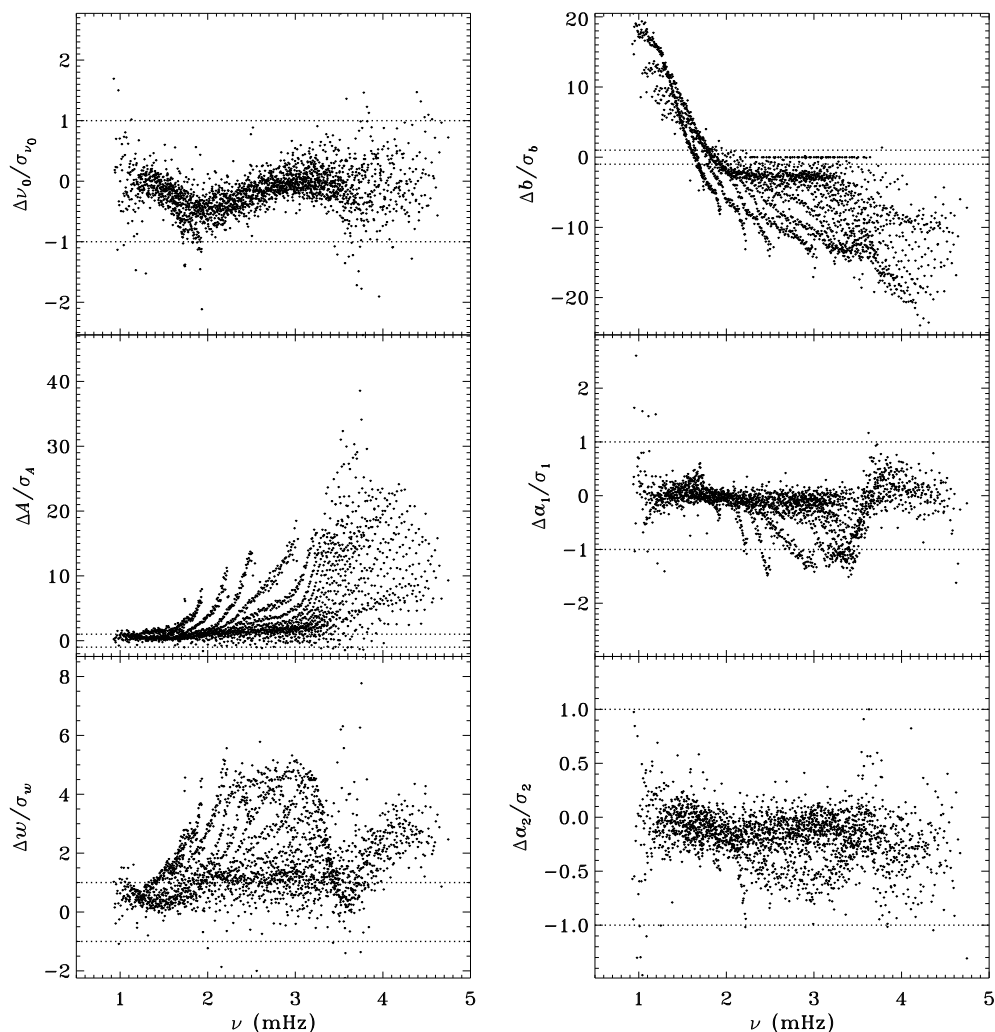


Figure 4.2: Effect of apodization on mode parameters. Shown are changes in frequency $[\nu_0]$, amplitude $[A]$, width $[w]$, background parameter $[b]$, a_1 , and a_2 in units of standard deviation. Each panel is scaled differently; dotted lines show the $\pm 1\sigma$ levels. For the a -coefficients, no more than nine points have been excluded from the range shown. The sense of subtraction is `fd_ap90` minus `fd_ap83`.

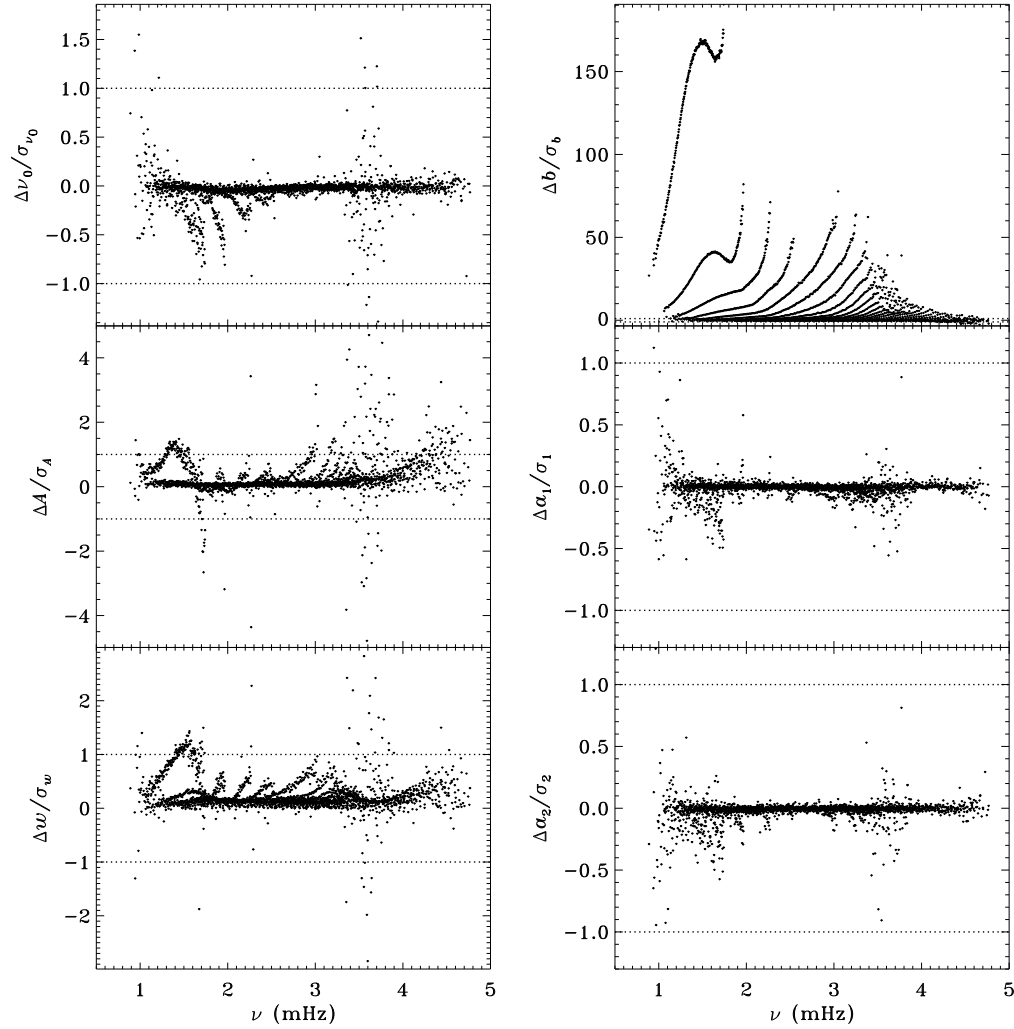


Figure 4.3: Effect of smoothing and subsampling on mode parameters. Shown are changes in frequency [ν_0], amplitude [A], width [w], background parameter [b], a_1 , and a_2 in units of standard deviation. For clarity, the bottom panels have at most 0.65% of points excluded. Each panel is scaled differently; dotted lines show the $\pm 1\sigma$ levels. The sense of subtraction is `fd_ap83` minus `vw_ap83`.

The small difference for the amplitude shown in Figure 4.3 is, however, deceptive. For all other parameters, the differences look roughly the same for the different dynamics runs, but for the amplitudes, the difference actually alternates in sign. This is shown in Figure 4.4, where we have plotted the mean significance as a function of time. We have as yet no explanation for this oscillation, but focus and tuning changes in the instrument are likely candidates.

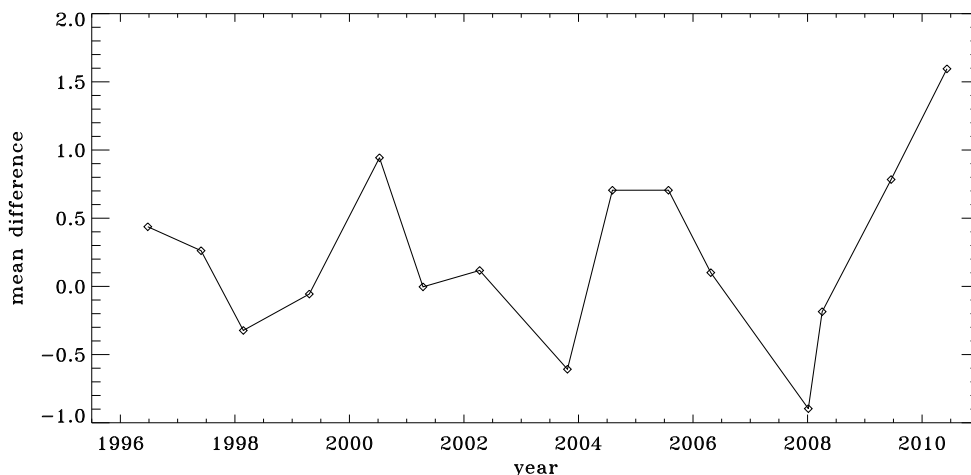


Figure 4.4: Effect of smoothing and subsampling on amplitudes. Shown are the mean changes in units of standard deviation, for all dynamics runs. The sense of subtraction is `fd_ap83` minus `vw_ap83`.

4.4.2 Systematic Errors in MDI data

To explore the effect of the different analyses on our systematic errors, we begin by performing simple one-dimensional regularized least-squares (RLS) rotational inversions using the a_1 -coefficient only, just as in LS. In this case, we formed modesets common to the `fd_ap90`, `fd_ap83`, and `vw_ap83` analyses for each dynamics run, and took the average in time as before, except that for inversions we always use the error on the average. The tradeoff curves in Figure 4.5 show the result. The curve for the `fd_ap90` analysis has the shape one hopes to see: a single “elbow” so that one may unambiguously choose a tradeoff parameter, not to mention that the χ^2 values

are closer to unity. It is satisfying to see that the value typically used, $\mu = 10^{-6}$, lies right where it should on the curve: “the place where the residuals stop decreasing sharply, so that further decreases of μ will be of little benefit” (LS). The other two curves are very close to the final curve we found in LS, and we have marked the tradeoff parameters we used previously.

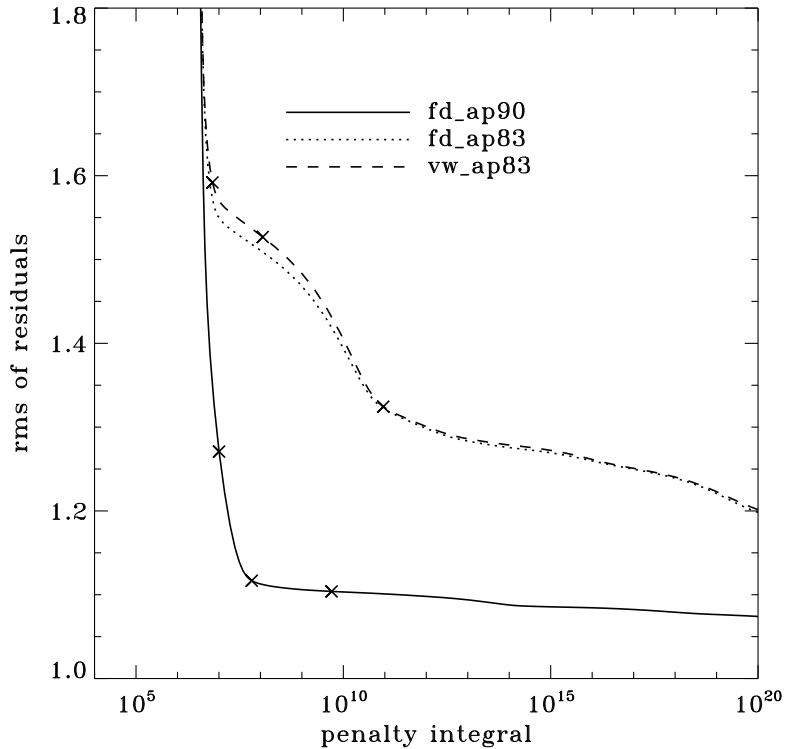


Figure 4.5. Tradeoff curves for an average over all dynamics runs. Symbols, from left to right, indicate tradeoff parameters of $\mu = 10^{-4}$, $\mu = 10^{-6}$, and $\mu = 10^{-9}$.

In order to see how the different analyses affect our inference of how the solar rotation varies with latitude, we perform two-dimensional RLS inversions using 36 a -coefficients. First, we form averages over the dynamics runs just as we did for the one-dimensional inversions. The residuals of a_1 resulting from inversions of these averages are shown in Figure 4.6. As one can see, the analyses using the `vw_V` apodization clearly show the bump, whereas it is essentially absent from the `fd_ap90` analysis. Investigating the polar jet, we found that it was clearly visible in inversions of the 1998 dynamics run alone, so we are able to compare all four analyses. Again, we took the modeset common to all four. As Figure 4.7 shows, we again see that using a

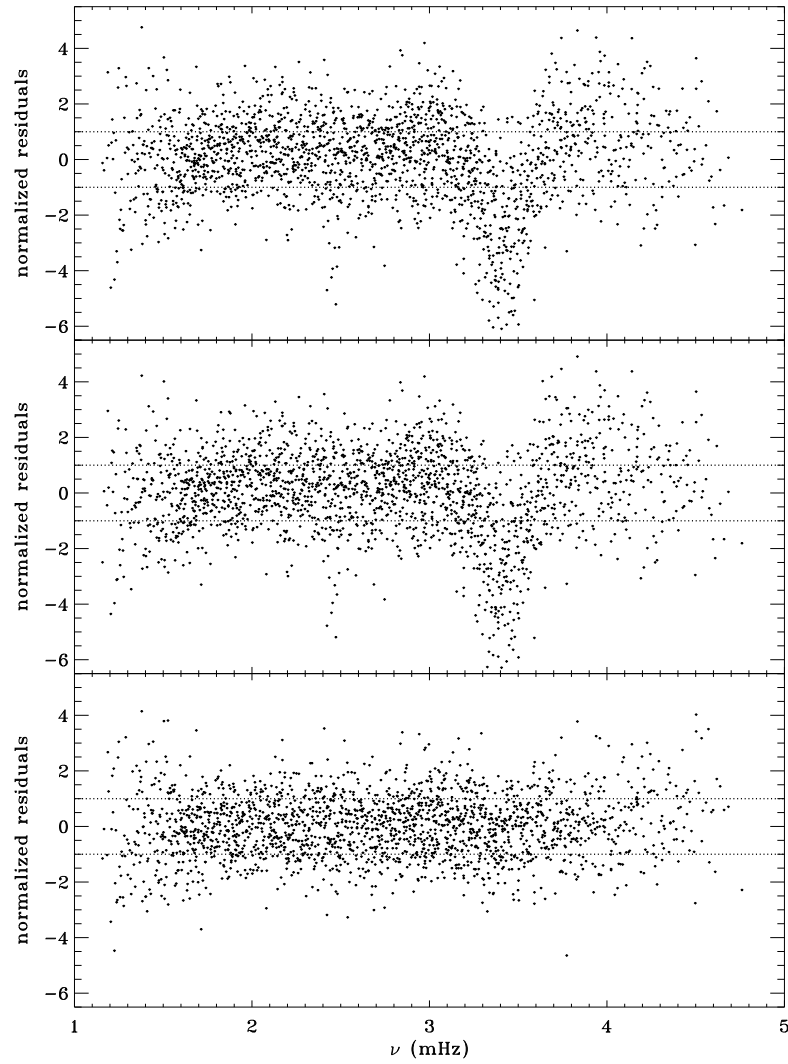


Figure 4.6: Normalized residuals of a_1 for the average over all dynamics runs. Shown from top to bottom are the vw_ap83 analysis, the fd_ap83 analysis, and the fd_ap90 analysis. Dotted lines show the $\pm 1\sigma$ levels.

smaller apodization radius results in the polar jet, while the larger apodization radius shows no sign of it. Here we must reiterate that the bump does not cause the jet; previous research has shown that excluding from the inversion modes that constitute the bump still shows the jet (Schou *et al.*, 2002). Hence, for both the bump and the jet, we are left with a puzzle. Using the *vw_V* apodization results in both systematic errors, which are then removed by using *more* data from the input images, although the data added is expected to contain only a small fraction of the helioseismic signal.

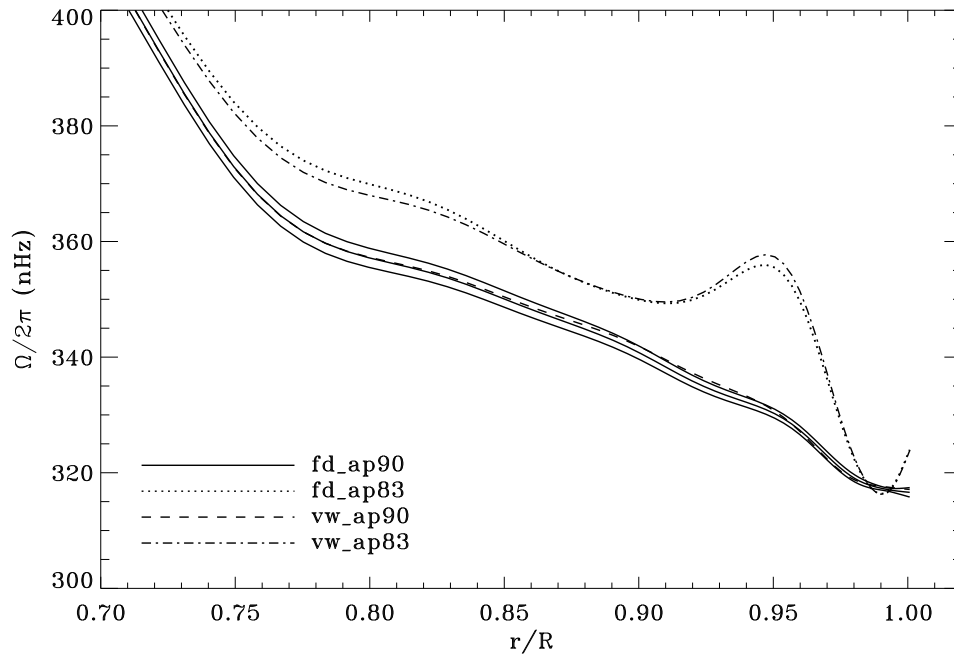


Figure 4.7: Internal rotation as a function of radius at 75° latitude for four analyses applied to the 1998 dynamics run. Solid lines show the *fd_ap90* analysis and its error; errors for the other analyses were similar.

4.4.3 HMI Mode Parameters

We have so far analyzed about six years of HMI data, as both 72-day and 360-day fits for the full-disk data, using both symmetric and asymmetric profiles. For the *vw_V* proxy, we have used only 72-day long timeseries and symmetric profiles. The resulting

number of modes fitted is shown in Figure 4.8. The difference in coverage between symmetric and asymmetric fits and between 360-day fits and 72-day fits is what we have come to expect based on our analysis of other datasets. Surprising, however, is the large oscillation in coverage of the fits to the *vw_V* proxy data, especially since it exceeds the coverage of the full-disk fits at its peak. We shall return to this fact later.

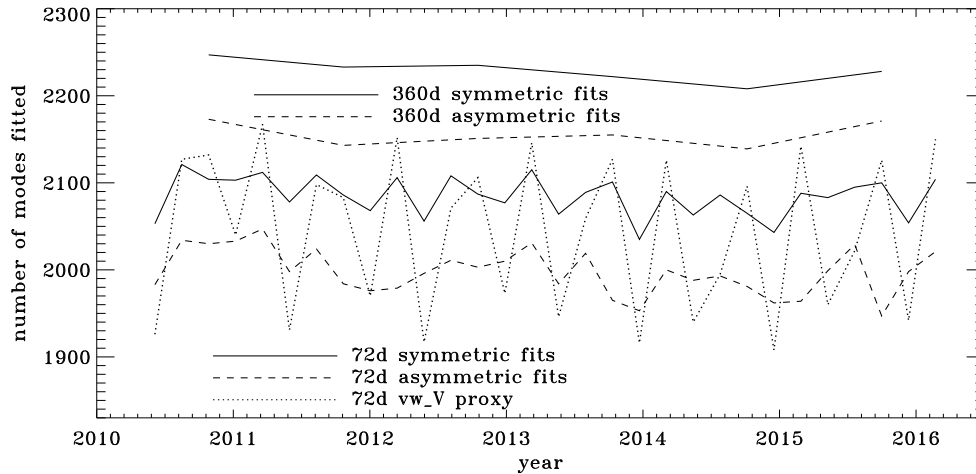


Figure 4.8: Number of modes fitted as a function of time for the first six years of HMI.

In LS we found that the fits using asymmetric profiles are much less stable than those using symmetric profiles. This is not surprising since the asymmetric fits require an extra parameter, but it does result in decreased mode coverage. However, in the region where the modes are observed to have strong asymmetry, one must accept that using asymmetric profiles more accurately characterizes them. Hence, the parameters resulting from both types of fitting have become standard data products. The difference in coverage is shown in Figure 4.9, where diamonds indicate a mode that failed at least once using symmetric profiles, and dots indicate a mode that failed at least once using asymmetric profiles. The difference in mode parameters themselves are shown in Figure 4.10, where we have performed averaging in the same manner as before, using the 72-day fits. This figure is to be compared to the last panel of Figures 4-8 in LS. Clearly, the asymmetric profiles have a large effect on the frequencies in a range between 1.0 and 3.0 mHz. The other mode parameters were similarly, but

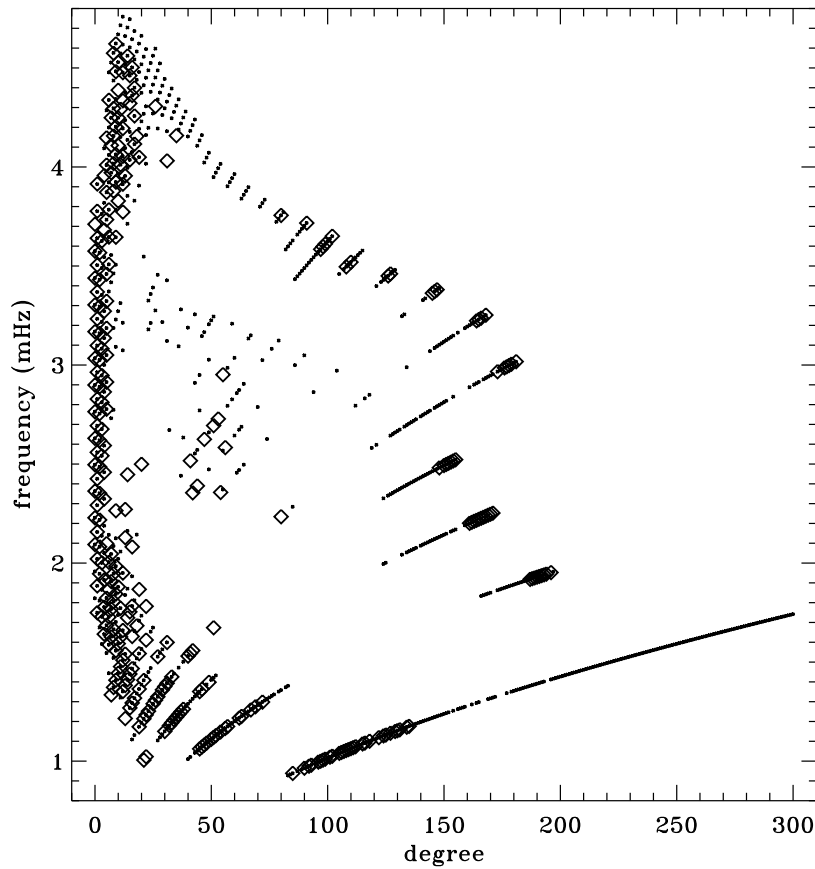


Figure 4.9. Difference in mode coverage for the first six years of HMI. Diamonds show modes that failed to fit at least once with symmetric profiles when asymmetric profiles succeeded, and dots show the opposite.

less significantly, affected in a slightly smaller frequency range, still centered at about 2.0 mHz. For the amplitudes, widths, and background parameters, there was also a large and opposite change above 3.8 mHz, while the frequency differences show a second peak around the same frequency. Although not shown here, we found similar differences using the MDI full-disk data. Hence, we can rest assured that the asymmetry of the modes is characterized the same by all the datasets we have studied. Unfortunately, this also means that the error magnification we saw for the frequencies and background parameters in LS is also present in the analysis of the full-disk datasets.

Our previous work also revealed discrepancies between 360-day fits and an average over 72-day fits for the MDI *vw_V* data, regardless of whether symmetric or

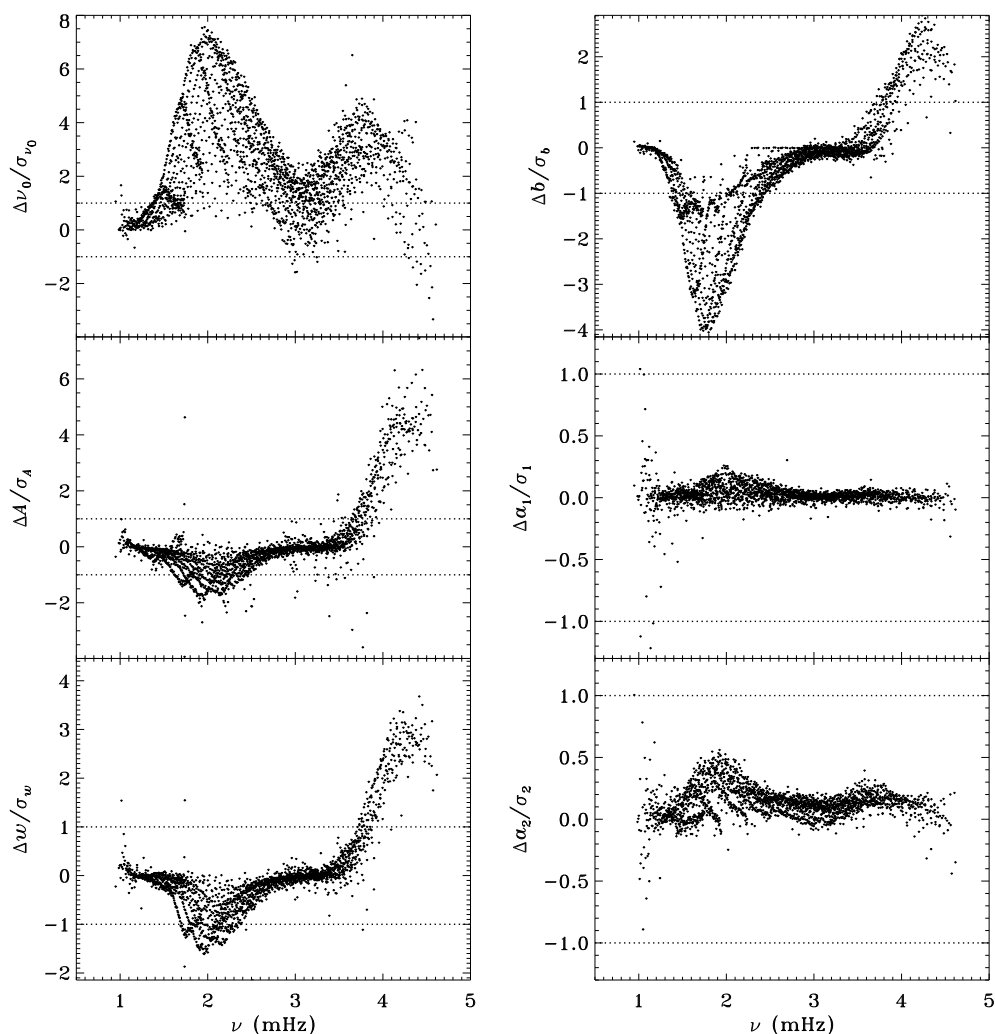


Figure 4.10: Effect of asymmetric profiles on mode parameters from 72-day fits. Shown are changes in frequency [ν_0], amplitude [A], width [w], background [b], a_1 , and a_2 in units of standard deviation. The data have been averaged over six years of HMI. Each panel is scaled differently; dotted lines show the $\pm 1\sigma$ levels. At most 0.18% of points have been excluded. The sense of subtraction is asymmetric minus symmetric.

asymmetric profiles were used. To confirm that this reflects a characteristic of the algorithm and not the data, we repeated the comparison for the first six years of HMI. Figure 4.11 shows the results using asymmetric profiles. Comparison with Figure 13 of LS reveals the same trends. The exception is the amplitude differences, but this can be attributed to the gaussian smoothing applied to the `vw_V` data. Although not shown here, we also found error ratios similar to those shown in LS. This would indicate that the difference has to do with the algorithm and not the data. However, Barekat, Schou, and Gizon (2014) found significant differences between the two instruments in the radial gradient of the rotation rate at high latitudes near the surface. In subsequent investigations, Barekat (private communication, 2015) also found that the results using the 360-day fits for HMI differed significantly from those using the averaged 72-day fits, while for MDI the two are essentially in agreement. Clearly, further study is needed to determine the source of these differences.

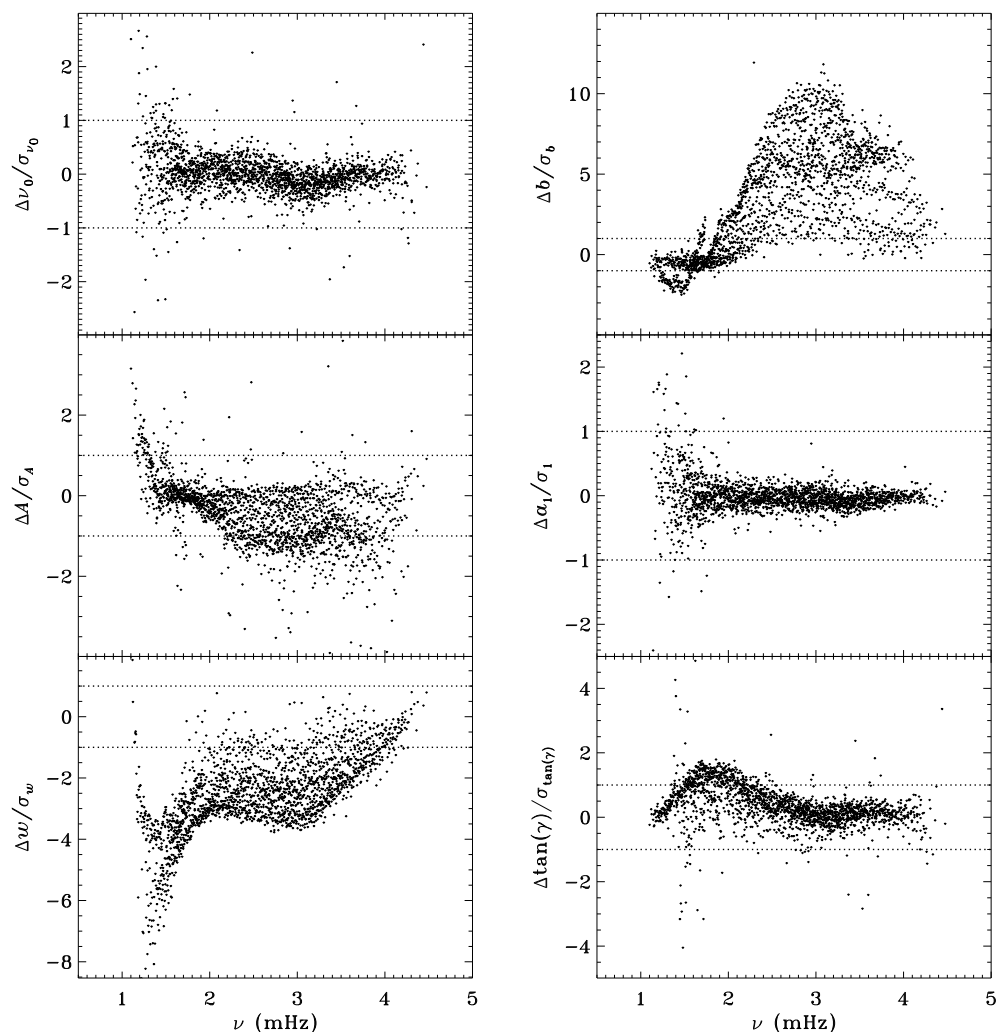


Figure 4.11: Difference between 360-day and 72-day fits in frequency $[\nu_0]$, amplitude $[A]$, width $[w]$, background $[b]$, a_1 , and asymmetry parameter in units of standard deviation. The data have been averaged over six years of HMI. Each panel is scaled differently; dotted lines show the $\pm 1\sigma$ levels. At most 0.66% of points have been excluded. The sense of subtraction is 360 day minus 72 day.

4.4.4 Systematic Errors in HMI data

We plot tradeoff curves and normalized residuals of a_1 for both the HMI full-disk and vw_V proxy analyses, shown in Figures 4.12 and 4.13, just as we did for the MDI data. Comparison reveals similar differences between the full-disk and low-resolution results as for MDI. The tradeoff curve shows higher residuals, and the bump in the residuals of a_1 is much more significant. For the rotation rate at high latitudes, HMI's time coverage allowed us to discover that the jet is only discernible when $|B_0|$ is maximal, although the two analyses still resulted in significantly different rotation rates. Further, the upturn in the rotation rate near the surface at 75° is more pronounced at these times for the vw_V proxy. When B_0 is close to zero we see the upturn in both analyses, but it is stronger for the vw_V proxy. Both features are clearly seen in an average over the six years we have analyzed, shown in Figure 4.14.

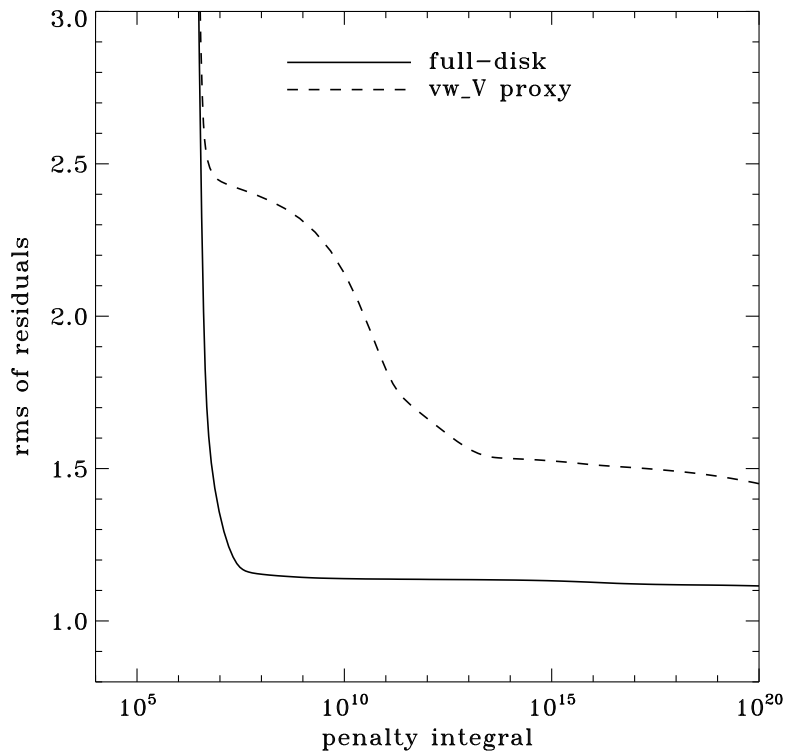


Figure 4.12. Tradeoff curves for an average over six years of HMI.

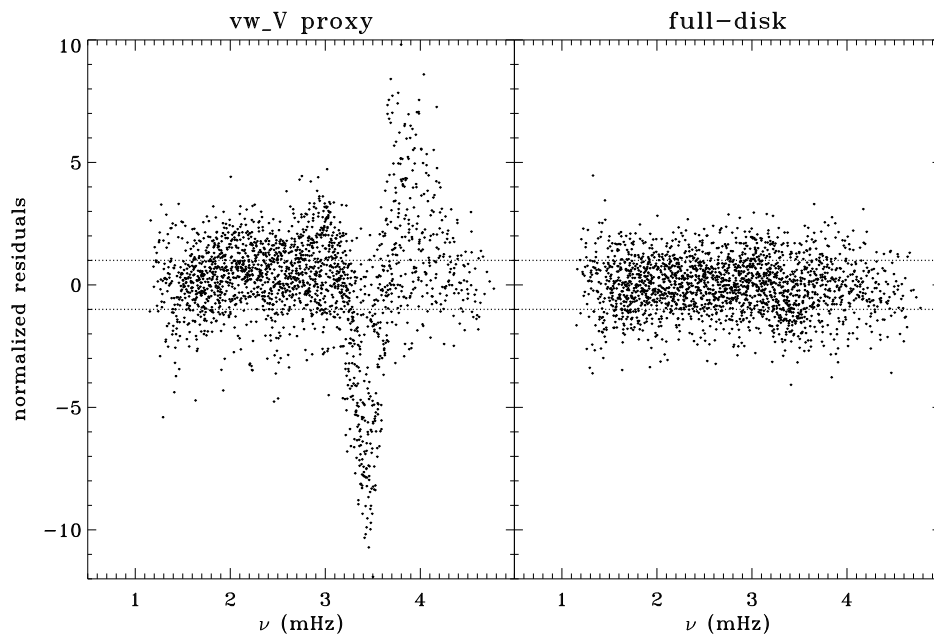


Figure 4.13: Normalized residuals of a_1 for an average over six years of HMI. Left panel shows the HMI *vw_V* proxy. Right panel shows the full-disk HMI analysis. Dotted lines show the $\pm 1\sigma$ levels.

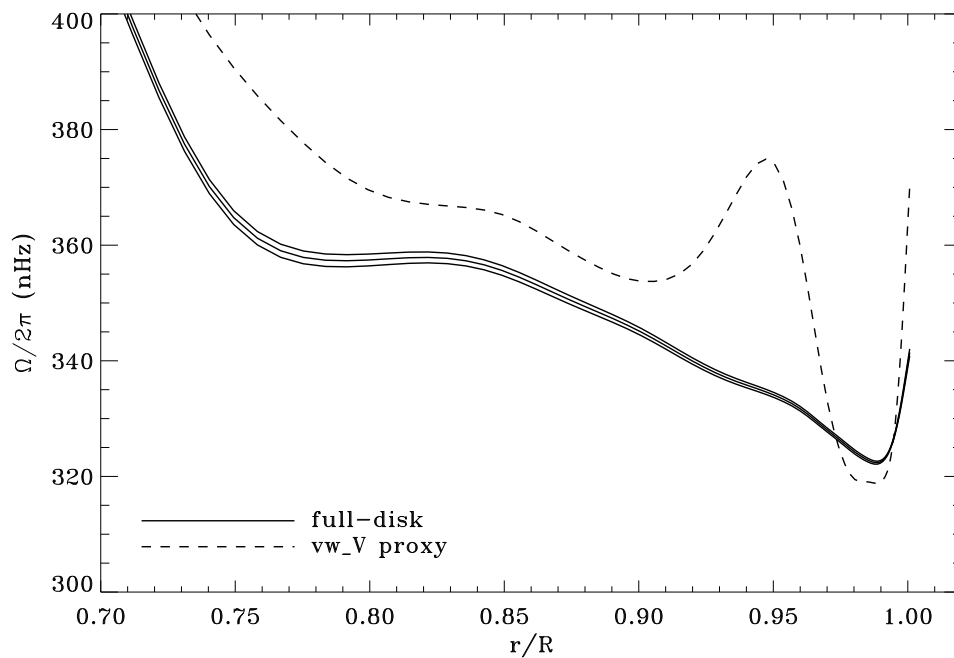


Figure 4.14: Internal rotation as a function of radius at 75° latitude for an average over six years of HMI. Solid lines show the full-disk analysis and its error; errors for the other analysis were similar.

4.4.5 Comparison of MDI and HMI

Both MDI and HMI were operating during the 2010 dynamics run. Hence, we have the opportunity to compare the mode parameters resulting from each dataset. Unfortunately, since the two instruments operate at two different cadences, it is not straightforward to generate a common window function. Setting this aside, Figure 4.15 shows a comparison of the modes common to the `fd_ap90` and regular HMI analyses for this time interval using their native window functions. Similarly, Figure 4.16 compares the analysis of the HMI `vw_V` proxy and the MDI `vw_V` datasets for the first 72 days of HMI. Again, since realization noise is identical for the two instruments, we hope to see small differences for the frequencies, widths, and a -coefficients, since these parameters should not depend on the height of formation.

These figures are encouraging in that the frequencies and a -coefficients do show little change between the two instruments, although there is a hint of a feature in the frequency differences around 1.7 mHz. One is not surprised to see large differences in amplitude and background parameter, since these parameters do depend on the height at which the mode is observed. Although the amplitude differences have different shapes in Figures 4.15 and 4.16, HMI always observed larger amplitudes for almost all modes. Unfortunately, HMI observed lower widths at low frequencies.

To see how much of the discrepancy results from differences in the instruments and how much results from differences in the processing, Figure 4.17 plots the difference between the HMI full-disk fits and the fits to the `vw_V` proxy data for the first 72 days of HMI, while Figure 4.18 plots the difference between the `fd_ap90` and `vw_ap83` for the 2010 dynamics run. In other words, Figure 4.18 can be thought of as the sum of Figures 4.2 and 4.3. The close similarity of Figures 4.17 and 4.18 gives us confidence that the observed differences have little to do with the source of the data.

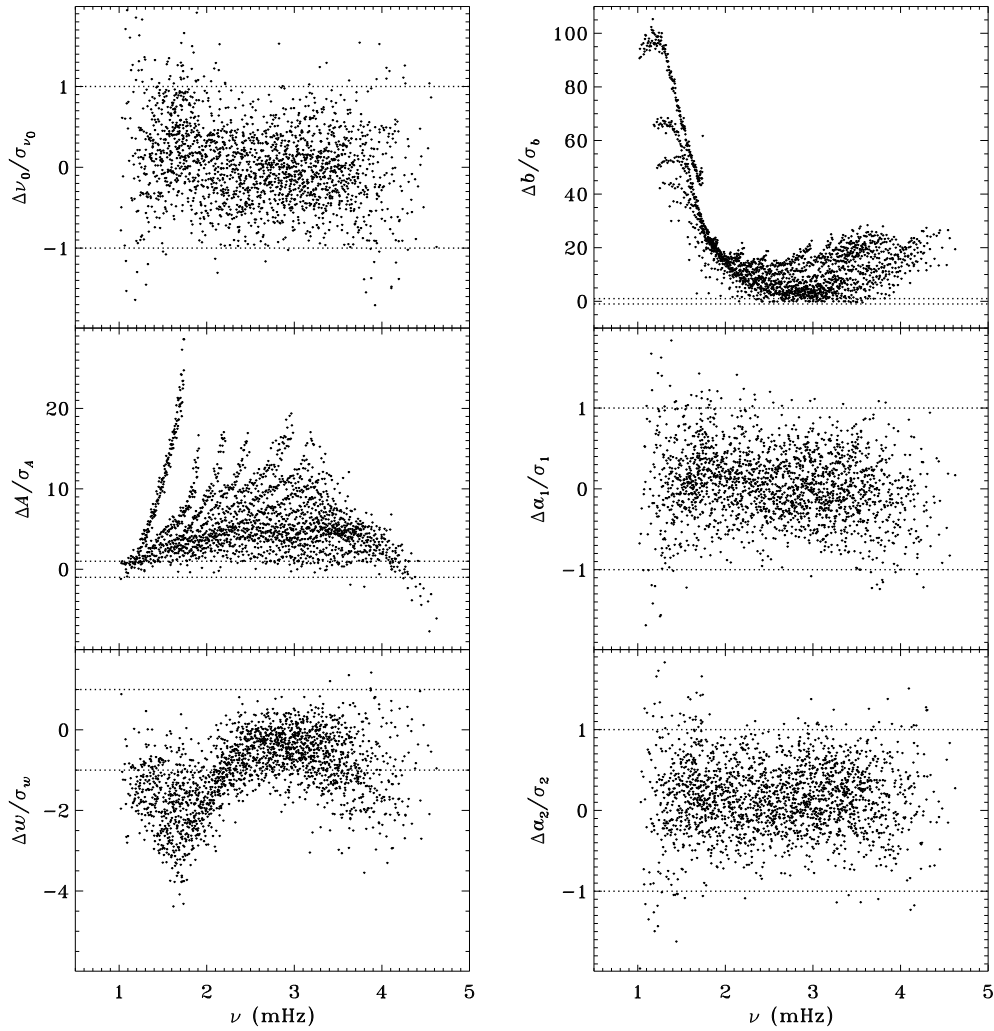


Figure 4.15: Difference between HMI and MDI full disk fits for the 2010 dynamics run. Each panel is scaled differently; dotted lines show the $\pm 1\sigma$ levels. The sense of subtraction is HMI minus MDI.

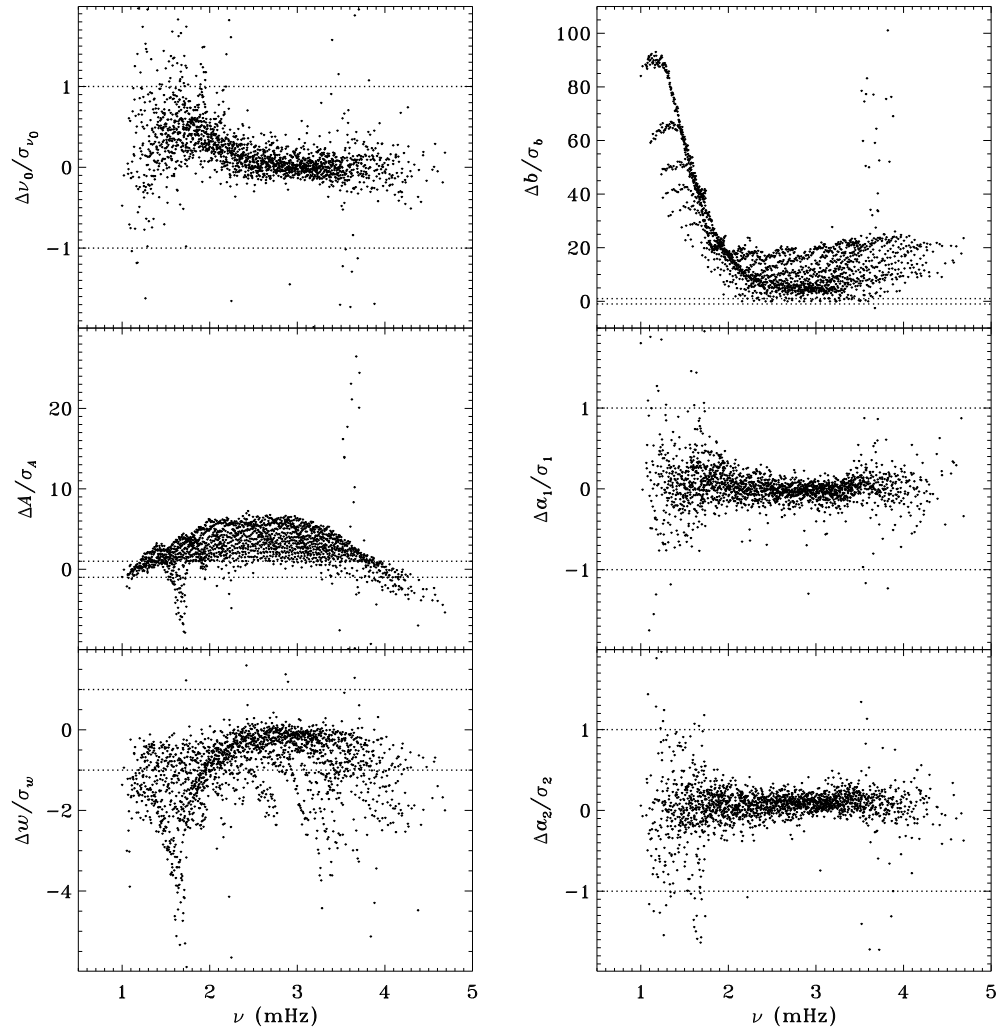


Figure 4.16: Difference between HMI v_w_V proxy and MDI v_w_V for the first 72 days of HMI. Panels are scaled as in Figure 4.15, with dotted lines showing the $\pm 1\sigma$ levels. The sense of subtraction is HMI minus MDI.

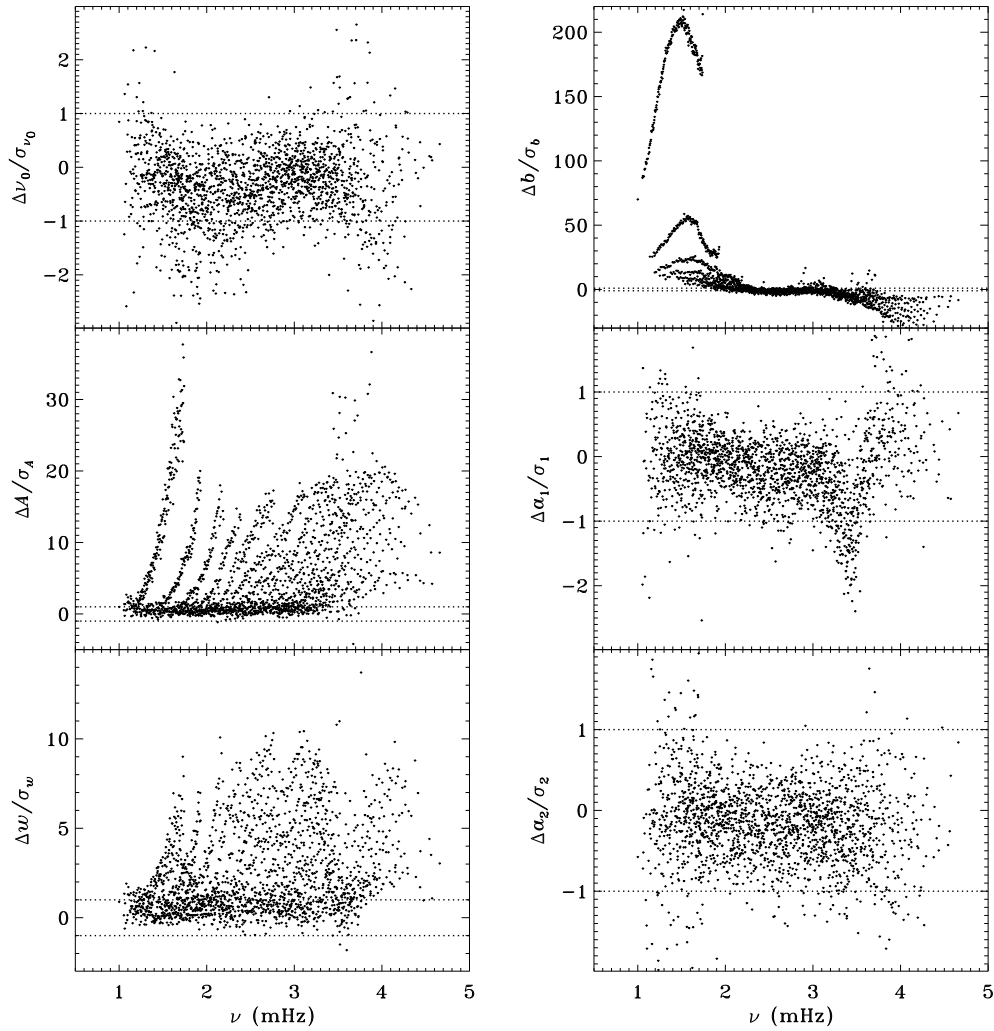


Figure 4.17: Difference between HMI full disk and vw_V proxy for the first 72 days of HMI. Each panel is scaled differently; dotted lines show the $\pm 1\sigma$ levels. The sense of subtraction is full-disk minus vw_V proxy.

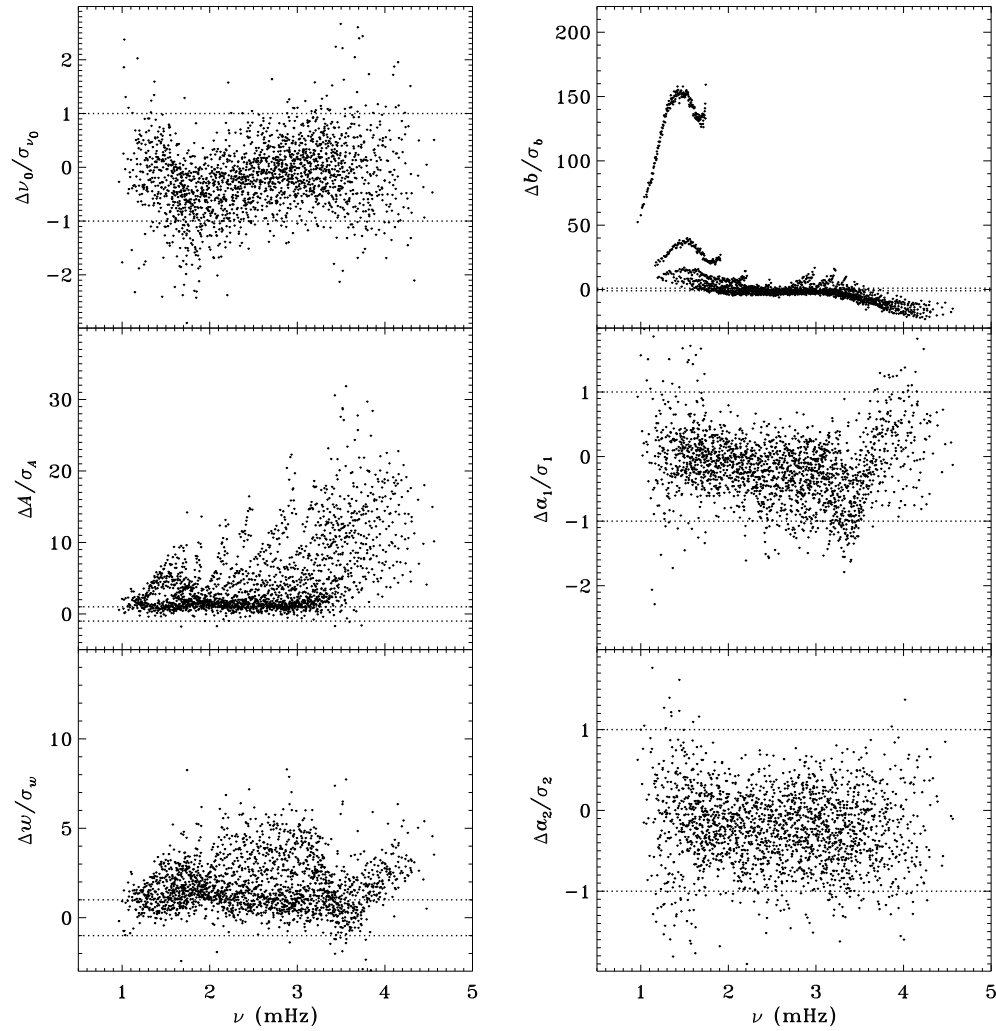


Figure 4.18: Difference between fd_ap90 and vw_ap83 for the 2010 dynamics run. Panels are scaled as in Figure 4.17, with dotted lines showing the $\pm 1\sigma$ levels. The sense of subtraction is fd_ap90 minus vw_ap83 .

4.4.6 Annual Periodicity

The analysis of the `vw_V` data revealed a one-year period in the fractional frequency change of the f -modes. In LS we found that the amplitude of the annual component increased with increasing degree, but it was decreased by correcting for the Doppler shift caused by the motion of SOHO relative to the Sun. In Figure 4.19 we show the fractional change in f -mode frequency for the entire mission using the updated mode parameters. The values shown have been averaged over a range in ℓ from 251 to 300 and the Doppler correction has been applied. To see how the frequency shifts vary with the solar cycle, we plotted them against the average rms value of the line-of-sight magnetic field, as given by the `DATARMS` keyword in the corresponding data series. We found a linear relationship between the two. After subtracting this solar-cycle dependence, we expect to see an oscillation related to the absolute value of B_0 . To demonstrate that this is so, we overplot the two quantities in Figure 4.20. The correlation coefficient between the frequency shifts and the average absolute value of B_0 is 0.47.

To see if the same is true for HMI, we apply the same procedure to the `vw_V` proxy, although in this case the motion of the spacecraft relative to the Sun has already been corrected for in the dopplergrams by shifting their target times. Again we see a prominent six-month signal, but it is weaker than for MDI, as Figure 4.22 shows. In this case the correlation coefficient was only 0.28. However, inspection of the number of modes fitted as a function of time for the `vw_V` proxy, shown in Figure 4.8, reveals exactly this period. Overplotting the absolute value of B_0 further reveals that, contrary to all expectation, mode coverage is lowest when B_0 is minimal, as Figure 4.23 shows. Here the correlation coefficient is 0.95. Recall that the leakage matrix is computed assuming $B_0 = 0$. Hence it can only come as a shock that we fit more modes when the leakage matrix is most incorrect. Until this discovery one might have thought that the variation of mode parameters with B_0 was related to the approximation that the leaks from $\Delta\ell + \Delta m$ odd are zero, since it assumes north-south symmetry. It now seems much more likely that the variation has to do with what part of the solar surface is visible.

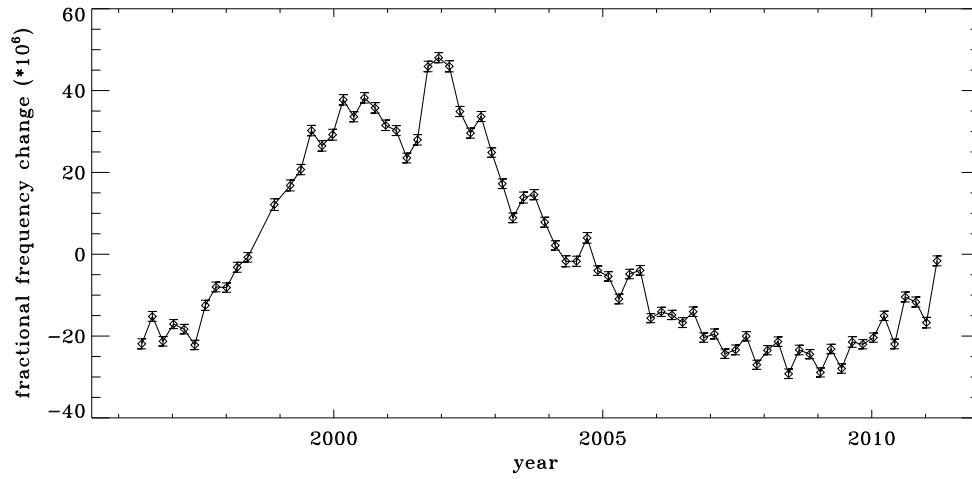


Figure 4.19: Fractional change in f -mode frequency for the entire MDI mission.

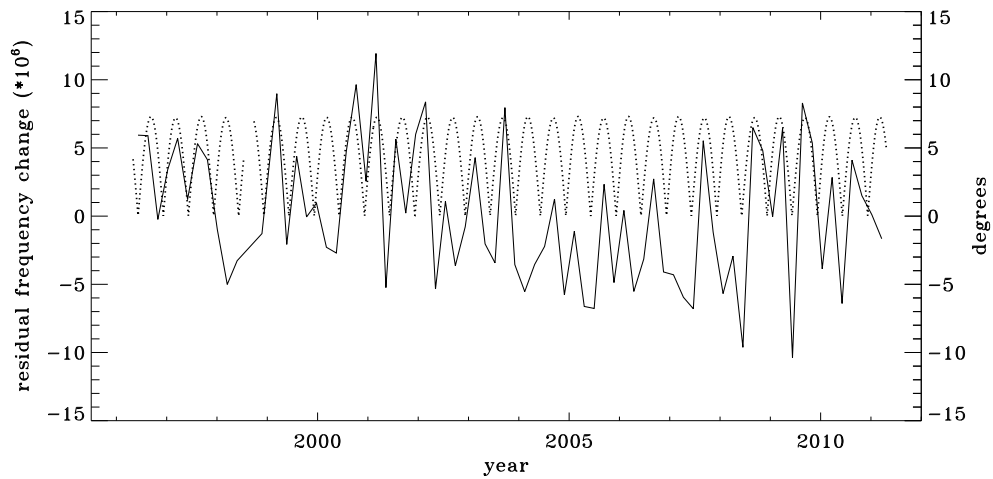


Figure 4.20: Fractional change in f -mode frequency for MDI with solar-cycle dependence removed. Overplotted is the absolute value of B_0 .

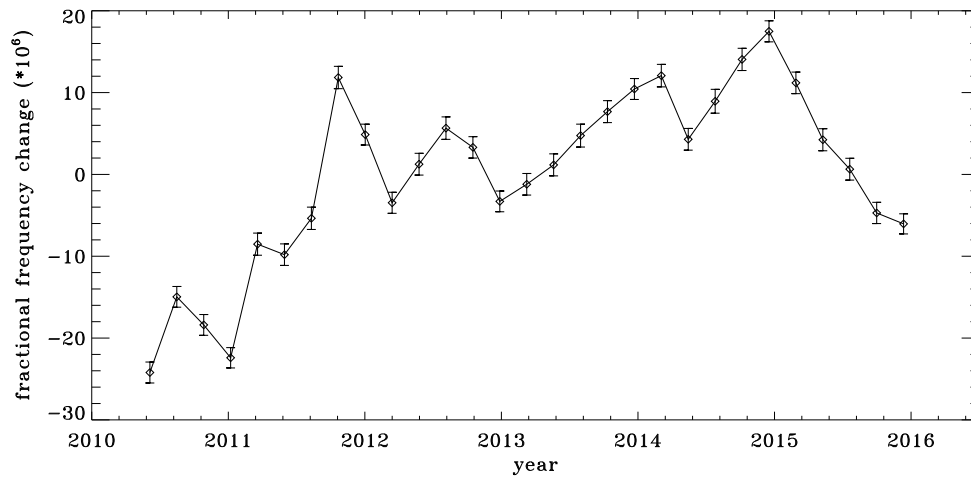


Figure 4.21: Fractional change in f -mode frequency for the first six years of HMI.

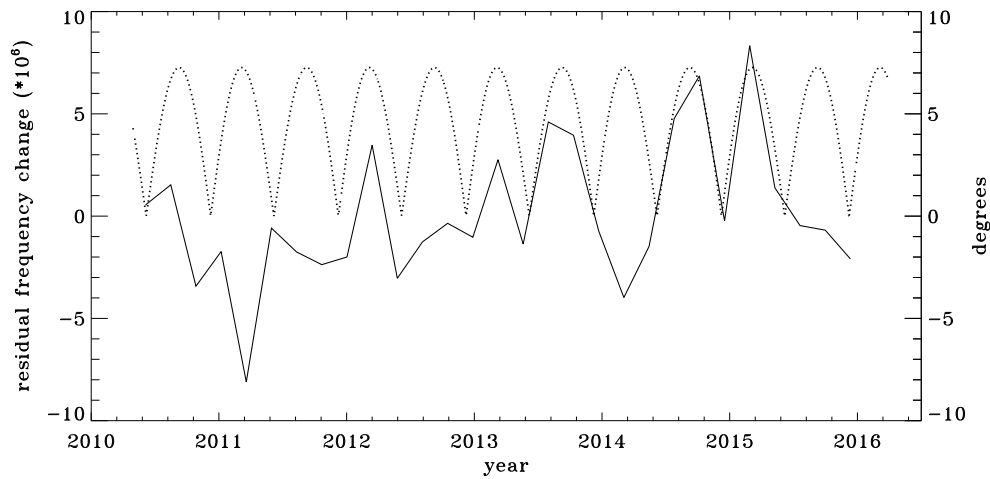


Figure 4.22: Fractional change in f -mode frequency for HMI with solar-cycle dependence removed. Overplotted is the absolute value of B_0 .

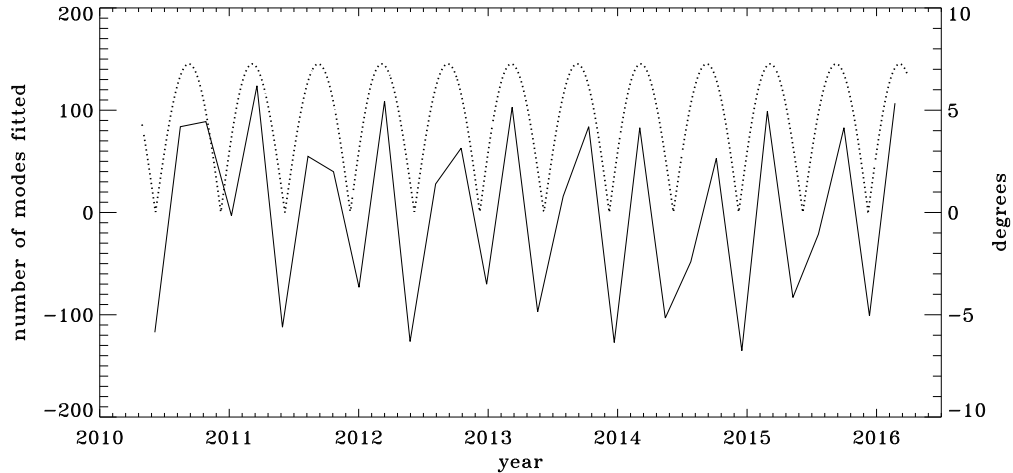


Figure 4.23: Number of modes fitted as a function of time for the HMI vw_V proxy relative to the mean (total number fitted shown in Figure 4.8). Overplotted is the absolute value of B_0 .

4.5 Discussion and Future Prospects

In comparing the MDI full-disk data with the vw_V data we found that the difference in mode parameters, with the exception of the background, mostly resulted from the different apodizations used in the two analyses. In particular, the difference in a_1 showed the bump at 3.4 mHz. Correspondingly, two-dimensional RLS inversions of data using the full-disk apodization did not show the bump in the residuals, whereas it appeared almost the same in the two analyses using the vw_V apodization. Likewise, the high-latitude jet was almost completely absent when using the full-disk apodization. In one-dimensional inversions, the tradeoff curve for the full-disk analysis using the vw_V apodization still showed the anomalous shape seen in LS.

To explore the possible cause of these discrepancies, we plotted the ratio of the amplitudes from the full-disk analysis using its regular apodization to the amplitudes found using the vw_V apodization, and likewise for the widths. The result is shown in Figure 4.24. The shape of these ratios is roughly the same as the differences shown in Figure 4.2, where we plotted only the significance. The difference in amplitudes

would suggest a problem with the leakage matrix, which could also affect the widths, but those differences might also be attributed to the model we use for the background. Although not shown, we found that the background differences themselves also showed a trend similar to that seen in the significance.

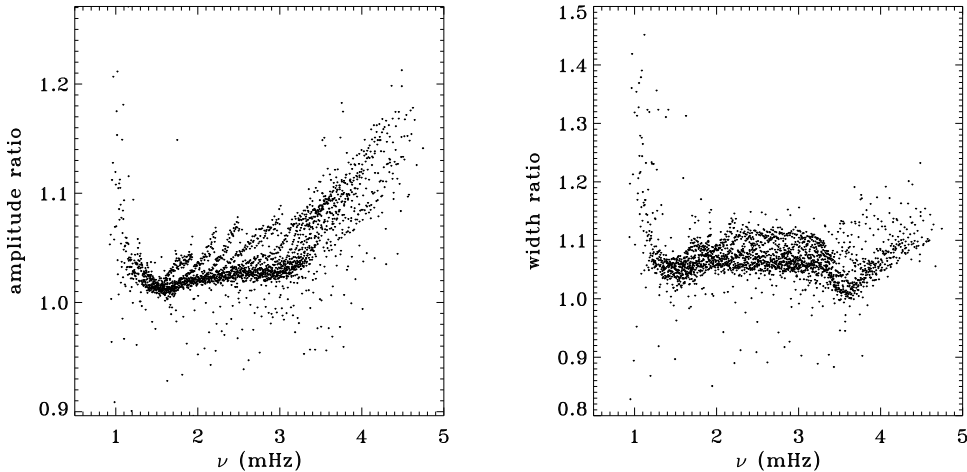


Figure 4.24: Ratios of amplitude and width from the `fd_ap90` analysis to those from the `fd_ap83` analysis for an average over all dynamics runs. For the width, 17 points have been excluded from the range shown.

Smoothing and subsampling made highly significant changes only to the background parameter. Recalling that e^b multiplies the covariance of the noise at high frequencies (LS), one might guess that the gaussian convolution somehow changes the noise in that range. The smoothing and subsampling also made significant changes to the amplitude, and these changes varied in sign across the dynamics runs. One probable cause for the sign change is the difference between the best focus and commanded focus in the instrument, which varied throughout the mission. Tuning changes are also likely to play a part. The question of how the smoothing and subsampling change the amplitude at all remains unanswered, as their effect should be accounted for in the leakage matrix. In the future one might perform the smoothing without subsampling, since subsampled data should result in greater interpolation errors when the images are remapped, which could account for some of the differences. Other methods of smoothing and subsampling are possible, as well as measuring the covariance of the noise in different frequency intervals.

A variation in the analysis suggested by the results of the previous section is to use a leakage matrix for a non-zero B_0 . By good fortune, B_0 was near its minimum in the middle of the 1998 dynamics run, its average value being -6.35° . We repeated the peakbagging for this interval using full-disk leakage matrices computed for that value of B_0 for both apodizations. Although not shown, we found that the mode parameters changed similarly in both cases. The unsurprising exception was that the change in a_1 showed the bump, with marginal significance, when using the `vw_V` apodization. The amplitudes and background parameters showed highly significant changes, while the changes in width were moderately significant. The results of two-dimensional RLS inversions are shown in Figure 4.25. Clearly a large change resulted between $0.83R$ and $0.95R$ when using the `vw_V` apodization, whereas the change when using the full-disk apodization was not significant. Although not shown, we found similar results using the smoothed data. Plotting the tradeoff curves, shown in Figure 4.26, we see that the new leakage matrix resulted in lower residuals for both apodizations. We must point out, however, that the results using the new leakage matrices are not necessarily any more correct than the original results, since in both cases the leaks from $\Delta\ell + \Delta m$ odd are ignored. If we were to suppose that the results using the full-disk apodization are more correct, then using the leakage matrix calculated for $B_0 = -6.35^\circ$ actually made the results using the `vw_V` apodization worse.

The analysis of HMI data confirmed that using a proxy for the `vw_V` data resulted in both the high-latitude jet and the bump in the odd a -coefficients, whereas both were essentially absent from the analysis of full-disk data. Comparison of fits using asymmetric mode profiles to those using symmetric profiles revealed similar differences as seen in LS and in the analysis of MDI full-disk data. In spite of fitting fewer modes, asymmetric profiles (occasionally) resulted in more stable fits at the ends of ridges, mostly at the low- ℓ ends, but also at the high- ℓ ends for p -modes of low to moderate radial order. Comparison of 360-day fits to an average of 72-day fits also revealed differences similar to those seen in LS. Other investigators (Barekat, Schou, and Gizon, 2016, in press), however, have found differences in the inversions of modesets from the two instruments, which we have not discussed here, but should be investigated in the future.

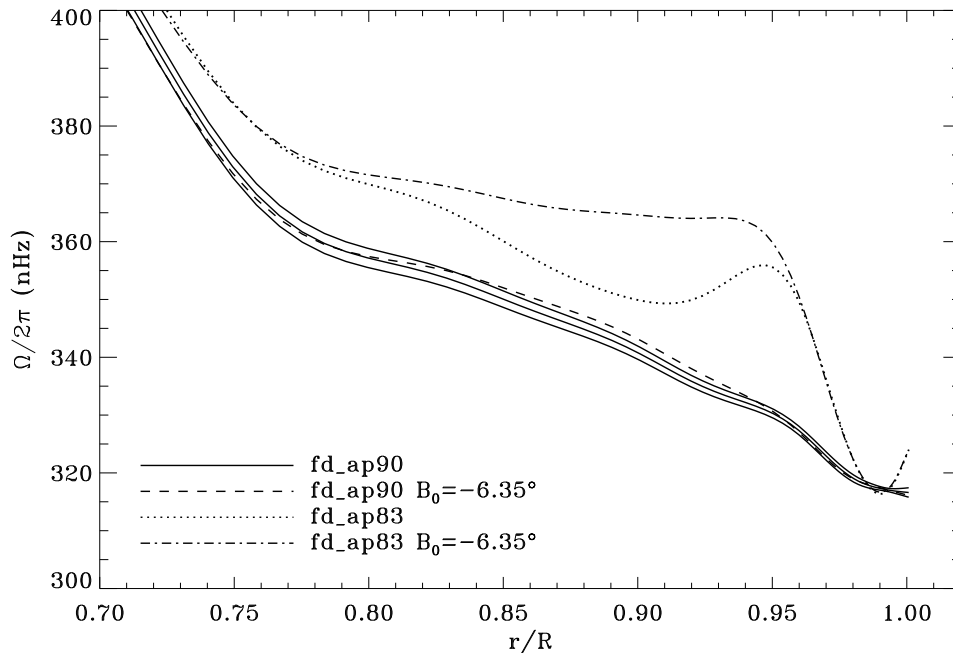


Figure 4.25: Effect of leakage matrix on inversions. Shown is internal rotation as a function of radius at 75° latitude for four analyses applied to the 1998 dynamics run. Two of the curves were shown in Figure 4.7. Solid lines show the `fd_ap90` analysis and its error; errors for the other analyses were similar. For these inversions the full modesets were used, rather than common modesets.

HMI also allows us to compare the difference between the full-disk results and those for the `vw_V` proxy in the magnitude of the six-month oscillation. Although we have not examined the frequency shifts for the full-disk data, we did find the surprising result that more modes were fitted for the `vw_V` proxy when the absolute value of B_0 was at its peak. This might suggest that the systematic errors we see are related to the alignment of the apodization circles with the spherical harmonic node lines. To see if this is true, one might try using differently shaped apodizations, such as apodizing in longitude rather than image radius, or an elliptical apodization.

In the comparison of mode parameters from HMI and MDI, we found that differences in frequencies and a -coefficients were not significant for the full-disk analyses, and even less so for the `vw_V` analyses. While the frequency differences indicated

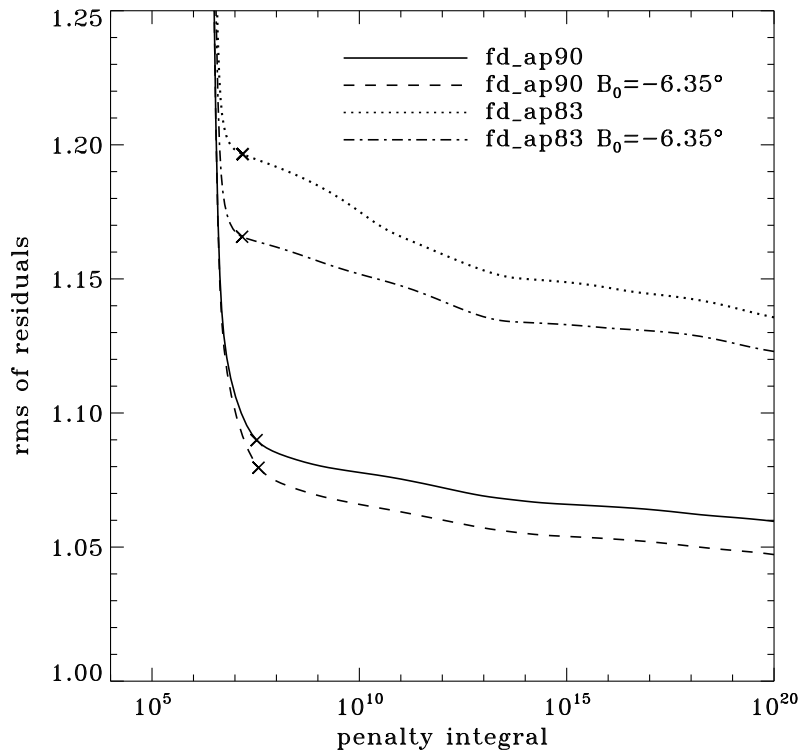


Figure 4.26. Effect of leakage matrix on residuals. Shown are tradeoff curves for four analyses applied to the 1998 dynamics run. Symbols indicate a tradeoff parameter of $\mu = 10^{-6}$. For these inversions the full modesets were used, rather than common modesets.

a small feature, the differences in a -coefficients were almost completely flat. Since these are the only parameters used in rotational inversions, there should be no problem with concatenating datasets from the two instruments in order to increase the interval over which consistent physical inferences can be drawn. Furthermore, if we believe that the full-disk analyses are more accurate than the \mathbf{vw}_V analyses, we can use the former to correct the latter. This is essential for MDI, since the \mathbf{vw}_V data are the only helioseismic dataset it provided with a high duty cycle.

Acknowledgements

This work was supported by NASA Contract NAS5-02139. *SOHO* is a mission of international cooperation between NASA and ESA. *SDO* is part of NASA's Living With a Star program. HMI data are provided courtesy of NASA/SDO and the HMI science team. The authors thank the Solar Oscillations Investigation team at Stanford University and its successor, the Joint Science Operations Center. Much of the work presented here was done while J. Schou was employed at Stanford University. T.P. Larson thanks the Max-Planck-Institut für Sonnensystemforschung for generously hosting him during the initial composition of this article.

Chapter 5

Looking Back, Looking Forward

5.1 Ideas

The preceding chapters have left us with several outstanding issues. The persistence of systematic errors (the bump and the jet) in the analyses using the smaller apodization, as well as unexplained differences in mode parameters between analyses, would lead one to suspect errors in the leakage matrix. Although this cannot yet be ruled out, other factors may be at play. To begin with, discrepancies in the fitted widths, both between HMI and MDI and between 360-day fits and 72-day fits, might indicate a problem with the the model we are using for the background (see Equation 3.13). Interestingly, the shape of the width differences was similar in the two cases: HMI saw significantly lower widths in a valley centered at about 1.7 mHz (see Figures 4.15 and 4.16), and the 360-day fits yielded a significant dip at about 1.4 mHz (see Figures 3.13 and 4.11). I also note that the 360-day fits saw a peak in the error estimates for the asymmetry parameter at the same frequency. Meanwhile, in the comparison between HMI and MDI, there was a small but discernible feature in the frequencies differences at about 1.7 mHz. For the 360-day fits, there was also a peak in the differences for the asymmetry parameter at about this frequency.

An error in the background model would also obviously explain differences in the background parameter itself, whether as a result of the apodization (see Figure 4.2), as a result of smoothing and subsampling (see Figure 4.3), or between 360-day and

72-day fits. It is more difficult to explain how the amplitudes are changed by either the apodization or the smoothing and subsampling. Both effects should be accounted for in the leakage matrix, so that is the most obvious place to search for errors. To begin with, the code used to create the artificial images as input was transcribed line by line from one language to another, and no programming errors were found. On the other hand, no error in this code can explain why the apodization affects the mode parameters, since the routines used for apodization are identical for the data and for the leakage matrix. Furthermore, the removal of various approximations in the calculation of the leakage matrix has yielded no results. For the smoothing, I replaced an analytical gaussian with the actual kernel used on the spacecraft. Instead of calculating leaks for a subset of modes (1824 out of 48516 for ℓ up to 310) and interpolating the rest, I have tried calculating all of them directly. Unfortunately, none of these considerations made any significant changes to the mode parameters. I have also made leakage matrices for different values of B_0 , which did affect the mode parameters, but since the code ignores the leaks arising from north-south asymmetry, it is not clear whether or not this represents an improvement.

In the last chapter we were surprised to find how several of our results depended on B_0 . When $|B_0|$ is maximal, we fit the most modes, with the number fitted for the `vw_V` proxy being higher than for the full-disk. On the other hand, when B_0 is close to zero, the full-disk analysis fit many more modes (see Figure 4.8). Ironically, when we have the the most modes is also when we see the jet (in the `vw_V` proxy analysis). Thus one might wonder if it is the extra modes that are causing the jet. To quell this concern in advance, I reanalyzed the the 72-day interval beginning on MDI day number 7336 (see Table 4.2). The average value of B_0 during this time was -6.79° . For the inversion, I only used the modes common with the 72-day interval beginning on MDI day number 6328. The average value of B_0 during that interval was -0.16° , and the average value of $|B_0|$ was 2.07° . These intervals were selected because of their high and low mode coverage, respectively. The results of two-dimensional RLS inversions are shown in Figure 5.1. As one can see, the bump is still present in the `vw_V` proxy analysis, although later we will see that it is somewhat reduced.

All is not well with the full-disk analysis, however. In particular, when B_0 is close

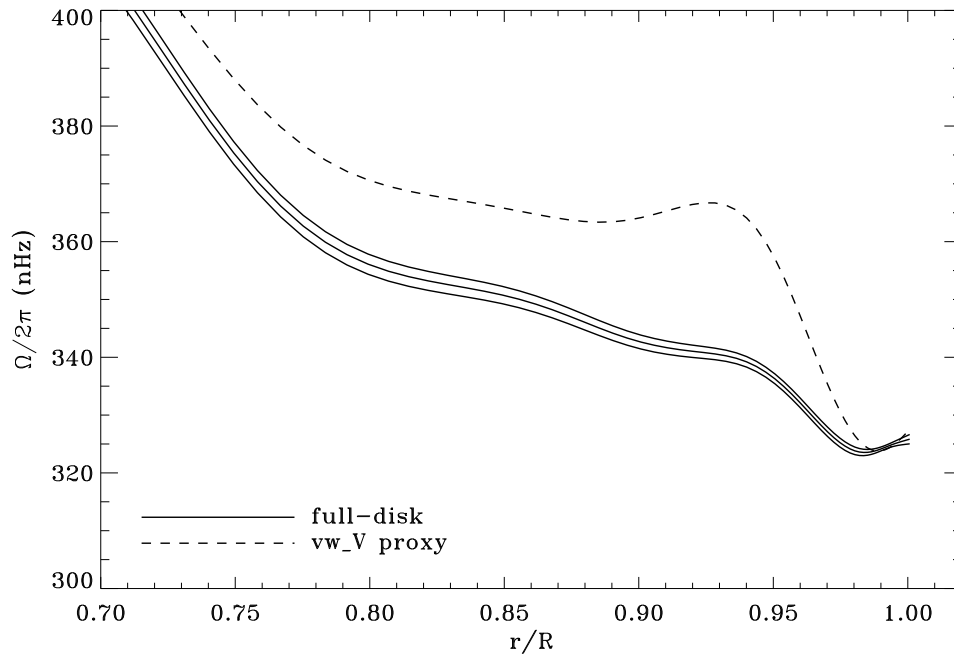


Figure 5.1: Internal rotation as a function of radius at 75° latitude for two analyses applied to the high- $|B_0|$ interval resulting from restricted modesets. Solid lines show the full-disk analysis and its error; errors for the other analysis were similar.

to zero, inversions show an upturn in the near-surface rotation rate at 75° latitude, which is clearly visible in the inversion of a six-year average (see Figure 4.14). This upturn is not visible in the full-disk analysis when $|B_0|$ is close to maximum, although the `vw_V` proxy analysis shows it more strongly at these times. This variation in the full-disk analysis can partly explain the results of Barekat, Schou, and Gizon (2016, in press), who saw significant differences in the gradient of the high-latitude, near-surface rotation rate between the inversions of 360-day and averaged 72-day fits for HMI but not for MDI. In the case of the MDI `vw_V` data, which are the only dataset from which 360-day MDI timeseries can be constructed, the upturn in the rotation rate at high latitudes is present at all times, albeit with different magnitudes. For the HMI full-disk analysis, however, it will be present in some 72-day intervals and not in others. For any 360-day analysis, the average value of $|B_0|$ will be close to its yearly average of 4.61° . Hence it is not surprising that the results differ, especially

considering that the difference in mode coverage implies a variation in the stability of the fits. I must emphasize that my results do not tell us whether the upturn or the lack thereof is a systematic error, but the variation with $|B_0|$ certainly is.

With the aim of obtaining the maximum information possible from each analysis, from here on I will consider only full modesets. To elucidate the issues discussed above, Figure 5.2 shows the inversions results for the HMI full-disk and *vw_V* proxy analyses for the two time intervals mentioned above. We see that the two types of analysis come into agreement near the surface for the low- $|B_0|$ interval, while for the other interval the rates and especially their derivatives differ markedly. The difference in the full-disk analyses between the two time intervals is significant in the range from $0.85R$ to $0.90R$, but this difference could possibly be solar in origin. Note that if we restrict the high- $|B_0|$ modeset as in Figure 5.1, the two analyses again agree near the surface.

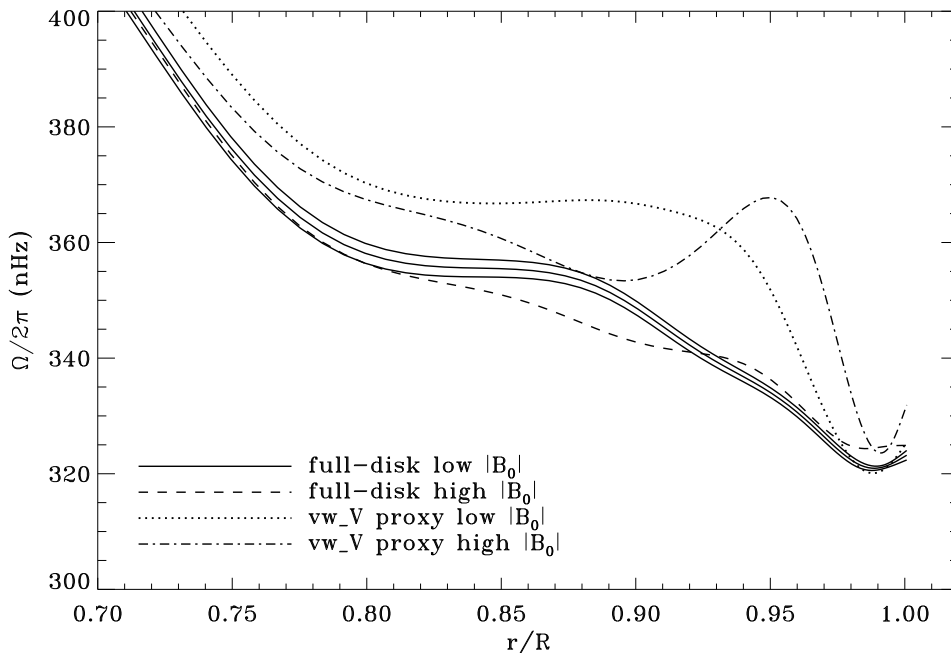


Figure 5.2: Internal rotation as a function of radius at 75° latitude for analyses applied to low- $|B_0|$ and high- $|B_0|$ intervals. Solid lines show the full-disk analysis for the former and its error; errors for the other analyses were similar.

The residuals from the inversions are reflected in the tradeoff curves in Figure 5.3. Although more modes were fitted for the high- $|B_0|$ interval, the residuals were lower for the low- $|B_0|$ interval. Although not shown, the bump remained unchanged, which is reflected in the unchanged shape of the tradeoff curve for the `vw_V` proxy analysis. Lastly, one hopes to achieve rms residuals close to unity, indicating that only random errors remain in the analysis. Unfortunately, this is not achieved in any of these analyses.

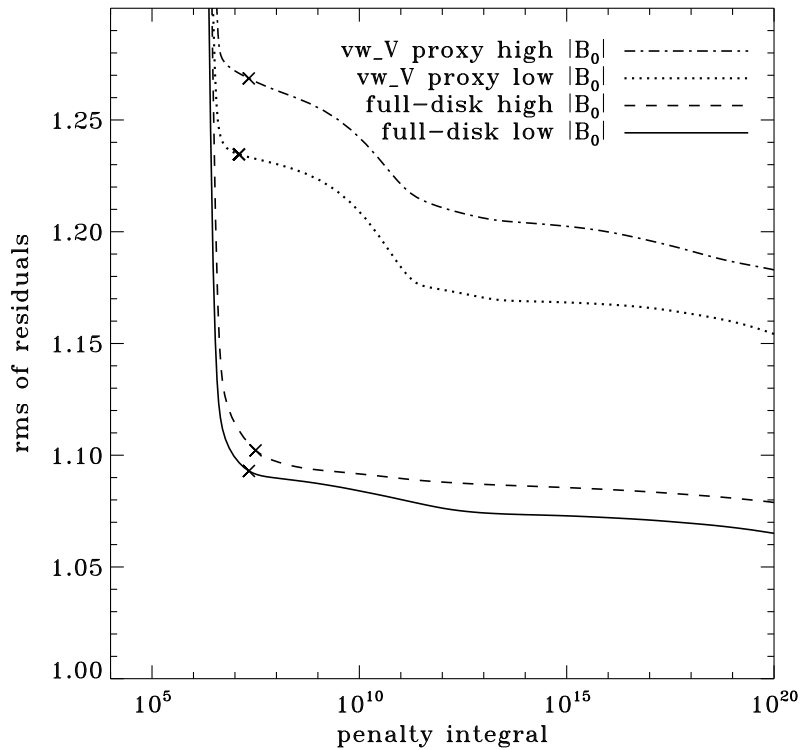


Figure 5.3. Tradeoff curves for analyses applied to low- $|B_0|$ and high- $|B_0|$ intervals. Symbols indicate a tradeoff parameter of $\mu = 10^{-6}$.

Since we know that the differences resulting from the apodization cannot be due to any error in the code that generates the input images for the leakage matrix, I am led to conjecture that some other effect causes them. The apodization may be affecting the data itself in unforeseen ways. The two apodizations so far discussed are different in the following way. Consider the case of $B_0 = 0$. For the wider apodization circle (defined by either the inner or outer apodization radius), the lines of constant longitude that are tangent to the circle are more “parallel” to it. That is,

the curvature is more similar at the tangent point for the larger than for the smaller apodization circle. As $|B_0|$ increases, one of the poles moves toward the circle and the lines of constant longitude tangent to the circle change their curvature. So what if we made the apodization perfectly parallel to lines of longitude? Fortunately, the spherical harmonic decomposition code is equipped to provide just such an apodization. Unfortunately, it is not able to apodize in latitude. Therefore I constructed an apodization shaped as follows: apodized with a cosine curve in longitude from $56.10^\circ = \arcsin(0.83)$ to $60.46^\circ = \arcsin(0.87)$ with a hard cutoff in latitude at 60° . This mimics the width of the `vw_V` apodization at the equator. More data may be included at the corners of this apodization, so small adjustments may have to be made to use it for MDI data, but I can certainly test it using the HMI `vw_V` proxy. We can expect the hard cutoff in latitude to spread some power around, but this should at least partially be accounted for in the leakage matrix. To account for it better, one could extend the range of the leaks used.

Figures 5.4 and 5.5 show the tradeoff curves and high-latitude rotation profiles for the low- $|B_0|$ interval using all three apodizations. Encouragingly, we see the new apodization resulted in reduced residuals relative to the `vw_V` apodization. The shape of its tradeoff curve is closer to the shape for the full-disk analysis, indicating that the bump is also reduced. Disappointingly, the new apodization did not make much difference to the rotation profile.

Figures 5.6 and 5.7 show the same plots for the high- $|B_0|$ interval. Here we see a marginal increase in the magnitude of the jet, but a much greater reduction of the residuals relative to the `vw_V` proxy¹. Furthermore, the residuals resulting from the new apodization are the only ones that did not increase for the higher value of $|B_0|$. The overall shape of the tradeoff curves remained unchanged.

As a final variation, I repeated the exercise at the end of chapter 4 for HMI data. That is, I calculated new leakage matrices for all three apodizations using $B_0 = -6.79^\circ$, and repeated the fitting of the high- $|B_0|$ interval. The results are shown in Figures 5.8 and 5.9. All three tradeoff curves are now close to the shape hoped for, and for each analysis the curves are the lowest yet. Although the `vw_V` proxy analysis still shows a slight sign of the bump, it had the greatest reduction in

¹This sentence has been changed; in the original dissertation, Figures 5.5, 5.7, and 5.9 mistakenly had the line styles interchanged for the two low-resolution analyses. Two words in the text have been changed as a result.

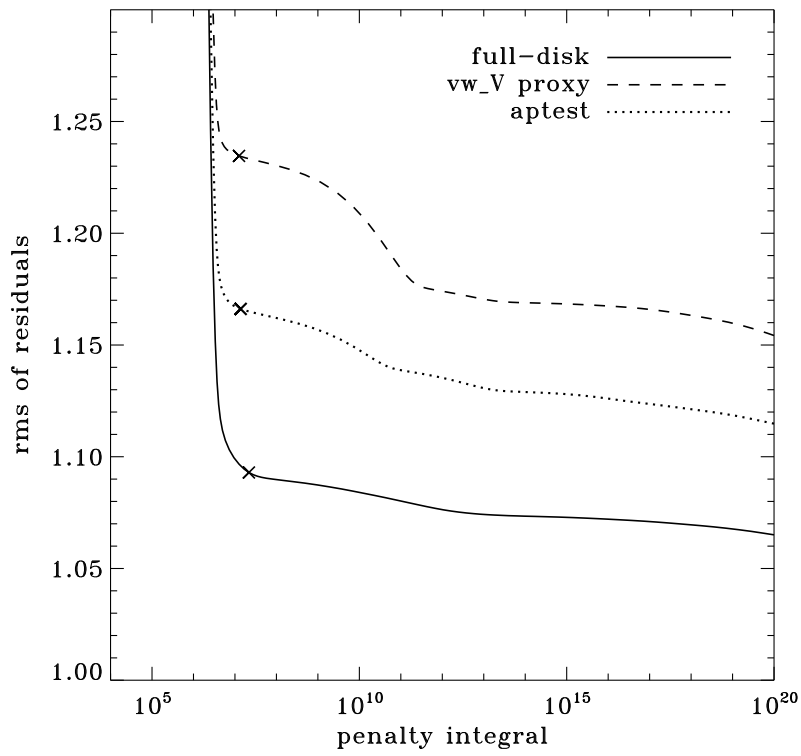


Figure 5.4. Tradeoff curves for three apodizations applied to the low- $|B_0|$ interval. The top and bottom curves were shown in Figure 5.3. Symbols indicate a tradeoff parameter of $\mu = 10^{-6}$.

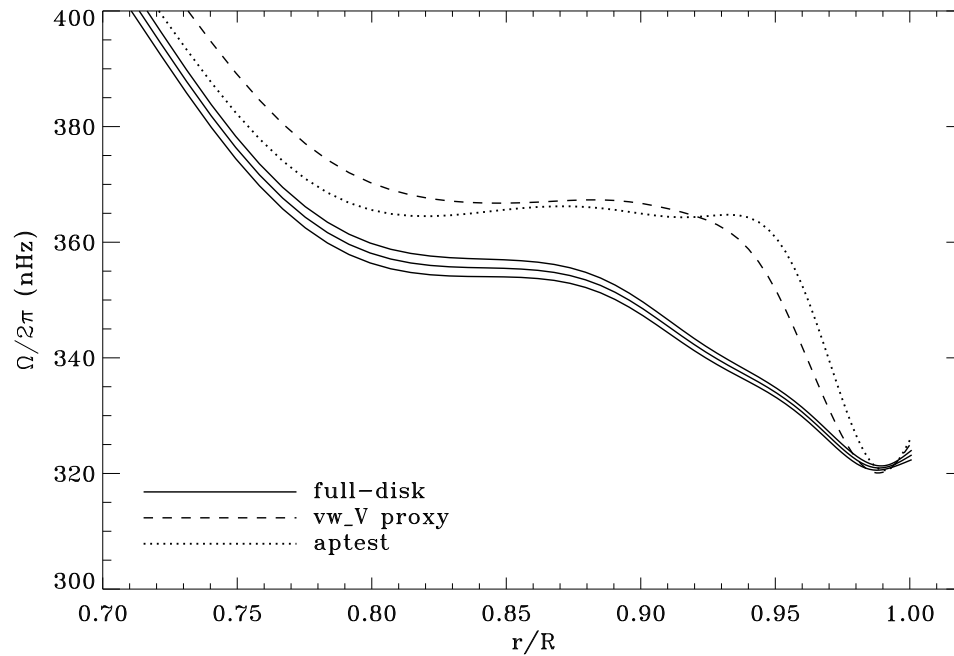


Figure 5.5: Internal rotation as a function of radius at 75° latitude for three apodizations applied to the low- $|B_0|$ interval. Two of the curves were shown in Figure 5.2. Solid lines show the full-disk analysis and its error; errors for the other analyses were similar.

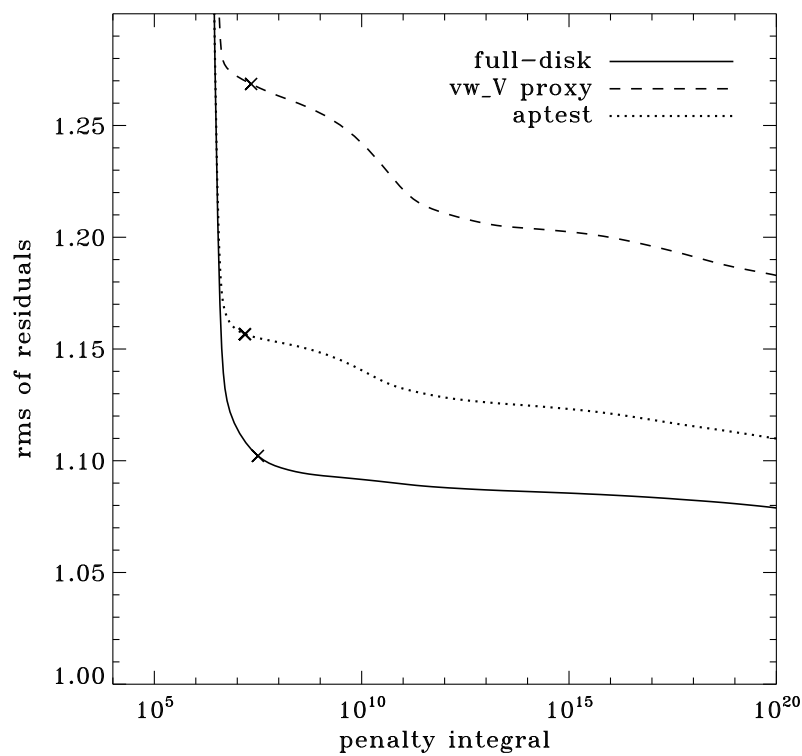


Figure 5.6. Tradeoff curves for three apodizations applied to the high- $|B_0|$ interval. The top and bottom curves were shown in Figure 5.3. Symbols indicate a tradeoff parameter of $\mu = 10^{-6}$.

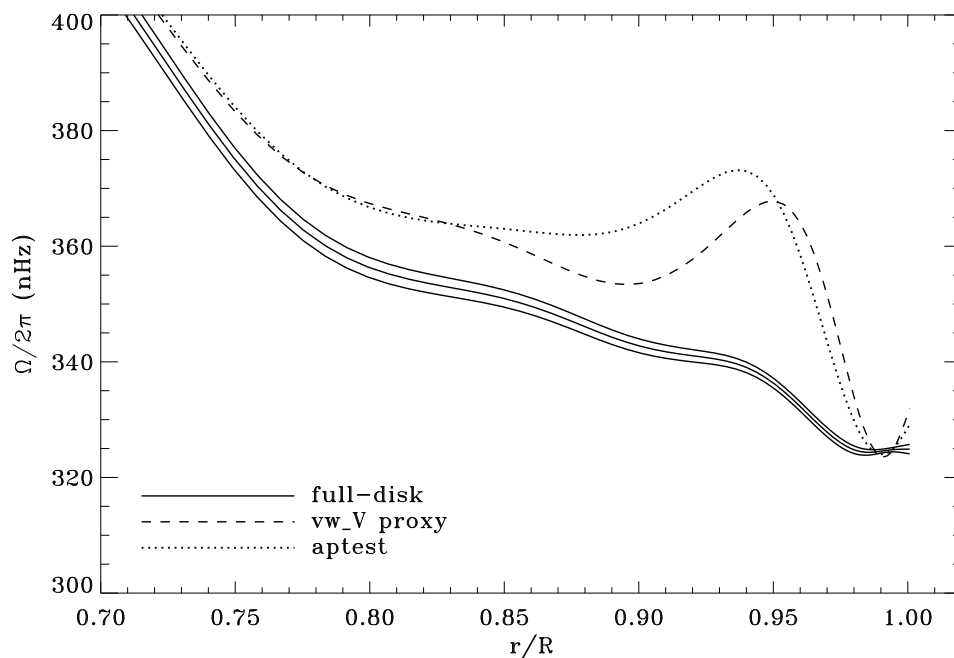


Figure 5.7: Internal rotation as a function of radius at 75° latitude for three apodizations applied to the high- $|B_0|$ interval. Two of the curves were shown in Figure 5.2. Solid lines show the full-disk analysis and its error; errors for the other analyses were similar.

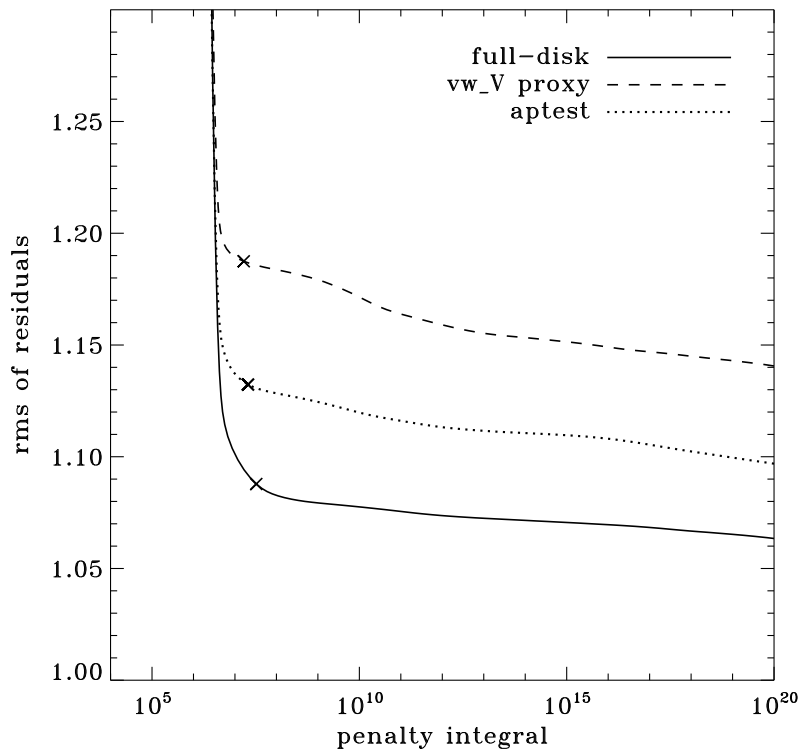


Figure 5.8. Tradeoff curves for three apodizations applied to the high- $|B_0|$ interval using a new leakage matrix. Symbols indicate a tradeoff parameter of $\mu = 10^{-6}$.

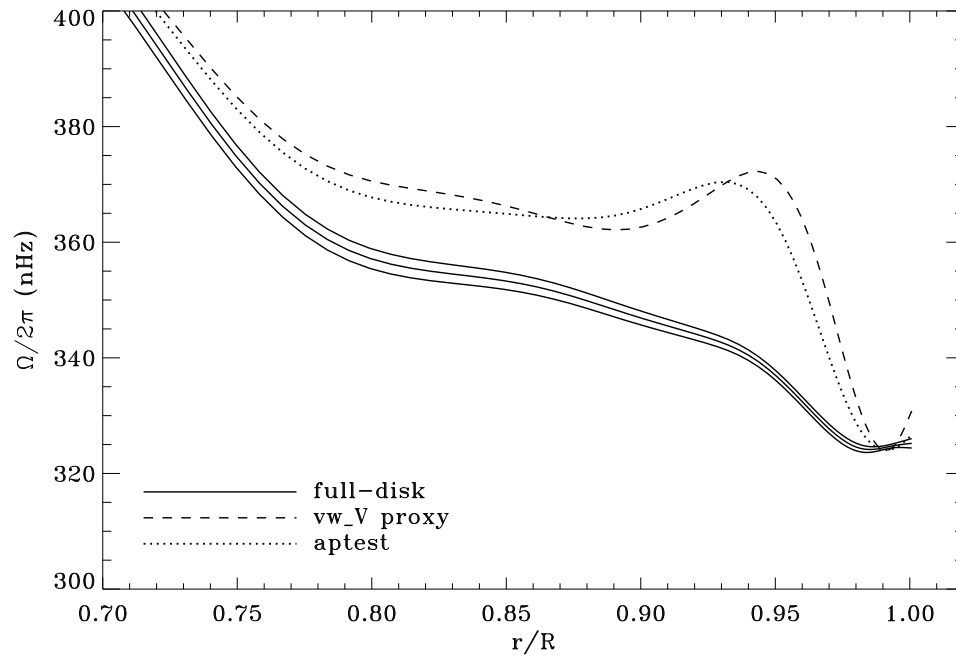


Figure 5.9: Internal rotation as a function of radius at 75° latitude for three apodizations applied to the high- $|B_0|$ interval using a new leakage matrix. Solid lines show the full-disk analysis and its error; errors for the other analyses were similar.

its residuals. None of the curves reach a value of 1.0, which indicates there are still systematic errors in all of them, or that perhaps the errors have been underestimated. Again the new apodization resulted in a rotation profile close to that using `vw_V` apodization, except near the surface, where the full-disk and `vw_V` proxy analyses are now in agreement.

Overall, the results using the new apodization are quite encouraging. One might hope that once an apodization in latitude is added, we will see even more improvement.

5.2 Zonal Flows

Now we move on to a review of our results in the context of the Sun's zonal flow pattern. I have described one method among many for measuring how the solar rotation rate varies with latitude throughout the convection zone. When a suitable time average or a static fit of this global rotation rate is subtracted, the residual velocities reveal bands of faster-than-average and slower-than-average rotation alternating in latitude (see Figure 1.3). The pattern has two branches that begin at mid-latitudes; one propagates toward the poles and the other propagates toward the equator. The latter is closely correlated with the emergence of magnetic activity (see Figure 1.1). Although there is no generally accepted explanation for it, the zonal flow pattern is believed to be an important clue to understanding the solar dynamo.

To see how the different analyses presented in this dissertation affect the zonal flow pattern, I have performed inversions using the f -modes only, which have the lowest errors and sample the outermost layers of the Sun, where the pattern is most visible. The temporal mean of a_1 , a_3 , and a_5 are subtracted from each before inversion, leaving the remaining odd a -coefficients unchanged. This is equivalent to subtracting a smooth curve in latitude. The resulting zonal flow plot for the updated analysis of the MDI `vw_V` data in 72-day timeseries using symmetric mode profiles is shown in Figure 5.10. The difference between the updated and original analysis is shown in Figure 5.11. Up until about the middle of 2003 the differences were small and mostly negative, meaning that the updated analysis saw a smaller prograde flow than the

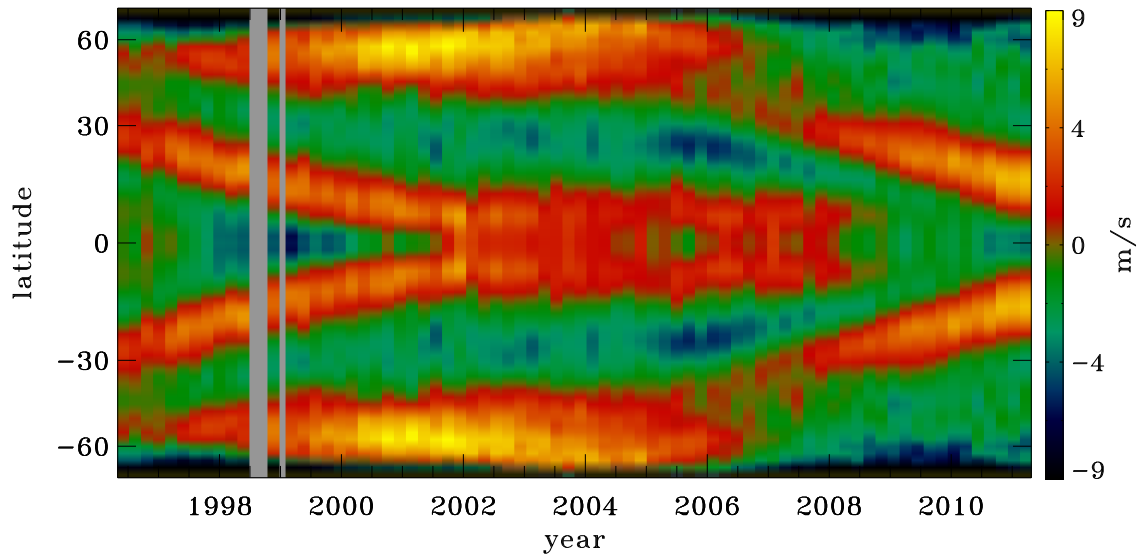


Figure 5.10: Zonal flows resulting from the MDI 72-day analysis with all updates applied, except asymmetric mode profiles

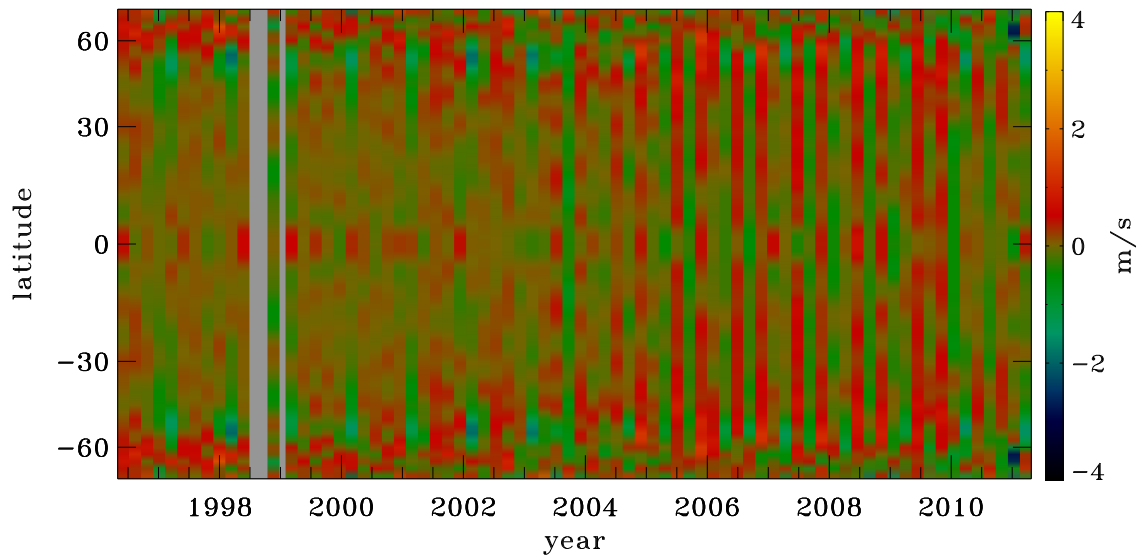


Figure 5.11: Difference in zonal flows between the original and updated MDI analysis. The sense of subtraction is updated minus original.

original analysis. The exception is near the poles, where the updated analysis saw a larger prograde flow. Afterward the differences seem to alternate from one 72-day interval to the next. Although the cause is not known, the transition is presumably due to antenna problems with SOHO that required the spacecraft to be inverted every three months, starting on 8 July 2003.

One can also see in the differences the annual period known to exist in the original analysis, both in mode coverage at the upper end of the ℓ range and in the f -mode frequencies themselves, the latter being caused largely by an uncorrected error in P_{eff} (see Section 3.4.2). I remind the reader at this point that these plots are all symmetric about the equator, since global-mode frequencies can only provide information about the symmetric component of the velocity field, as discussed at the end of Chapter 2.

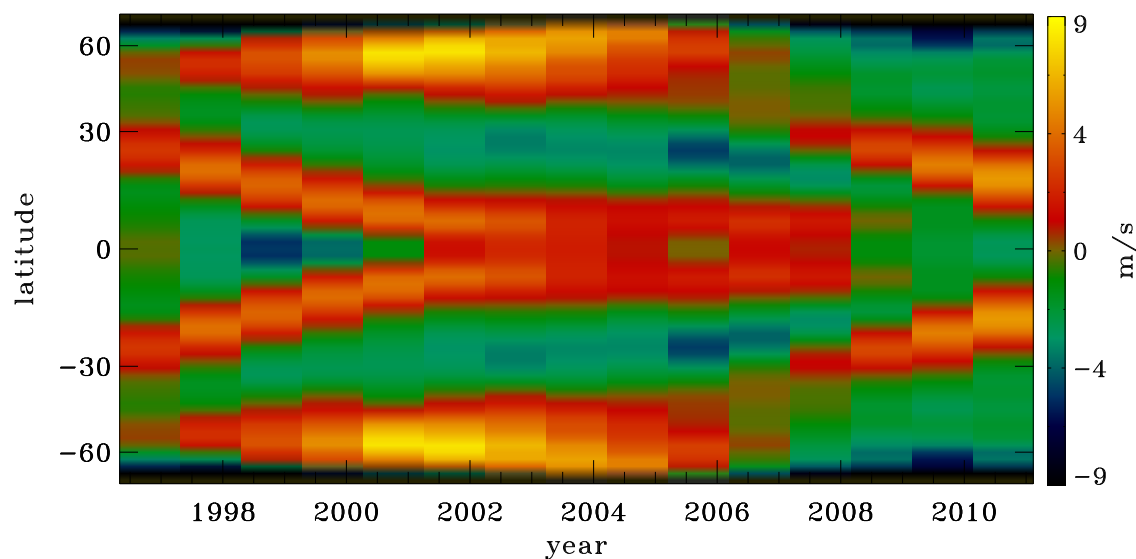


Figure 5.12: Zonal flows resulting from the MDI 360-day analysis using symmetric profiles.

Figure 5.12 shows the zonal flow pattern for the MDI vw_V data analyzed in 360-day timeseries using symmetric mode profiles. Although the longer timeseries result in less time resolution, the expanded mode coverage allows for a more precise measurement of the rotation. On the other hand, as lower values of ℓ are included, the inversion averages over a greater depth, so results from substantially different modesets cannot be directly compared.

The zonal flow plot for the HMI full-disk data analyzed in 72-day intervals using symmetric profiles is shown in Figure 5.13. The difference caused by using the `vw-V` proxy is shown in Figure 5.14. For the f -modes, the number fitted was similar for the two analyses. Still, based on the results above, one might expect to see a six-month period in the differences at high latitudes, but this is not discernible here. Overall, the small and essentially random differences give us confidence that the surface flows derived from the two analyses do not differ in any systematic way. A comparison with the fits using asymmetric profiles would be fitting at this point, but as discussed at the end of Section 3.3, they sometimes have problems with the f -modes. The number of f -modes fitted is usually comparable to the number fit with symmetric profiles, but occasionally the number is drastically smaller, compromising the inversion results. Hence I defer this comparison to the discussion of the 360-day fits, where this problem vanishes.

Figure 5.15 shows the zonal flows for the HMI full-disk data analyzed in 360-day timeseries. In this case, due to the large discrepancy in mode coverage, I repeated the inversion using only modes common with the averaged 72-day fits, and from this I subtracted the zonal flows resulting from those fits themselves. The result is shown in Figure 5.16. Although the differences are small, this plot does show bands that overlap the zonal flows themselves, especially the prograde flows. Since we already know that the radial gradient of the flow differs between the two modesets, it comes as no surprise that the flows themselves differ.

Figure 5.17 shows the difference resulting from the use of asymmetric mode profiles. Although these differences are the smallest seen, they show the clearest band structure. We expect the differences to be very small, since the asymmetric profiles predominantly change the even a -coefficients, and the rotation rate is only sensitive to the odd ones.

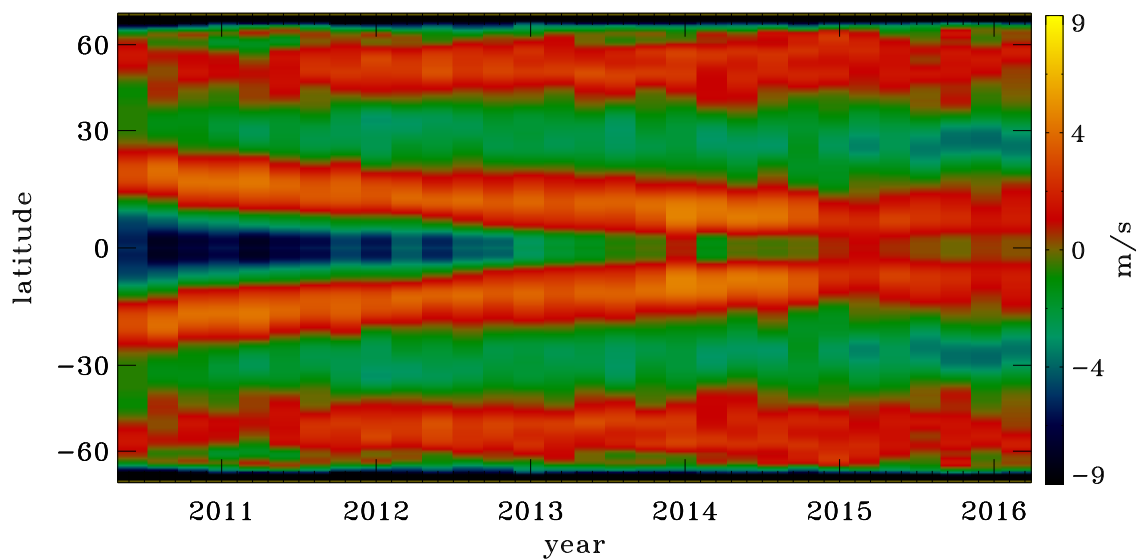


Figure 5.13: Zonal flows resulting from the HMI 72-day analysis using symmetric profiles.

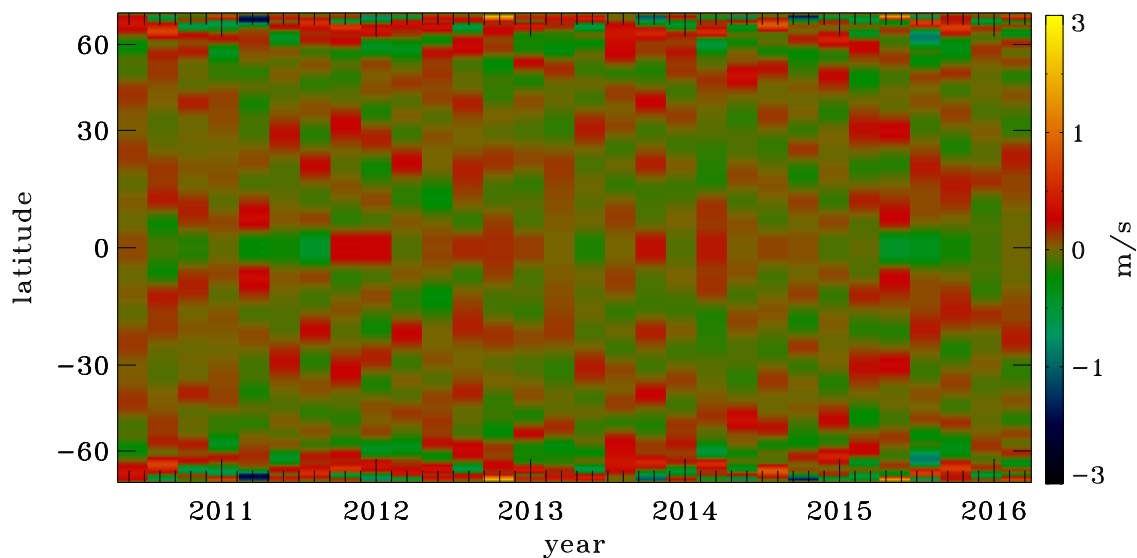


Figure 5.14: Difference in zonal flows resulting from the vw_V proxy. The sense of subtraction is full-disk minus vw_V proxy.

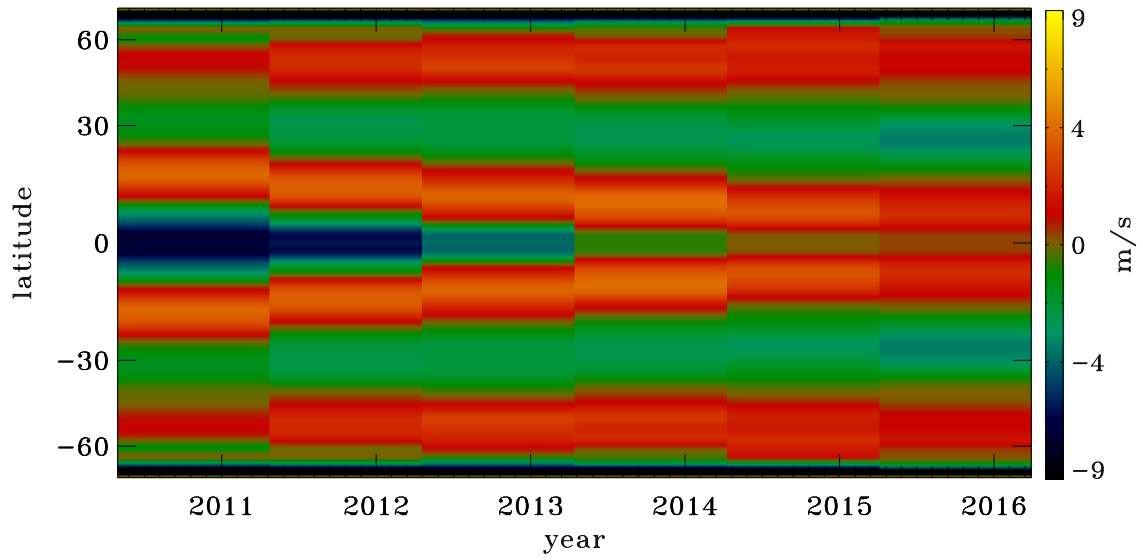


Figure 5.15: Zonal flows resulting from the HMI 360-day analysis using symmetric profiles.

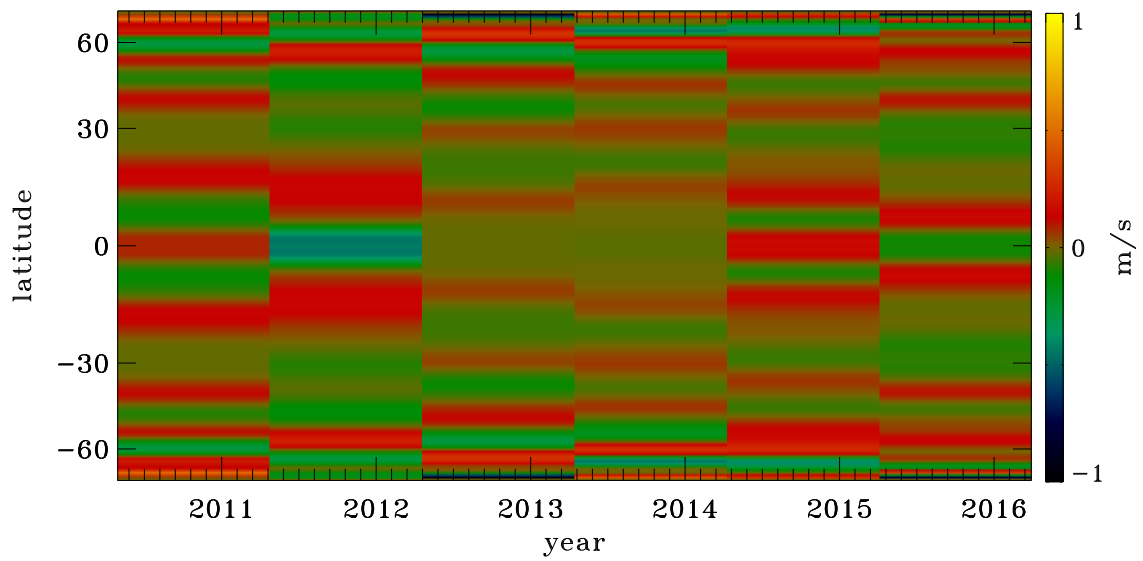


Figure 5.16: Difference in zonal flows between the 360-day and 72-day analyses using a common modeset. The sense of subtraction is 360 day minus 72 day.

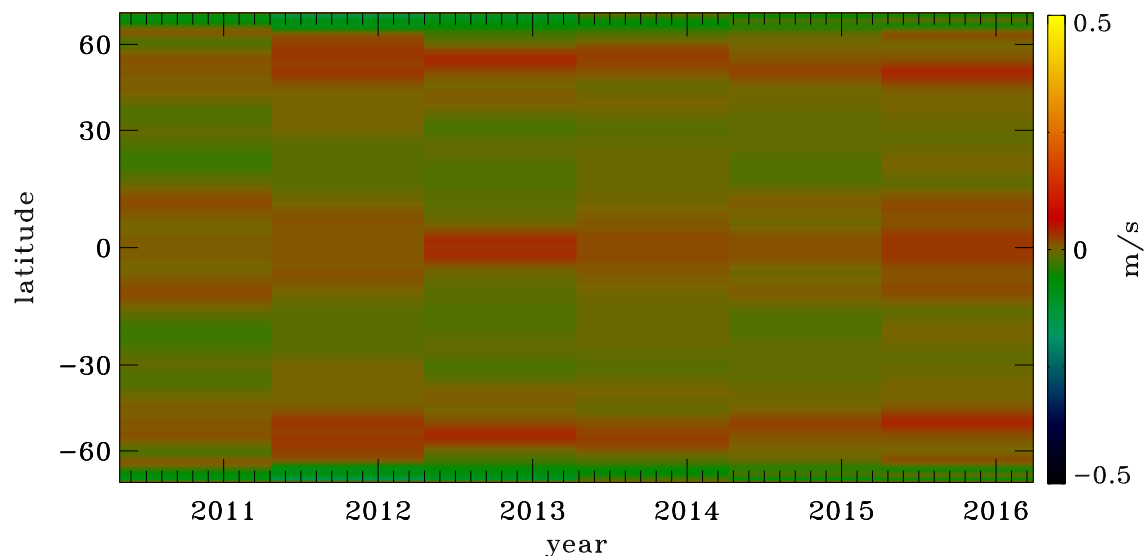


Figure 5.17: Difference in zonal flows between symmetric and asymmetric profiles for the HMI 360-day analysis. The sense of subtraction is asymmetric minus symmetric.

Finally, I show in Figure 5.18 a zonal flow plot resulting from the concatenation of the 72-day datasets from both MDI and HMI. For consistency, I have used the vw_V proxy for HMI. Although the poleward branches for the current cycle were clearly visible in Figure 5.13, here they can barely be seen relative to the branches in the previous cycle. The change in visibility is due to the different temporal average subtracted in the two cases. Previous research has shown this can be avoided by subtracting shorter averages, suggesting a change in the underlying rotation rate at high latitudes (Howe *et al.*, 2013).

5.3 Conclusion

In conclusion, throughout this dissertation I have given consideration to many factors that affect the inferences we are able to draw from solar data. Many that are left to consider are mentioned in the conclusions of Chapters 3 and 4. As a beginning, I was

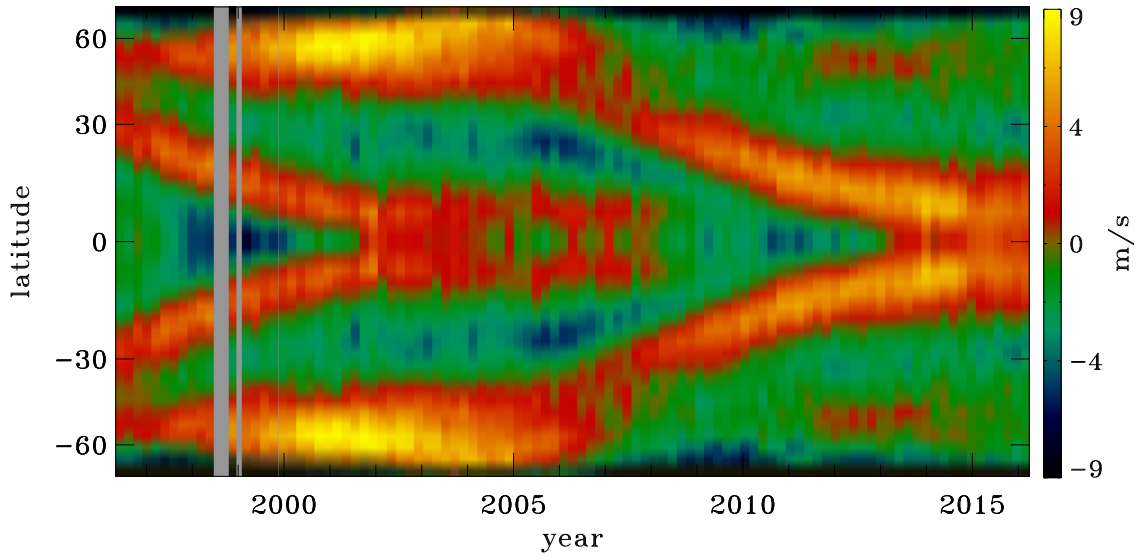


Figure 5.18: Zonal flows resulting from combined MDI and HMI 72-day vw_V datasets.

able to improve the analysis of data from the MDI Medium- ℓ program. In particular, residuals from inversions were reduced, as well as the magnitude of the annual component of the f -mode frequency shift. This latter was necessary to uncover the underlying six-month period that I later found in several unexpected areas. Although the systematic errors I sought out to address (the bump and the jet) were almost entirely unaffected, eventually I discovered that they both had to do with something we never would have guessed: the apodization of the input images. It was the comparison between the different MDI datasets that led me to continue my investigation using the HMI data, where the strong oscillation in the mode coverage for the vw_V proxy brought me to realize what should have been obvious all along. Thus I found that the jet (unlike the bump) was not a constant feature of the inversions. Although we may never understand how the portion of the disk used affects these errors, I have at least made progress toward a method for eliminating them. These results have also enabled other investigators, for example Barekat, Schou, and Gizon (2014) and Baldner *et al.* (2009), to improve various inferences of the solar interior.

For the future, I would like to go backward in time, namely to the helioseismic data collected at the Solar Tower at Mount Wilson Observatory. Since it precedes the beginning of the MDI data by nearly a full solar cycle, it will add to our knowledge of long-term trends in the Sun, such as the zonal flows discussed in this chapter. Considering how different the current and preceding cycles are, as shown by Figure 5.18, this backward extension could make a significant contribution towards efforts to predict the solar cycle. Moving forward, I would like to add the analysis of HMI intensity data to the standard processing performed here at Stanford. Although we can expect less mode coverage than for the velocity data, the intensity data has more signal at the solar limb, and so may possibly shed light on the issue of apodization. Further, the simultaneous fitting of intensity and velocity data could constrain mode parameters more tightly and result in an overall expansion of mode coverage, especially when using asymmetric mode profiles. Owing to different underlying mechanisms, the peaks in an intensity power spectrum have an asymmetry opposite to those in a velocity power spectrum. Hence we can expect to increase our understanding of mode physics by using both.

In the past I have performed preliminary analysis on both these types of data. Due to technical problems in both cases, it is with extreme regret that I am unable to present any results from these analyses here. Furthermore, as stated previously, the GONG data must be added to the list of datasets pending analysis. Since the original comparisons were made without regard to apodization, this dissertation gives us reason to be optimistic about resolving discrepancies between the two projects. Further, continued study using the HMI data may even allow us to go back and make better corrections to the MDI data. The concatenation of data from MDI and HMI will constitute one of the most extensive helioseismic datasets to date. With so much data in hand, new discoveries at the low end of the frequency spectrum may become possible.

Bibliography

- Anderson, E.R., Duvall, T.L. Jr., Jefferies, S.M.: 1990, Modeling of solar oscillation power spectra. *Astrophys. J.* **364**, 699–705. doi:10.1086/169452.
- Antia, H.M., Basu, S., Pintar, J., Schou, J.: 2001, How correlated are f-mode frequencies with solar activity? In: Wilson, A., Pallé, P.L. (eds.) *SOHO 10/GONG 2000 Workshop: Helio- and Asteroseismology at the Dawn of the Millennium*, *ESA Special Publication* **464**, 27–32.
- Appourchaux, T., Belkacem, K., Broomhall, A.-M., Chaplin, W.J., Gough, D.O., Houdek, G., Provost, J., Baudin, F., Boumier, P., Elsworth, Y., García, R.A., Andersen, B.N., Finsterle, W., Fröhlich, C., Gabriel, A., Grec, G., Jiménez, A., Kosovichev, A., Sekii, T., Toutain, T., Turck-Chièze, S.: 2010, The quest for the solar g modes. *Astron. Astrophys. Rev.* **18**, 197–277. doi:10.1007/s00159-009-0027-z.
- Babcock, H.D.: 1959, The Sun’s Polar Magnetic Field. *Astrophys. J.* **130**, 364. doi:10.1086/146726.
- Baldner, C.S., Antia, H.M., Basu, S., Larson, T.P.: 2009, Solar Magnetic Field Signatures in Helioseismic Splitting Coefficients. *Astrophys. J.* **705**, 1704–1713. doi:10.1088/0004-637X/705/2/1704.
- Barekat, A., Schou, J., Gizon, L.: 2014, The radial gradient of the near-surface shear layer of the Sun. *Astron. Astrophys.* **570**, L12. doi:10.1051/0004-6361/201424839.
- Barekat, A., Schou, J., Gizon, L.: 2016, in press, Solar-cycle variation of the rotational shear near the solar surface. *Astron. Astrophys.*

- Beck, J.G., Giles, P.: 2005, Helioseismic Determination of the Solar Rotation Axis. *Astrophys. J. Lett.* **621**, 153–156. doi:10.1086/429224.
- Beckers, J.M., Brown, T.M.: 1978, Solar circulation measurements: consideration and plans. In: Godoli, G. (ed.) *Future solar optical observations needs and constraints* **106**, 189.
- Brown, T.M.: 1986, Measuring the sun's internal rotation using solar p-mode oscillations. In: Gough, D.O. (ed.) *NATO Advanced Science Institutes (ASI) Series C, NATO Advanced Science Institutes (ASI) Series C* **169**, 199–214.
- Cacciani, A., Rhodes, E.J. Jr.: 1984, The magneto-optical filter, working principles and recent progress. In: Ulrich, R.K., Harvey, J., Rhodes, E.J. Jr., Toomre, J. (eds.) *Solar Seismology from Space*.
- Carrington, R.C.: 1858, On the Distribution of the Solar Spots in Latitudes since the Beginning of the Year 1854, with a Map. *Mon. Not. Roy. Astron. Soc.* **19**, 1–3. doi:10.1093/mnras/19.1.1.
- Carrington, R.C.: 1863, *Observations of the Spots on the Sun: From November 9, 1853, to March 24, 1861, Made at Redhill, University of Chicago Digital Preservation Collection*, Williams and Norgate, London, UK. <https://books.google.com/books?id=UCRWAAAAYAAJ>.
- Christensen-Dalsgaard, J.: 2002, Helioseismology. *Reviews of Modern Physics* **74**, 1073–1129. doi:10.1103/RevModPhys.74.1073.
- Christensen-Dalsgaard, J.: 2004, An Overview of Helio- and Asteroseismology. In: Danesy, D. (ed.) *SOHO 14 Helio- and Asteroseismology: Towards a Golden Future, ESA Special Publication* **559**, 1.
- Claverie, A., Isaak, G.R., McLeod, C.P., van der Raay, H.B., Cortes, T.R.: 1979, Solar structure from global studies of the 5-minute oscillation. *Nature* **282**, 591–594. doi:10.1038/282591a0.

- Deubner, F.-L., Gough, D.: 1984, Helioseismology: Oscillations as a Diagnostic of the Solar Interior. *Ann. Rev. Astron. Astrophys.* **22**, 593–619. doi:10.1146/annurev.aa.22.090184.003113.
- Duvall, T.L. Jr.: 1982, A dispersion law for solar oscillations. *Nature* **300**, 242. doi:10.1038/300242a0.
- Duvall, T.L. Jr., Jefferies, S.M., Harvey, J.W., Osaki, Y., Pomerantz, M.A.: 1993, Asymmetries of solar oscillation line profiles. *Astrophys. J.* **410**, 829–836. doi:10.1086/172800.
- Eddy, J.A.: 1976, The Maunder Minimum. *Science* **192**, 1189–1202. doi:10.1126/science.192.4245.1189.
- Fahlman, G.G., Ulrych, T.J.: 1982, A New Method for Estimating the Power Spectrum of Gapped Data. *Mon. Not. Roy. Astron. Soc.* **199**, 53.
- Fleck, B., Couvidat, S., Straus, T.: 2011, On the Formation Height of the SDO/HMI Fe 6173 Å Doppler Signal. *Solar Phys.* **271**, 27–40. doi:10.1007/s11207-011-9783-9.
- Gough, D.: 2013, What Have We Learned from Helioseismology, What Have We Really Learned, and What Do We Aspire to Learn? *Solar Phys.* **287**, 9–41. doi:10.1007/s11207-012-0099-1.
- Hale, G.E.: 1908, On the Probable Existence of a Magnetic Field in Sun-Spots. *Astrophys. J.* **28**, 315. doi:10.1086/141602.
- Hale, G.E., Ellerman, F., Nicholson, S.B., Joy, A.H.: 1919, The Magnetic Polarity of Sun-Spots. *Astrophys. J.* **49**, 153. doi:10.1086/142452.
- Hart, A.B.: 1954, Motions in the Sun at the photospheric level. IV. The equatorial rotation and possible velocity fields in the photosphere. *Mon. Not. Roy. Astron. Soc.* **114**, 17. doi:10.1093/mnras/114.1.17.
- Harvey, J.W.: 2013, Three Decades of Helioseismology at Kitt Peak and South Pole. In: Jain, K., Tripathy, S.C., Hill, F., Leibacher, J.W., Pevtsov, A.A. (eds.) *Fifty*

Years of Seismology of the Sun and Stars, Astronomical Society of the Pacific Conference Series **478**, 51.

Harvey, J.W., Hill, F., Hubbard, R.P., Kennedy, J.R., Leibacher, J.W., Pintar, J.A., Gilman, P.A., Noyes, R.W., Title, A.M., Toomre, J., Ulrich, R.K., Bhatnagar, A., Kennewell, J.A., Marquette, W., Patron, J., Saa, O., Yasukawa, E.: 1996, The Global Oscillation Network Group (GONG) Project. *Science* **272**, 1284–1286. doi:10.1126/science.272.5266.1284.

Hathaway, D.H.: 2010, The solar cycle. *Living Reviews in Solar Physics* **7**(1). doi:10.1007/lrsp-2010-1. <http://www.livingreviews.org/lrsp-2010-1>.

Hill, F., Bolding, J., Toner, C., Corbard, T., Wampler, S., Goodrich, B., Goodrich, J., Eliason, P., Hanna, K.D.: 2003, The GONG++ data processing pipeline. In: Sawaya-Lacoste, H. (ed.) *GONG+ 2002. Local and Global Helioseismology: the Present and Future, ESA Special Publication* **517**, 295–298.

Howard, R., Labonte, B.J.: 1980, The sun is observed to be a torsional oscillator with a period of 11 years. *Astrophys. J. Lett.* **239**, 33–36. doi:10.1086/183286.

Howe, R., Christensen-Dalsgaard, J., Hill, F., Komm, R.W., Larsen, R.M., Schou, J., Thompson, M.J., Toomre, J.: 2000, Deeply Penetrating Banded Zonal Flows in the Solar Convection Zone. *Astrophys. J. Lett.* **533**, 163–166. doi:10.1086/312623.

Howe, R., Christensen-Dalsgaard, J., Hill, F., Komm, R., Larson, T.P., Rempel, M., Schou, J., Thompson, M.J.: 2013, The High-latitude Branch of the Solar Torsional Oscillation in the Rising Phase of Cycle 24. *Astrophys. J. Lett.* **767**, L20. doi:10.1088/2041-8205/767/1/L20.

Korzennik, S.G.: 2005, A Mode-Fitting Methodology Optimized for Very Long Helioseismic Time Series. *Astrophys. J.* **626**, 585–615. doi:10.1086/429748.

Korzennik, S.G., Eff-Darwich, A.: 2013, Mode Frequencies from 17, 15 and 2 Years of GONG, MDI, and HMI Data. *Journal of Physics Conference Series* **440**(1), 012015. doi:10.1088/1742-6596/440/1/012015.

- Korzennik, S.G., Rabello-Soares, M.C., Schou, J.: 2004, On the Determination of Michelson Doppler Imager High-Degree Mode Frequencies. *Astrophys. J.* **602**, 481–516. doi:10.1086/381021.
- Larson, T., Schou, J.: 2009, Variations in Global Mode Analysis. In: Dikpati, M., Arentoft, T., González Hernández, I., Lindsey, C., Hill, F. (eds.) *Solar-Stellar Dynamos as Revealed by Helio- and Asteroseismology: GONG 2008/SOHO 21*, *Astronomical Society of the Pacific Conference Series* **416**, 311.
- Larson, T.P., Schou, J.: 2008, Improvements in global mode analysis. *Journal of Physics Conference Series* **118**(1), 012083. doi:10.1088/1742-6596/118/1/012083.
- Larson, T.P., Schou, J.: 2015, Improved Helioseismic Analysis of Medium- ℓ Data from the Michelson Doppler Imager. *Solar Phys.* **290**, 3221–3256. doi:10.1007/s11207-015-0792-y.
- Leighton, R.B., Noyes, R.W., Simon, G.W.: 1962, Velocity Fields in the Solar Atmosphere. I. Preliminary Report. *Astrophys. J.* **135**, 474. doi:10.1086/147285.
- Libbrecht, K.G.: 1992, On the ultimate accuracy of solar oscillation frequency measurements. *Astrophys. J.* **387**, 712–714. doi:10.1086/171119.
- Lloyd's and Atmospheric and Environmental Research: 2013, *Solar Storm Risk to the North American Electric Grid*, <http://www.lloyds.com/~media/lloyds/reports/emerging%20risk%20reports/solar%20storm%20risk%20to%20the%20north%20american%20electric%20grid.pdf>. [accessed 13-June-2016].
- Nigam, R., Kosovichev, A.G.: 1998, Measuring the Sun's Eigenfrequencies from Velocity and Intensity Helioseismic Spectra: Asymmetrical Line Profile-fitting Formula. *Astrophys. J. Lett.* **505**, 51–54. doi:10.1086/311594.
- Phillips, T.: 2014, *Near Miss: The Solar Superstorm of July 2012*, http://science.nasa.gov/science-news/science-at-nasa/2014/23jul_superstorm/. [accessed 13-June-2016].

- Rabello-Soares, M.C., Korzennik, S.G., Schou, J.: 2008, Analysis of MDI High-Degree Mode Frequencies and their Rotational Splittings. *Solar Phys.* **251**, 197–224. doi:10.1007/s11207-008-9231-7.
- Reiter, J., Rhodes, E.J. Jr., Kosovichev, A.G., Schou, J., Scherrer, P.H., Larson, T.P.: 2015, A Method for the Estimation of p-Mode Parameters from Averaged Solar Oscillation Power Spectra. *Astrophys. J.* **803**, 92. doi:10.1088/0004-637X/803/2/92.
- Rhodes, E.J. Jr.: 2013, The Observational Helioseismology Programs at the Sacramento Peak and Mount Wilson Observatories. In: Jain, K., Tripathy, S.C., Hill, F., Leibacher, J.W., Pevtsov, A.A. (eds.) *Fifty Years of Seismology of the Sun and Stars, Astronomical Society of the Pacific Conference Series* **478**, 61.
- Rhodes, E.J. Jr., Reiter, J., Schou, J., Kosovichev, A.G., Scherrer, P.H.: 2001, Observed and Predicted Ratios of the Horizontal and Vertical Components of the Solar p-Mode Velocity Eigenfunctions. *Astrophys. J.* **561**, 1127–1143. doi:10.1086/323260.
- Rhodes, E.J., Reiter, J., Schou, J., Larson, T., Scherrer, P., Brooks, J., McFaddin, P., Miller, B., Rodriguez, J., Yoo, J.: 2011, Temporal changes in the frequencies of the solar p-mode oscillations during solar cycle 23. In: Prasad Choudhary, D., Strassmeier, K.G. (eds.) *Physics of Sun and Star Spots, IAU Symposium* **273**, 389–393. doi:10.1017/S1743921311015614.
- Schad, A., Timmer, J., Roth, M.: 2013, Global Helioseismic Evidence for a Deeply Penetrating Solar Meridional Flow Consisting of Multiple Flow Cells. *Astrophys. J. Lett.* **778**, L38. doi:10.1088/2041-8205/778/2/L38.
- Scherrer, D.: 2015a, *Ancient Observatories - Timeless Knowledge*, <http://solar-center.stanford.edu/AO/Ancient-Observatories.pdf>. [accessed 11-June-2016].
- Scherrer, D.: 2015b, *Solar Folklore and Storytelling*, <http://solar-center.stanford.edu/folklore/Solar-Folklore.pdf>. [accessed 11-June-2016].

- Scherrer, P.H., Bogart, R.S., Bush, R.I., Hoeksema, J.T., Kosovichev, A.G., Schou, J., Rosenberg, W., Springer, L., Tarbell, T.D., Title, A., Wolfson, C.J., Zayer, I., MDI Engineering Team: 1995, The Solar Oscillations Investigation - Michelson Doppler Imager. *Solar Phys.* **162**, 129–188. doi:10.1007/BF00733429.
- Schou, J.: 1992, On the Analysis of Helioseismic Data. PhD thesis, , Aarhus University, Aarhus, Denmark, (1992).
- Schou, J.: 1999, Migration of Zonal Flows Detected Using Michelson Doppler Imager F-Mode Frequency Splittings. *Astrophys. J. Lett.* **523**, 181–184. doi:10.1086/312279.
- Schou, J., Bogart, R.S.: 2002, Reduction of Systematic Errors in MDI Measurements. In: *American Astronomical Society Meeting Abstracts #200, Bulletin of the American Astronomical Society* **34**, 645.
- Schou, J., Brown, T.M.: 1994, Generation of artificial helioseismic time-series. *Astron. Astrophys. Suppl.* **107**, 541–550.
- Schou, J., Christensen-Dalsgaard, J., Thompson, M.J.: 1994, On comparing helioseismic two-dimensional inversion methods. *Astrophys. J.* **433**, 389–416. doi:10.1086/174653.
- Schou, J., Howe, R., Basu, S., Christensen-Dalsgaard, J., Corbard, T., Hill, F., Komm, R., Larsen, R.M., Rabello-Soares, M.C., Thompson, M.J.: 2002, A Comparison of Solar p-Mode Parameters from the Michelson Doppler Imager and the Global Oscillation Network Group: Splitting Coefficients and Rotation Inversions. *Astrophys. J.* **567**, 1234–1249. doi:10.1086/338665.
- Schou, J., Scherrer, P.H., Bush, R.I., Wachter, R., Couvidat, S., Rabello-Soares, M.C., Bogart, R.S., Hoeksema, J.T., Liu, Y., Duvall, T.L., Akin, D.J., Allard, B.A., Miles, J.W., Rairden, R., Shine, R.A., Tarbell, T.D., Title, A.M., Wolfson, C.J., Elmore, D.F., Norton, A.A., Tomczyk, S.: 2012, Design and Ground Calibration of the Helioseismic and Magnetic Imager (HMI) Instrument on the Solar Dynamics Observatory (SDO). *Solar Phys.* **275**, 229–259. doi:10.1007/s11207-011-9842-2.

- Stein, R.F.: 2013, Models of the 5-Minute Oscillation and their Excitation. In: Jain, K., Tripathy, S.C., Hill, F., Leibacher, J.W., Pevtsov, A.A. (eds.) *Fifty Years of Seismology of the Sun and Stars, Astronomical Society of the Pacific Conference Series* **478**, 19.
- Van Helden, A.: 1995, *The Galileo Project — Science — Sunspots*, <http://galileo.rice.edu/sci/observations/sunspots.html>. [accessed 11-June-2016].
- Vorontsov, S.V.: 2007, Solar p modes of high degree l: coupling by differential rotation. *Mon. Not. Roy. Astron. Soc.* **378**, 1499–1506. doi:10.1111/j.1365-2966.2007.11894.x.
- Vorontsov, S.V., Jefferies, S.M.: 2013, Modeling Solar Oscillation Power Spectra. II. Parametric Model of Spectral Lines Observed in Doppler-velocity Measurements. *Astrophys. J.* **778**, 75. doi:10.1088/0004-637X/778/1/75.
- Woodard, M.F.: 1989, Distortion of high-degree solar p-mode eigenfunctions by latitudinal differential rotation. *Astrophys. J.* **347**, 1176–1182. doi:10.1086/168206.
- Woodard, M., Schou, J., Birch, A.C., Larson, T.P.: 2013, Global-Oscillation Eigenfunction Measurements of Solar Meridional Flow. *Solar Phys.* **287**, 129–147. doi:10.1007/s11207-012-0075-9.